
University of Rome TOR VERGATA

Faculty of Engineering
PhD Course in Engineering of Energy-Environment
XXII Cycle

PhD Thesis

# Numerical Analysis of Multiphase Flows through the Lattice Boltzmann Method

**Candidate**
Eng. *Daniele CHIAPPINI*

**Supervisor**
Prof. *Fabio GORI*

**Co-Supervisor**
Prof. *Gino BELLA*
Dr. Eng. *Sauro SUCCI*
Prof. *Stefano UBERTINI*

**Coordinator**
Prof. *Fabio GORI*

a.a. 2009/2010

*To my parents*

# Contents

# List of Figures

# List of Tables

# Introduction

This thesis deals with multiphase flows, i.e. systems in which different fluid phases, or fluid and solid phases, are simultaneously present. More specifically, in this work, the fluids are different phases of the same substance, such as a liquid and its vapor [4]. In the sense in which the term is normally understood, however, multiphase flow denotes a subset of this very large class of problems. A precise definition is difficult to formulate as, often, whether a certain situation should be considered as a multiphase flow problem depends more on the point of view of the investigator than on its intrinsic nature. As a common example one may consider a single small bubble as an instance of multiphase flow, particularly if the study focuses on features that would be relevant to an assembly of such entities.
There are a lot of factors which are source of complexity in the multiphase flow phenomena; not only the interaction between bubbles-droplets-particles immersed in a fluid, but also physical problems, like the transition between different liuid-gas flow regimes, or the presence of a perturbed interface, as well the simultaneous presence of phenomena occuring at different scales. This complexity represents a tough limit in the use of fully analitical methods designed in order to solve this kind of problems. For example, also the flow around

spheres -which have intrinsically simple shapes- present some analytical soltion which are definetely limited to either to small or large Reynolds numbers. For the most interesting applications, referred to moderate Reynolds numbers, a closed analytical solution is missing.
Moreover a lot of difficulties have to be faced up in an experimental setup. In fact, in a laboratory a lot of degrees of control are present. If we consider, for example, a droplet breakup in a gaseous turbulent domain, we have to determine exaclty all the parameters involved in this case-study, like the exact droplet diameter or the flow velocity.
Luckily, in these situations, the numerical simulation can help us and may become an essential tool for the analysis/investigation of multiphase flows. Moreover, very often, the numerical approach is the only available tool in order to investigate physical aspects of the phenomenon, for example the influence of gravity or the surface tension, free to be modified in the numerical simulation nevertheless they are fixed to a certain value in a laboratory setup. Furthermore, the complexity of multiphase flows requires to look to some reduced descriptions or averaged equations which can guarantee accurate results in an acceptable computational time. During last years many powerful computational capabilities have developed and they have represented a great improvement in multiphase flow analysis.
After having pointed out the great advantage of multiphase flow numerical analysis, introducing some interesting engineering applications is useful. The multiphase problems, in fact, some examples are sprays (e.g. in Internal Comustion Engine -ICE-), or pipelines, fluidized bed, distillation columns, etc. Morever there are many “Natural” phenomena which involve multiphase flows like cluods and rain, liquid droplets impingement, waves, rivers and water-falls. Again, as pointed out above, the scales involved in multiphase flows cover a complete range,

starting from *micro*-meters (sprays) until reaching *kilo*-meters. This wide range does not allow defining a universal model capable to solve all these applications.
Due to the simplicity of implementation and managing a lot of users have been encouraged in using the Lattice Boltzmann Method -LBM- in order to recast fluid-dynamic equations. The great diffusion has been reached concerning single phase approach. However, many techiniques have been defined for this innovative approach in order to model interactions between phases. The main advantage in using multiphase models coupled with the LBM is the possibility to solve the Equation of State -EOS- in every grid-point, with apparent advantages in terms of accuracy.
In the first chapter we will start with the derivation of continuity equation for a fluiddynamic system and we will show some numerical methods used to solve this kind of problems. In the second chapter the bases of Lattice Boltzmann Method will be presented, will be especially highlighted the reconstruction of Navier-Stokes equation from this kinematic apporach. In the third chapter, an overview of multiphase methods for LBM will be presented undelying advantages/disadvantages of each of them. Thus, in the fouth chapter the theory beyond the studied method will be presented giving some ideas about the implementation and about possile parallelization procedure. Finally in the last chapter some results for the above presented method will be shown in order to nderstand which are the real capabilities of it.

# Chapter 1

# Simulation of Multiphase Flows

## 1.1 Motivation

Multi-phase flows are not only part of our natural environment such as rainy or snowy winds, tornadoes, typhoons, air and water pollution, volcanic activities etc., but also are working processes in a variety of conventional and nuclear power plants, combustion engines, propulsion systems, flows inside the human body, oil and gas production and transport, chemical industry, biological industry, process technology in the metallurgical industry or in food production etc. The list is by far not exhaustive. For instance everything to do with phase changes is associated with multi-phase flows. The industrial use of multi-phase systems requires methods for predicting their behaviour [5].
The contemporary presence of different phases is common in many applications. We can perform a main distinction with macro-areas

wherein we can highlight characteristic applications:

- Power Systems: *boiler, water nuclear reactors, internal combustion engines, Rankine cycle power plants, etc.*;
- Heat Transfer Systems: *heat exchangers, evaporators/condensers, dryers, spray cooling towers, etc.*;
- Process Systems: *extraction/distillation units, fluidized beds, chemical reactors, phase separators, scrubbers, atomizers, stirred reactors, porous media, etc.*;
- Lubrication System: *bearing colling by cryogenics, two-phase flow lubrication, etc.*;
- Environmental Control: *air conditionsers, treatement plants, separators, air pollution controls, etc.*;
- Biological Systems: *blood flow, capillary transoport, nasal flow, cardiovascolar system, etc.*.

As can be observed from the previou list, there are several applications which deal with multiphase flows. Nevertheless all of them are governed by the same physical laws of transport of mass, momentum and energy. One of the main disctinction is the lenghtscale of involved phenomena. The interface between phases, in fact, will assume different shape and size as a function of specific application. Clearly, by varying the characteristic length and timescale a different numerical method should be used in order to better fit the specific interfactial interaction. As example, in the following table some characteristic test cases will be presented with characteristic parameters useful for determining the method adopted in the solution.

| Application | Example | Pressure | Density Ratio |
|---|---|---|---|
| *Secondary BreakUp* | Droplet BreakUp | High | Moderate |
| *Primary BreakUp* | Jet BreakUp | Moderate | High/Moderate |
| *Environmental Flows* | River/fall | Low | High |

Table 1.1: Different multiphase applications in engineering field.

Starting from previous table 1.1 it is clear that specific implementation procedures have to be developed according to the specific problem. For example, a diesel spray, which in reality comprises a large number of droplets, is not represented directly, but can be modelled by a changing Monte-Carlo population of sample droplets. This allows each droplet's behaviour to be described separately by a set of ordinary differential equations for the conservation of mass, energy and momentum. Usually, the following detailed spray processes are modelled: atomization, turbulence, dispersion and modulation, drop breakup and collision, spray-wall interactions, and inter-phase transfer of mass, momentum and energy. The solution strategy for the continuous phase could be based on the finite volume method. On the other hand, a bigger lenghtscale problem, like an environmental flow, can be studied with a different approach, for example with Volume Of Fluid (VOF) method which allows evaluating the portion of every cell occupied from the liquid phase, leaving unsolved the gas portion of the domain. An example of fuel atomization and breakup [6] and VOF approach is reported in figure 1.1.

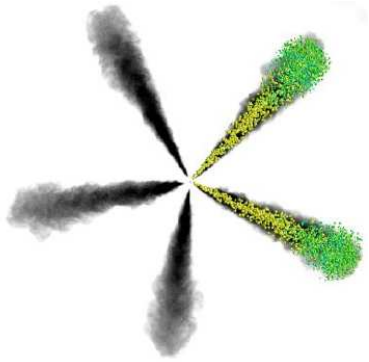

Figure 1.1: A numerical-experimental comparision of secondary breakup in a Diesel Engine Injection.

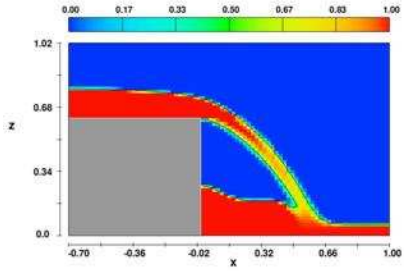


Figure 1.2: An example of VOF approach, *www.flow3d.com.*

Consequently, numerical methods for the investigation of their complex behaviour is in constant demand. However, the task of simulating multi-phase flows is very challenging, due to the inherent complexity of the involved phenomena (emergence of moving interfaces with complex topology, droplet collision and break-up), and represents one of the leading edges of computational physics [4]. As a matter of fact, a general computational approach encompassing the full spectrum of complexity exposed by multiphase flows is still not available. In the recent past, the evolution of computational capabilities allowed reaching a high level of precision in simulating fluid-dynamics problems. As a consequence a lot of models have been written in order to characterize the interactions bewteen different phases especially in the interface region. The numerical methods based on the traditional continuum approach (i.e. Navier-Stokes with closure relationships) are

usually based on rather complex correlations and often require transient solution algorithms with very small time steps. In the last two decades, a new class of mesoscopic methods, based on minimal lattice formulation of Boltzmann kinetic equation, have gained significant interest as an efficient alternative to continuum methods based on the discretisation of the NS equations for non ideal fluids [7].

Before characterizing multiphase flows dynamics, the prior definition of governing equation for incompressible single-phase fluid should be reported. Thus, in this section, the governing dynamic equation will be derived for an incompressible fluid (valid in the range of applicability of LBM), [4, 8, 9, 1, 10].
More specifically, a flow is completely determined if the velocity vector $\mathbf{u}$ and the thermodynamic properties (pressure $p$, density $\rho$ and temperature $T$) are known in every point of the fluid domain. These quantities, the three velocity components and the three thermodynamic variables, are mandatory in order to describe the flow. This can be done by solving the conservation equations for mass, momentum, and energy and the thermal equation of state, which connects the thermodynamic variables with each other. Liquids can be considered as incompressible, as well as gases flowing at low speeds. In the following pararagraph the derivation of continuity equation will be carried out under the assumption of incompressible flow.

## 1.2 The Continuity Equation

In a generic volume $V(t)$, which can be variable in time, with a closed surface $A(t)$, the mass of a flowing medium must be constant,

as highlighted in the following equation:

$$\frac{Dm}{Dt} = \frac{d}{dt}\int_{V(t)} \rho dV = 0 \tag{1.1}$$

Re-writing equation 1.1 in terms of total derivatives:

$$\frac{d}{dt}\int_{V(t)} \rho dV = \lim_{\Delta t \to 0}\left[\frac{1}{\Delta t}\left(\int_{V(t+\Delta t)} \rho\left(t+\Delta t\right) dV - \int_{V(t)} \rho\left(t\right) dV\right)\right] \tag{1.2}$$

After some analytical manipulations the previous equations 1.1 and 1.2 can be rewritten as follows:

$$\frac{d}{dt}\int_{V(t)} \rho dV = \int_{V(t)}\left[\frac{\partial \rho}{\partial t} + \nabla \cdot (\rho \mathbf{v})\right] dV = 0 \tag{1.3}$$

The previous equation is equal to 0 only if the integrand is identical to 0 everywhere in the domain. Hence,

$$\frac{\partial \rho}{\partial t} + \nabla \cdot (\rho \mathbf{v}) = 0 \tag{1.4}$$

which is the continuity equation.

## 1.3 The Navier-Stokes Equation

The conservation of the momentum equation can be recast by evaluating the equilibrium of forces on a volume of fluid. In a closed volume, the variation in the time of the momentum is equal to the sum of external forces acting on the volume itself.

$$\frac{D}{Dt}\int_{V(t)} \rho \mathbf{v} dV = \sum \mathbf{F} \tag{1.5}$$

Though simple operations, as done before for the continuity equation, the left-hand side of this equation can be rearranged as follows:

$$\begin{aligned}\frac{d}{dt}\int_{V(t)}\rho\mathbf{v}dV &= \int_{V(t)}\left[\frac{\partial\rho\mathbf{v}}{\partial t}+\nabla\cdot(\rho\mathbf{v}\mathbf{v})\right]dV = \\ &= \int_{V(t)}\rho\left[\frac{\partial\mathbf{v}}{\partial t}+(\mathbf{v}\cdot\nabla)\,\mathbf{v}\right]dV\end{aligned} \tag{1.6}$$

The right-hand part of eq. 1.5 usually contains two different contributions: the gravitational force (eq. 1.7), and the surface force, resulting from the stress tensor $\bar{\bar{\sigma}}$ (eq. 1.8).

$$\mathbf{F}_g = \int_{V(t)}\rho\mathbf{g}dV \tag{1.7}$$

and

$$\mathbf{F}_\sigma = -\int_{A(t)}(\mathbf{n}\cdot\bar{\bar{\sigma}})\,dA \tag{1.8}$$

The term $(\mathbf{n}\cdot\bar{\bar{\sigma}})$ is the vector product of the normal vector $\mathbf{n}$ and the stress tensor $\bar{\bar{\sigma}}$. The momentum equation reads:

$$\int_{V(t)}\rho\left[\frac{\partial\mathbf{v}}{\partial t}+(\mathbf{v}\cdot\nabla)\,\mathbf{v}\right]dV = \int_{V(t)}\rho\mathbf{g}dV - \int_{V(t)}(\nabla\cdot\bar{\bar{\sigma}})\,dV \tag{1.9}$$

Again the integral is null only if the integrand is everywhere equal to zero, thus:

$$\rho\left[\frac{\partial\mathbf{v}}{\partial t}+(\mathbf{v}\cdot\nabla)\,\mathbf{v}\right] = \rho\mathbf{g} - (\nabla\cdot\bar{\bar{\sigma}}) \tag{1.10}$$

The stress tensor assumes generically the following form:

$$\bar{\bar{\sigma}} = \begin{pmatrix}\sigma_{xx} & \tau_{xy} & \tau_{xz}\\ \tau_{yx} & \sigma_{yy} & \tau_{yz}\\ \tau_{zx} & \tau_{zy} & \sigma_{zz}\end{pmatrix} \tag{1.11}$$

For an incompressible flow with a constant dynamic viscosity $\mu$ the Navier-Stokes equation are reduced to:

$$\begin{aligned}\rho\frac{Du}{Dt} &= -\frac{\partial P}{\partial x} + \mu\nabla^2 u + \rho g_x \\ \rho\frac{Dv}{Dt} &= -\frac{\partial P}{\partial y} + \mu\nabla^2 v + \rho g_y \\ \rho\frac{Dw}{Dt} &= -\frac{\partial P}{\partial z} + \mu\nabla^2 w + \rho g_z\end{aligned} \tag{1.12}$$

The previous formulation of mass conservation 1.1, valid for a single-phase fluid must be extended to the case of multi-phase fluid. In that case, the total mass of the mixture must be conserved, [11], it is not required the conservation of every species, being possible mass fluxes and changes of state between different components/phases. However it is possible to write the conservation law for every *k-th* species as written in the following equation:

$$\frac{\partial \rho_k}{\partial t} + \nabla \cdot \rho_k \mathbf{u}_k = 0 \tag{1.13}$$

where $\mathbf{u}_k$ and $\rho_k$ represent respectively the velocity and the density of the *k-th* species. The mixture density will be evaluated as the sum of the single densities $\rho = \sum_k \rho_k$. By referring to the barycentric velocity, evaluated as $\rho\mathbf{u}_k = \sum_k \rho_k \mathbf{u}_k$, which describes the motion of a fluid element, the previous equation 1.13 becomes:

$$\frac{\partial \rho_k}{\partial t} + \nabla \cdot \rho_k \mathbf{u} = -\nabla \cdot \mathbf{j}_k \tag{1.14}$$

where $\mathbf{j}_k$ is the relative current of the *k-th* species, $\mathbf{j}_k = \rho_k (\mathbf{u}_k - \mathbf{u})$. This parameter takes into account all the dynamic effects due to the missmatch in velocities between different species.

## 1.4 Dimensionless Parameters

In the following analysis many dimensionless groups will be used. Thus, it is useful to introduce them at this time with an explanation of their physical meaning. Moreover, the use of dimensional analysis and dimensionless groups is a well-established practice in fluid dynamics. The starting point is the definition of the length scale characteristic of each problem, such as particle size, duct diameter, and others. The spatial scale of each problem can be therefore represented by a characteristic length $L$. A similar definition can be adopted for characteristic time scale $\tau$ and velocity scale $\mathbf{u}^*$. We introduce dimensionless variables $x^*$, $t^*$, and $\mathbf{u}^*$ by writing:

$$\begin{aligned} x &= Lx^* \\ t &= \tau t^* \\ \mathbf{u} &= U\mathbf{u}^* \end{aligned} \tag{1.15}$$

The eq. 1.15 gives an idea about relathionships between physical quantities and dimensionless parameters.
After having fixed these characteristic quantities, introducing the dimensionless numbers used in the computation is possible. First of all it must be underlined that every number evaluated for physical quantities can be rewritten for the dimensionless parameters *without* modifying the physical meaning and the structure of the dimensionless number itself.
The first dimensionless number to be introduced is the *Reynolds* number, which is the ratio between inertial and viscous forces:

$$Re = \frac{\rho LU}{\mu} = \frac{LU}{\nu} \tag{1.16}$$

where $\mu$ and $\nu$ represent the dynamic and kinetic viscosity respectively and $L$ is the characteristic length-scale of the case-study.
Another important number, which rules the interaction between inertial forces and surface tension effects, is the *Weber* number defined as follows:

$$We = \frac{\rho L U^2}{\sigma} \tag{1.17}$$

where $\sigma$ is the surface tension acting between the two different phases. In order to describe the interactions between viscous stresses and surface tension effects, the *Ohnesorge* is defined as:

$$Oh = \frac{\mu}{\sqrt{\rho L \sigma}} \tag{1.18}$$

Another important parameter is the *Eotovos* number, known also as *Bond* number, which may be regarded as proportional to buoyancy force divided by surface tension force:

$$Eo = \frac{a \Delta \rho L^2}{\sigma} \tag{1.19}$$

where $a$ is the acceleration magnitude and $\Delta\rho$ is the difference in densities between of liquid and vapor phases.

## 1.5 Numerical Methods for Multiphase Flows

To numerically model a multiphase flow, it is often important to use separate formulations for the different phases. It is possible to define the particle phase as the phase that consists of bubbles, particles, or drops, and the continuous phase as the fluid in which these particles

are generally immersed. Thus, the particles can be composed of solid, liquid, or gas, whereas the continuous fluid can be a liquid or a gas.

The coupling between the particle motion and its surroundings can be used to classify the character of the multiphase flow, and helps determining appropriate numerical techniques. Starting from the concentration of the particles two principal regimes can be determined, the dispersed and the dense flows, figure 1.3 In the dispersed flow the fluid-particle interaction plays a relevant role, and usually the particles' trajectories tend to be aligned with the continuum fluid motion. When the particle concentration becomes higher and the particle-particle interactions become dominant, the flow can be regarded as "dense". In the case of dispersed flow, four different interactions can be considered:

- one-way - the dispersed phase motion is influenced by the continuous one, but not vice-versa;
- two-way - the dispersed phase influences the continuous motion though interfacial phenomena;
- three-way - where the particle wakes influence other particles' motion;
- four-way - the collision between particles influences the overall particle interaction.

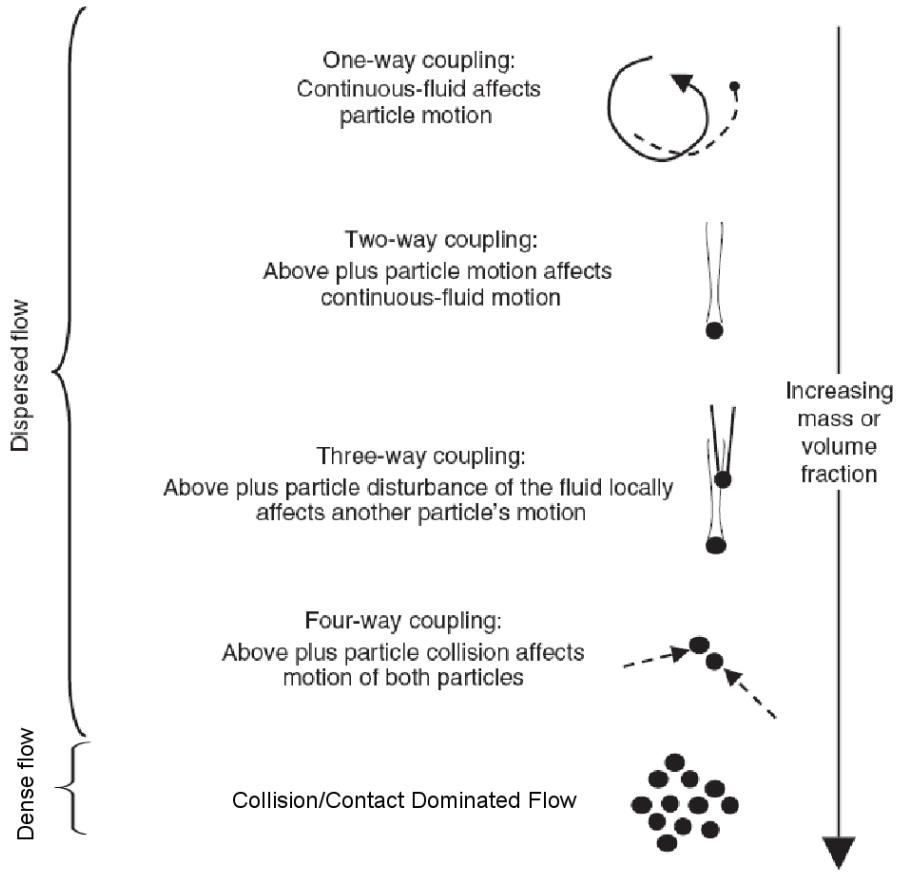


Figure 1.3: A graphic definition for fluid dilution. The definition of dilution degree is useful for the definition of solving method, [1].

On the other hand, dense flows are usually characterized only by the four-way coupling, as shown in fig. 1.3.
Moreover, the above classification can be used in order to differentiate various numerical formulations. For example in the case of one-way

coupling, where the particle motion does not influence the continuous phase, this can be solved independently from the particles' solution with models function of the Reynolds number.

Continuous-flow simulations are typically carried out with an Eulerian approach, being the most computationally efficient description for solution, particularly for steady flows. In the Eulerian method, a domain of fluid is considered where the domain motion and boundaries are selected based on convenience as a function of the specific application. Different spatial discretization for the fluid characteristics (velocity, temperature, and pressure) are possible, and they can be used with *finite-difference*, *finite-volume*, and *finite-element* treatments. Although less common than the Eulerian treatment, the continuous fluid is sometimes treated in a Lagrangian manner. In addition, there are some hybrid methods such as the *Arbitrary - Lagrangian – Eulerian* (ALE) technique. In general, the treatments of continuous-phase flows are subject to standard resolution convergence issues (spatial and temporal) to satisfy the governing differential equations.

Another important characterization of the continuous-phase flow is if it is assumed to be inviscid or viscous, having this parameter a deep influence on the numerical solution of partial differential equations (PDEs). For inviscid flows, the quantitative effects of friction over surfaces and dissipation of vorticity are negligeable for the desired flow properties. However, an inviscid continuous-phase solution does not preclude the effects of viscosity with respect to particle motion. Viscous flows require inclusion of shear stresses in the PDE formulation and thus in the numerical solution. These flows are primarily classified as *laminar*, *transitional*, or *turbulent* as a function of the Reynolds number.

## 1.6 Numerical Methods for Continuous-Phase Turbulent Flows

Due to the high computational requirement, the simulation of high Reynolds flows requires a kind of averaging procedure for the PDEs, or at least for the smallest-scale structures, in order to obatin results in an acceptable time with feasible computational resources. Of course, this procedure involves some artifacts, and thus this averaging should be avoided, or minimized as much as possible. The degree of averaging can vary, as a function of the physics of interest. An important distinction is whether none, some, or all of the vortices (eddy structures) can be resolved. However, two main groups can be defined for turbulent flows: 1) time-averaged simulations (no structures resolved) and 2) eddy-resolved simulations (some or all of the structures resolved).
*Time-averaged* simulations employ a time average with respect to the turbulence, and only mean statistics are predicted. Moreover, only one average turbulence length scale and time scale can be identified, and no eddy structures are solved. The most common example is the Reynolds-averaged technique, where all flow variables are individually time-averaged and the resulting equations are generally called the *Reynolds Averaged Navier Stokes* (RANS) equations.
*Eddy-resolved* simulations predict at least some of the biggest eddy structures, thus some of the turbulent eddies are resolved. This category includes *Direct Numerical Simulations* (DNS) where the turbulence is described for all eddies' wave-numbers. This category also includes *Large-Eddy Simulations* (LES) where the turbulence is only resolved up to some threshold wave-number, beyond which a subgrid scale is employed. Morever, hybrid RANS–LES techniques may be

adopted, wherein only the separated flow regions are treated with an LES approach while attached flow regions are treated with a RANS approach.
Eddy-resolved techniques can capture the principal structures associated with the turbulence, as a matter of facts they are more accurate than the time-averaged techniques in terms of turbulent diffusion and other statistical flow features. As can be seen in figure 1.4, the choice of solving eddies has a valuable and apparent effect on the dispersed-phase predictions. The variety of wavenumbers simulated by these

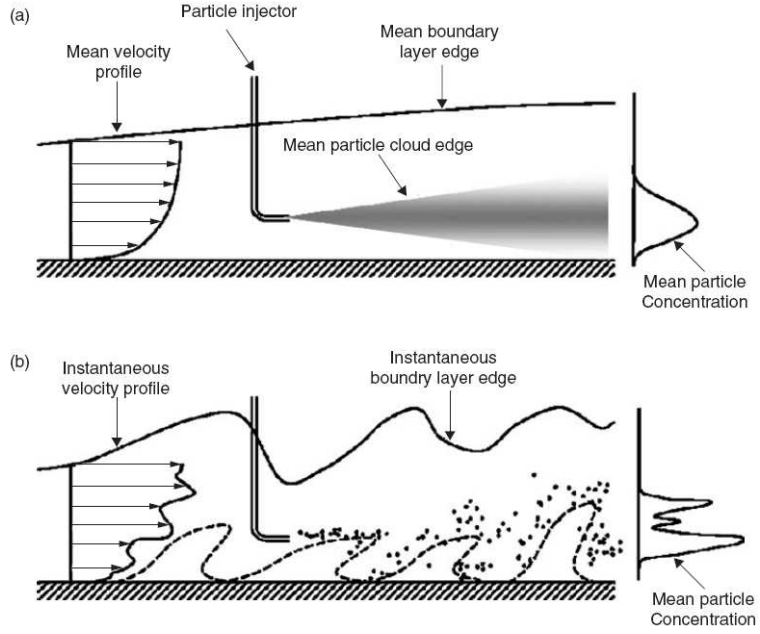


Figure 1.4: Different solutions for a turbulent boundary layer for a time-averaged scheme (a) and an eddy-resolved approach (b).

different techniques ranging from RANS -just an integral length-scale-

, LES -dynamics of the most energetic eddies- to DNS -the dynamics of all the eddies- is schematically represented in Figure 1.5. However, eddy-resolved formulations require a harsh price in terms of higher computational resources, both CPU memory and time.

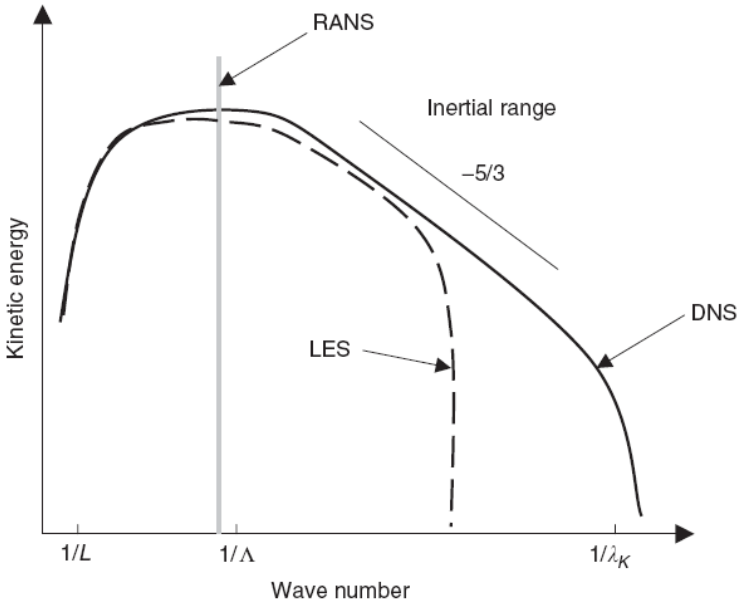


Figure 1.5: Scheme of turbulence spectrum for the RANS, LES and DNS approaches.

### The RANS Model

The first step of the RANS model is the separation of velocities into two different contributions: the steady end the fluctuating component:

$$\mathbf{u}\left(\mathbf{x},t\right)=\overline{\mathbf{U}}\left(\mathbf{x}\right)+\boldsymbol{u}^{'}\left(\mathbf{x},t\right) \tag{1.20}$$

where $\bar{\mathbf{U}}(\mathbf{x})$ represents the time-averaged velocity over a time period greater than the characteristictimescale. According to the new velocity definition, the momentum equation in the extended formulation can be rewritten for RANS turbulent methods, as follows:

$$\frac{\partial \mathbf{U}}{\partial t} + \nabla \cdot (\mathbf{U}\mathbf{U}) + \nabla \cdot \left(\overline{\mathbf{u}'\mathbf{u}'}\right) = -\frac{1}{\rho}\nabla P + \nu \nabla^2 \mathbf{U} \tag{1.21}$$

The primary aim of RANS models is to model (numerically and empirically) the Reynolds stress $\left(\overline{\mathbf{u}'\mathbf{u}'}\right)$ terms, which appear in the source term of the momentum transport equations, through some of the mean velocity features. This highly non-linear term will be modeled via different techniques. In fact, for turbulent multiphase simulations, two-equation models ($k-\epsilon$, $k-\omega$, and $q-\omega$) are currently used, because they describe two independently varying properties of the turbulence; for example, the turbulent kinetic energy (TKE) $k$ and the turbulent dissipation $\epsilon$.

### The Eddy-Solving Approach

For the alternative approach to time-averaging, the eddy-resolved technique, many descriptions are possible. These can be arranged in order of increasing complexity, physical representation, and required computational resources.

*Hybrid RANS–LES models* - Different numerical treatments are designed in order to treat a part of the computational domain using a RANS formulation coupled with a LES formulation. The basic concept is to allow for a one-equation RANS treatment in the attached boundary layer regions and LES treatment in the separated and free-shear

flow regions. This is achieved by using a wall distance to spatially separate the RANS and LES regions.

*Large Eddy Simulations* (LES) - The governing equations are obtained by a low-pass spatial filtering of the Navier–Stokes equations such that all the velocity components are separated into their resolved (unfiltered) and unresolved (filtered) components. Similarly to RANS approach, the velocity components for the spatial filtering process are given as $\mathbf{u} = \overline{\mathbf{U}} + \boldsymbol{u}^{'}$ , where some modeling is required for the fluctuations that are at the subgrid level (unresolve eddies). Ideally, this spatial filtering is applied at sufficiently small scales so that the filtered turbulence is at or below the inertial range and thus nearly homogeneous and isotropic, such that Smagorinsky-type [12], models can be reasonably employed. However, the inertial range develops for only very high Reynolds numbers [13], as a consequence that spatial filtering can be a complex phenomenon that sometimes maks difficult to provide accurate and robust predictions of the subgrid turbulence. The LES technique is perhaps the most promising for low to moderate Reynolds number engineering flows.

*Direct Numerical Simulations* (DNS) - The governing equations in this case are the full time-dependent Navier–Stokes equations. Typically, the high resolution required for grid-independent solutions results in low Reynolds numbers, simple geometries, and use of spectral methods if flow discontinuities (shock waves, concentration fronts, etc.) are not critical to the flow physics. The primary advantage of DNS is that all the eddy structures are fully resolved and no (artificial) turbulence modeling is necessary. However, for most engineering flows, DNS computations are simply too computationally intensive.

## 1.7 The Particle-Phase Flow Methodologies

The methodologies used for the solution of particle-phase problems -with the presence of solid particles, droplets or bubbles- may involve either Eulerian or Lagrangian approaches. In the first option, the Eulerian approach, we may define two approaches the mixed or the point-force, as well as for the Lagragian schemes we may define point-force or resolved-surface approaches.
In the figure 1.6 a schematization of the different approaches is reported.

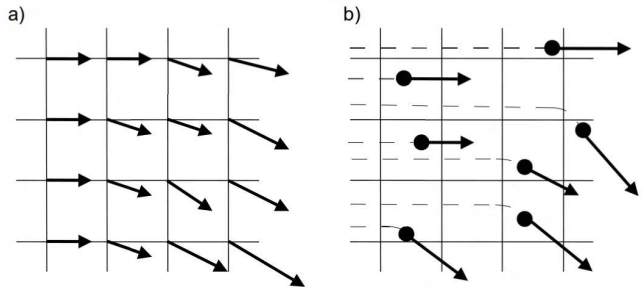


Figure 1.6: A graphic comparison between Eulerian (a) and Lagrangian (b) approaches.

### The Lagrangian Approach

In the Lagrangian technique using a point-force approach every fluid particle is described as a single-indipendent point moving with its own velocity, [4, 5, 10]. In this case, individual particle trajectories are computed with ordinary differential equations [ODEs] based on

the moving particle location, while the continuous-phase flow is typically treated in an Eulerian sense. For a large number of particles, computational packs or parcels can be used where each pack represents a cloud of several particles with the same characteristics. The size of the parcel should be much less than the continuous-phase local grid resolution ($\Delta x$).
If a resolved-surface approach is used, the detailed flow around each particle must be solved to a high resolution. Then, the flow solution can be numerically integrated over the surface to obtain the momentum interaction of the fluid on the particle and viceversa. Thus the Lagrangian method updates the particle The unwanted consequence of the resolved-surface technique is that many continuous-fluid grid points around each particle are computationally required, hence that simulation of many particles will generally be impractical on even the most advanced computers.

The previous figure 1.7 better explains the main differences between these two Lagrangian techniques. As can be seen in the case of point-force the particle surface effects on the continuum are neglected, as well as some models for drag and lift are required. On the other hand, for the resolved-surface approach the interfacial interactions are better described and this scheme seems to be optimal for complex particle shapes. As a consequence, while the first approach allows simulating problems with a large number of particles, the second one, despite being more accurate, requires higher CPU capabilities per particle.

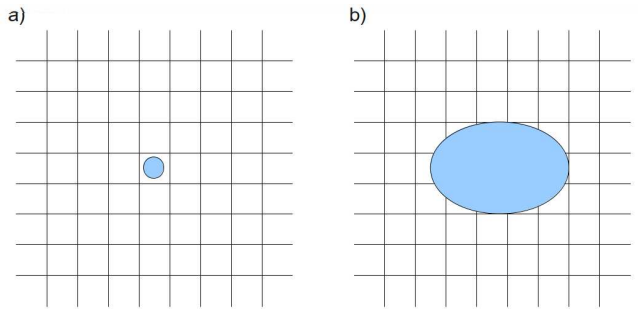


Figure 1.7: Different representations for particle treatment. The filled area represents the particle, while the black and white grid is the computational domain. The two approaches are shown: (a) Point-force approach ($d < \Delta x$) and (b) resolved-surface ($\Delta x << d$).

### The Eulerian Approach

The Eulerian technique, [4, 8, 10] applied to dispersed phase generally treats the particles in the same manner of the continuum phase, using the same discretization too. In the Eluerian approach with point-force method there are several particles per control volume grouped in different packs which share the same characteristics.
A more interesting classification for this approach is the one refered to mixed- or separated-fluid. In the first case the particles and the continuous are *locally in equilibrium* (kinetical and thermal). On the other hand, for separated fluid treatment, the two phases, continuous and dispersed, are assumed to belong to separate, but intermixed, continua. Thus two momentum equation are required, one for the carrier fluid and another for the particles' phase.

## 1.8 An Overview on Numerical Methods

In the following section a deeper analysis on numerical techniques for multiphase flows will be carried out. More specifically some aspects of discretization algorithms will be highlighted in order to asses a global overview of numerical possibilities to analyze multiphase flows.

### 1.8.1 DNS of Finite Reynolds Flows

As pointed out in the previous section, the DNS represents the *direct* numerical simulation of a fluid dynamic problem, [8, 14]. Thus, there are no modeling issues beyond the continuum hypothesis. The flow within each phase and the interactions at the interface are found by solving the governing conservation equations. In order to capture all the physical details grids which are finer than any physical length-scale, as well as time steps which are shorter than time-scale in the problem have to be used. The flow field produced by direct numerical simulations is highly detailed, allowing an exploration of the mechanisms which govern multiphase flows and extracting information not available in any other way. Using this numerical method it is possible to obtain extremely accurate solutions over a large range of operating conditions. The study of single bubble/droplet can be eqsily managed, while the interactions of a few bubbles, drops, or particles are a more challenging computational issues.
For a large number of multiphase flow problems the flow speeds are relatively low and it is possible to treat the flow as incompressible, due to the small value of Mach number. Theorically, there is no explicit equation for the pressure and therefore this has to be found in the overall solution process. The standard way to integrate the

Navier–Stokes equations, the so called *projection method*, solves the velocity field without accounting for the pressure, as a results a field that is in general not divergence-free is obtained. The pressure necessary to make the velocity field divergence-free is then found and the velocity field corrected by adding the pressure gradient.
The time derivative can be evaluated by using a first-order explicit integration scheme, but there are other methods which use higher order differentiation schemes. The continuity equations 1.3 and 1.10 are integrated on time as follows:

$$\frac{\mathbf{u}^{n+1}-\mathbf{u}^{n}}{\Delta t}+\mathbf{A}_h\left(\mathbf{u}^{n}\right)=\frac{1}{\rho}\nabla_h P+\nu\mathbf{D}_h\left(\mathbf{u}^{n}\right)+\mathbf{f}_b^n \tag{1.22}$$

and

$$\nabla_h\cdot\mathbf{u}^{n+1}=0 \tag{1.23}$$

where the superscripts $n$ and $n+1$ denote respectively variables evaluated at the beginning and at the end of timpestep $\Delta t$. $\mathbf{A}_h$ is the numerical approximation of the advection term, $\mathbf{D}_h$ of the diffusive term and $\mathbf{f}_b^n$ of any forcing term eventually present in the formulation. In the projection method the momentum equation is split into two parts by introducing a teemporary velocity $\mathbf{u}^*$ defined as $\mathbf{u}^{n+1}-\mathbf{u}^n=\mathbf{u}^{n+1}-\mathbf{u}^*+\mathbf{u}^*-\mathbf{u}^n$. Thus the first predictor step is evaluated in terms of $\mathbf{u}^*$ by neglecting the effects of pressure:

$$\frac{\mathbf{u}^{*}-\mathbf{u}^{n}}{\Delta t}=+\mathbf{A}_h\left(\mathbf{u}^{n}\right)+\nu\mathbf{D}_h\left(\mathbf{u}^{n}\right)+\mathbf{f}_b^n \tag{1.24}$$

and the second projector step is written as:

$$\frac{\mathbf{u}^{n+1}-\mathbf{u}^{*}}{\Delta t}=-\frac{1}{\rho}\nabla_h P^{n+1} \tag{1.25}$$

In order to eliminate the velocity $\mathbf{u}^{n+1}$ from equation 1.25 and to evaluate the pressure, one can use eq. 1.23 resulting the Poisson equation:

$$\frac{1}{\rho}\nabla_h^2 P^{n+1} = \frac{1}{\Delta t}\nabla_h \cdot \mathbf{u}^* \tag{1.26}$$

being the density constant after having found the pressure, the equation 1.25 is used to find the projected velocity at timestep $n+1$. The described method is evidently explicit and as a consequence is subjected to stringent timestep limitations. With a standard second order approximation for spatial derivatives, the stability requires the followng limitation on the timestep size $\Delta t$

$$\Delta t < C_\nu \frac{h^2}{\nu} \tag{1.27}$$

where $C_\nu$ is 1/4 or 1/6 respectively for a two- or three-dimensional flow, and $h$ the grid spacing.
On the other hand, the spatial discretization is usually based on a finite volume approach, in other words, the control volume is divided into a series of smallest elements where the velocity is averaged in every little volume. A standard procedure commonly used in order to increase the stability of the method is the evaluation of velocity in every node of the control volume, while the pressure is evaluated only in the volume centroid. This technique is usually named *staggered* grids and, as pointed out above, is necessary in order to avoid some stability issues. The following figure 1.8 better points out the staggered approximation now described.

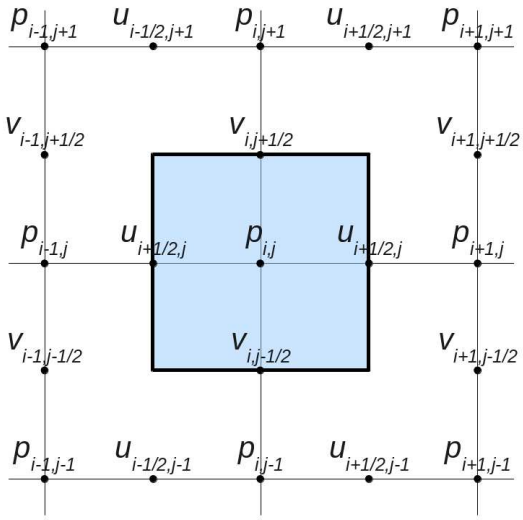


Figure 1.8: A graphical representation of staggered grid for a two-dimension application. The pressure is evaluated at the centroid $(i, j)$ while the velocities are evaluated at external nodes.

For example the continuity euqation for an incompressible flow can be approximated as follows:

$$\frac{u^{n+1}_{i+1/2,j} - u^{n+1}_{i-1/2,j}}{\Delta x} + \frac{v^{n+1}_{i,j+1/2} - v^{n+1}_{i,j-1/2}}{\Delta y} = 0 \qquad (1.28)$$

where the superscript $n+1$ is referred to the time integration procedure and the subscript to the spatial discretization.

### 1.8.2 The One Fluid Approach

Another numerical approach, the *One Fluid Approach* -OFA-, is based on the solution of a single set of equations for the whole multiphase system, composed at least of two different phases, [1, 8, 10].

However, in that case, some external forcing terms have to be added to the starting set of equations in order to take into account the differences between materials and to model all the interfacial phenomena -surface tension-. Being these terms concentrated at the boundary between the different fluids, it is useful to reproduce them via delta ($\delta-$) functions. When the equations are discretized, the $\delta$-functions must be transported/solved with the rest of the equations. The various fluids can be identified by a step (Heaviside) function $H$ which is 1 where a particular fluid is located -i.e. the heaviest one- and 0 elsewhere -i.e. for the sorrounding air-.
It is useful to indroduce now a simple example which highlights the core of this procedure. Thus, if the densities of two phases are constant the local density can be expressed as:

$$\rho\left(x,y\right)=\rho_1 H\left(x,y\right)+\rho_0\left[1-H\left(x,y\right)\right] \tag{1.29}$$

It is useful to derive the gradient as a function of the Heavyside at least for one of the thermodynamic quantities, in order to highlight its formulation before re-writing Navier-Stokes equation for this specific techniqiues. The gradient of density can be derived as described in the eq. 1.30

$$\begin{aligned}\nabla\rho &= \rho_1\nabla H-\rho_0\nabla H=\left(\rho_1-\rho_0\right)\nabla H= \\ &= \Delta\rho\int\delta\left(x-x^{'}\right)\delta\left(y-y^{'}\right)\mathbf{n}^{'}ds^{'}=\Delta\rho\delta\left(n\right)\mathbf{n}\end{aligned} \tag{1.30}$$

Thus, the Navier-Stokes, for the One Fluid approach can be rewritten as follows:

$$\rho\frac{\partial\mathbf{u}}{\partial t}+\rho\nabla\cdot\mathbf{uu}=-\nabla P+\rho\mathbf{f}+\nabla\cdot\mu\left(\nabla\mathbf{u}+\nabla^T\mathbf{u}\right)+\sigma\kappa\delta\left(n\right)\mathbf{n} \tag{1.31}$$

In the equation 1.31, the parameter $\kappa$ is the interface curvature, and $\mathbf{n}$ is the unit vector normal to the surface. As can be noticed, only one equation is used to solve the complex system, and, the different properties are taken into account through step-functions which rule the passage from a phase to another one. This kind of methods allows the users to solve multiphase problems using more or less the same algorithms and discretizations, used for a single phase flow. It is important to notice that, using a step function, the properties have an istantaneous variation along the interface, passing form a value to another of the Heavyside function $H$.

### 1.8.3 The Marker Function

This approach basically starts from the same assumptions done in the previous section about the Heavyside function, [8, 9]. In fact, a marker function $f$ which is 1 for one phase and 0 for the other, is defined. The main difference is that, the marker function is advected through the next equation:

$$\frac{\partial f}{\partial t} + \mathbf{u} \cdot \nabla f = 0 \tag{1.32}$$

The main difference with the previous method is that, solving the eq. 1.32, the interface will be smoothed as well as all the properties function of the local concentration. Differently from the OFA the fuction $f$ assume intermediate values crossing the interface thickness.
As a consequence, advecting a discontinous marker function becomes in sucha way tricky. This procedure is rapidly presented in the following. We can start from a one-dimensional advection equation with a

constant velocity $U > 0$:

$$\frac{\partial f}{\partial t} + U\frac{\partial f}{\partial x} = 0 \tag{1.33}$$

which can be re-writen by introducing $F = Uf$:

$$\frac{\partial f}{\partial t} + \frac{\partial F}{\partial x} = 0 \tag{1.34}$$

In order to discretize the above written equation we can consider a grid with points named as $j-1$, $j$, $j+1$ and so on. A sketch of grid and function advection is presented in figure 1.9.

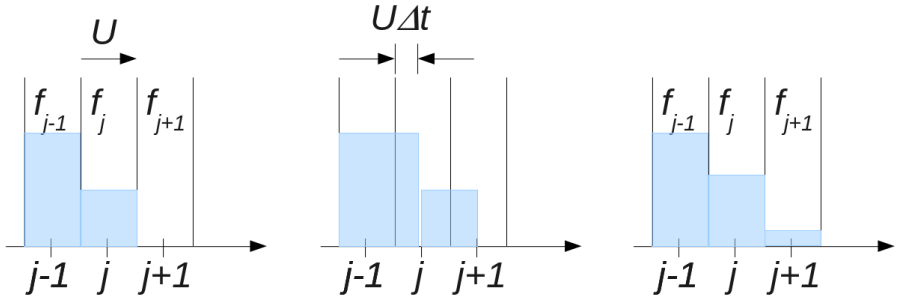


Figure 1.9: Advection of fuction $f$ with a constant velocity $U$ using a first-order upwind scheme. The funcion is assumed to be constant in the cell at the beginning and at the endo of advection timestep.

As can be seen at intermediat sub-step the function $f$ is not constant into thhe cell. The boundaries of the cell are respectivelly at $j \pm 1/2$ where the grid-point represents the center of cells or control volumes. Thus, the average of $f$ into the cell is simply expressed as the mean integral between boundaries:

$$f_j = \frac{1}{h}\int_{j-\frac{1}{2}}^{j+\frac{1}{2}} f\,(x)\,dx \tag{1.35}$$

bieng $h$ the grid spacing. Integrating equation 1.34 in space and time we can obtain:

$$f_j^{n+1} - f_j^n = \int_t^{t+\Delta t} F_{j+\frac{1}{2}} dt - \int_t^{t+\Delta t} F_{j-\frac{1}{2}} dt \tag{1.36}$$

The previous equation 1.36 represents an exact result. The physical meaning of 1.36 is that the value of $f_j$ has increased by the difference in the flux of $f$ *in* and *out* of the control volume. Being the velocity $U$ constant, the $f$ profile is simply advected by shifting it to the right and the time integral of the flux acorss the boundary can be easily computed if the exact shape of $f$ is known. At this point, storing only the mean value of $f_j$, some assuptions can be done about the distribution of $f$ in every cell. By considering a constant value of $f$, equal to the average $f_j$ the time integral can be computed exactly as follows:

$$\int_t^{t+\Delta t} F_{j+\frac{1}{2}} dt = \Delta t U f_j \tag{1.37}$$

As a consequence the average value of $f_j$ can be updated by:

$$f_j^{n+1} = f_j^n - \frac{\Delta t U}{h} \left( f_j^n - f_{j-1}^n \right) \tag{1.38}$$

The advection process can be decomposed in two steps. The first one consists in shifting the solution by $U\Delta t$ to the right and then the solution is averaged in order to recover a uniform distribution of $f$ in each cell, as reported in figure 1.9. The main problem with this approach is that by assuming that the value of $f$ into the cell is equal to the average value and by using this mean value for evaluating the gradients, $f$ starts flowing out of the cell $j$ before it is full. This leads to an apparent *artificial diffusion* quite common in first-order diffusion scheme. This is the reason why higher-order approaches have been proposed.

Between them valuable and quite common is the Lax-Wendroff one. One of the main attempts to generalize advection methos is represented by the Volume of Fluid (VOF) approach, which will be characterized in following chapters.

### 1.8.4 The level-set method

The level-set method, introduced by Osher and Sethian (1988) for multiphase flow simulations, [8, 10, 15], became one of the most used methods for the direct advection of a marker function. The level-set methods make no assumption about the connectivity of the interface. For example, if the interface separating liquid and gas should undergo a topological transition, or form a sharp corner, there is no user intervention or extra coding necessary in order to continue the computation. Besides being robust, level-set methods allow one to accurately represent interfacial quantities such as the interfacial normal and curvature. The level-set function transitions smoothly across the liquid–gas interface, differently from VOF where this phenomenon takes place over one grid cell; therefore standard discretizations of the normal and the curvature using the level-set function can be as accurate as needed.
In the level-set method, the interface separating two phases is represented using level-set function $\phi$. For a binary (gas-liquid) system, we can assume $\phi$ positive in the liquid and negative in the gas,

$$\phi(\mathbf{x}, t) = \begin{cases} +k, & \mathbf{x} \text{ in the liquid} \\ -k, & \mathbf{x} \text{ in the gas} \end{cases} \tag{1.39}$$

where $k$ represents the normal distance to the interface at time $t$.

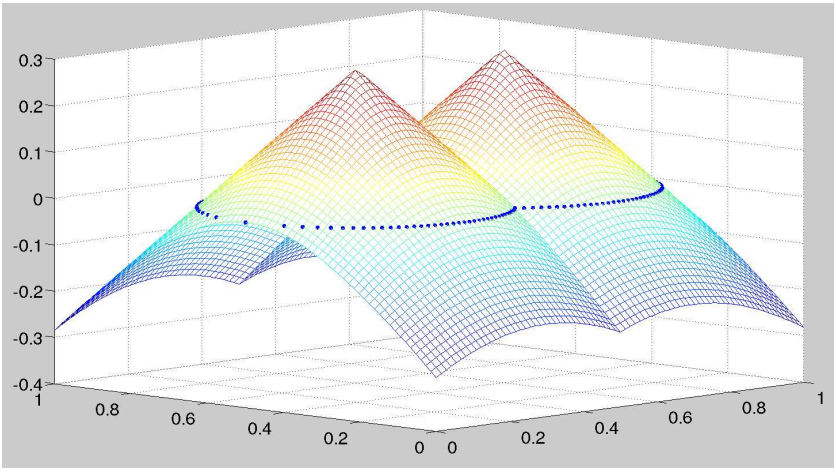


Figure 1.10: Level set representation of an interface, constructed as a distance function and represented with blue *.

In previous figure 1.10 the interface position can be appreciated as well as the function $\phi$ which represents the distance function.
Then the level set fuction is generally advected as follows:

$$\frac{\partial \phi}{\partial t} + \mathbf{u} \cdot \nabla \phi = 0 \tag{1.40}$$

where $\mathbf{u}$ is the fluid velocity. The level set equation can be derived using the assumption that it should be constant along particle paths trajectories, then:

$$\frac{d\phi\left(\mathbf{x}\left(t\right), t\right)}{dt} = 0 \tag{1.41}$$

By combining eq. 1.41 with $d\mathbf{x}\left(t\right)/dt \equiv \mathbf{u}$ we obtain

$$\frac{d\mathbf{x}\left(t\right)}{dt} \cdot \nabla \phi\left(\mathbf{x}, t\right) + \frac{\partial \phi\left(\mathbf{x}, t\right)}{\partial t} = 0 \tag{1.42}$$

which is equal to 1.40. Starting from this equation the level-set equation can be advected by any accurate scheme for hyperbolic equations. While $\phi = 0$ is advected in the right way, the level-set function of the interface wil not remain a distance function. In order to preserve the level-set function as a distance function, at least near the interface, condition necessary for coupling with the fluid equations in multiphase approaches, the level-set function has to be *reinitialized*. In fact, without reinitialization, the magnitude of gradient $|\nabla\phi|$ would assume very large/small values near the zero level-set of $\phi$. This unwanted effect can lead to an overall loss of accuracy of solution. Thus, in reinitialization process $\phi$ is converted into a new level-set function $\phi_a$ which shares with $\phi$ the same zero level set and it is imposed that:

$$|\nabla\phi_a| = 1 \tag{1.43}$$

In conclusion, the above presented VOF method can treat and succesfuly solve breakup and coalescence problems without any special treatment, while the level-set approach is not always capable to do that. However, the last one is significantly simpler than advanced VOF methods and can be easily extended to three-dimensional problems. Moreover, in order to point out other advantages of level-set method we can conclude that it can be coupled with finite element methods or spectral element methods.

# Chapter 2

# The Lattice Boltzmann Method

The Lattice Boltzmann Method provides an alternative way for solving continuum problems on a kinetic basis [16]. The computational method is based on the development of discrete molecular velocity distribution functions on uniform Cartesian lattices with additional diagonal links. Hydrodynamic variables are computed at the nodes as moments of the discrete distribution function, sum overall the allowed directions. The resulting algorithm has been shown to be simple and efficient for computations of incompressible, viscous flows over complex boundaries. An essential advantage of the LBGK method is the ease and accuracy in dealing with complicated boundary geometries. In the range of small to moderate $O(10^2)$ Reynolds numbers, where the flow solution is not too anisotropic, the lattice - BGK method is competitive or even superior to conventional CFD methods if dealing with flows in complex geometries.

## 2.1 The Kinetic Theory

If we consider a group of $N$ molecules moving in a box of volume $V$ at temperature $T$ and mutually interacting via a two-body intermolecular potential $\Psi(\vec{r})$ (with $\vec{r}$ the distance between two particles). If the linear size $s$ of the molecules is much smaller than their mean interparticle distance, $d = (V/N)^{1/3}$, we can consider them as point-like structureless particles. In such case, their dynamics can be considered as governed by the classical Newton equations,

$$\frac{d\vec{x}_i}{dt} = \frac{\vec{p}_i}{m} \tag{2.1}$$

$$\frac{d\vec{p}_i}{dt} = \vec{F}_i, \quad i = 1, \ldots, N \tag{2.2}$$

where $\vec{x}_i$ is the position of the *i-th* particle, $\vec{p}_i = m\vec{v}_i$ is its linear momentum and $\vec{F}_i$ is the total force acting on the *i-th* particle (coming from intermolecular interactions or any external field).
The main problem in solving the above equations is that $N$ is usually in the order of the Avogadro number ($Av \sim 6.022 \cdot 10^{23}$ molecules per mole), far too big for any 'starndard' computer.
Therefore, it appears wise and convenient to deal with the behaviour of the molecule enemble from a statistical point of view. Let's call $f(\vec{x}, \vec{p}, t)$ the distribution function that represents the probability density of finding a particle in $\vec{x}$ with momentum $\vec{p}$ at time $t$. This distribution function is the core object of kinetic theory and, in 1872, the Austrian scientist Ludwig Boltzmann derived an equation which was describing the evolution of $f$ in terms of microdynamic interactions.
The kinetic equation for the one-body distribution function is

$$D_t f = \left[\partial_t + \frac{\vec{p}}{m} \cdot \partial\vec{x} + \vec{F} \cdot \partial_{\vec{p}}\right] f(\vec{x}, \vec{p}, t) = \mathbf{Q}_{1-2} \tag{2.3}$$

In eq. 2.3, the left-hand side represents the streaming motion of the molecules along the trajectories associated withe the force field $\vec{F}$; $\mathbf{Q}_{1-2}$ represents the effect of intermolecular collisions. It is during the collision event that molecules *interact*. The collision operator $\mathbf{Q}_{1-2}$ is a two-body operator and involves a different distribution funcion, $f_{12}$, which expresses the probability of finding a molecule *-1-* in position $\vec{x}_1$ with speed $\vec{v}_1$ and a second molecule *-2-* in position $\vec{x}_2$ with speed $\vec{v}_2$, both at time t. However, the main problem to face up is that eq. 2.3 is not closed. This is due to the fact that the expression of $f_{12}$ calls into play $f_{123}$, which in turns depends on $f_{1234}$, and so on. In order to close eq. 2.3, Boltzmann made the following assumptions:

- **dilute gas**, made by
- **point-like**, structureless molecules, interacting via a
- **short-rangee** two-body potential.

Under those conditions, intermolecular interactions can be described in terms of localized binary collisions, with molecules spending most of their lifespan on free trajectories, in absence of external fields. Thus, the collision term can be split into gain and loss components,

$$\mathbf{Q}_{1-2} = G - L = \int \left(f_{1'2'} - f_{12}\right) g\sigma\left(g, \Omega\right) d\Omega d\vec{p}_2 \tag{2.4}$$

corresponding to direct/inverse collisions taking molecules respectively out/in the volume element $d\vec{v}_1$. $\sigma$ is the differential cross section, which channels the link to the underlying molecular dynamics, since it expresses the number of molecules with relative speed $\vec{g} = g\vec{\Omega}$, around the solid angle $\vec{\Omega}$. The closure assumptions made by Boltzmann says that

$$f_{12} = f_1 f_2 \tag{2.5}$$

which means that there is no correlation between molecules entering a collision (molecular chaos). According to this, eq. 2.3 turns into:

$$\left[\partial_t + \frac{\vec{p}}{m} \cdot \partial\vec{x} + \vec{F} \cdot \partial_{\vec{p}}\right] f\left(\vec{x}, \vec{p}, t\right) = \int \left(f_{1'2'} - f_{12}\right) g\sigma\left(g, \Omega\right) d\Omega d\vec{p}_2 \tag{2.6}$$

With the aim to derive hydrodynamic equations the definition of *local equilibrium* becomes mandatory.
Mathematically, it is defined as a local distribution function $f_{eq}$ such that the collision term is annihilated:

$$\mathbf{Q}\left(f_{eq}, f_{eq}\right) = 0.0 \tag{2.7}$$

which means that $f_{1'2'} = f_{12}$. Taking logarithms, this yelds to $\ln f_{1'} + \ln f_{2'} = \ln f_1 + \ln f_2$.
This means that the quantity $\ln f$ is an additive invariant for what concerns collision, or better, it represents a microscopic property that does not change under the effect of collisions. The immediate consequence is that at thermodynamic equilibrium $\ln f$ must only be a function of dynamic collision invariants, $I(v) = [1, m\vec{v}, mv^2/2]$, that represent the conservation of number, momentum and energy. In this way, $\ln f$ can be written as

$$\ln f = A + B_\alpha v_\alpha + \frac{1}{2} C v^2 \tag{2.8}$$

where $A$, $B_\alpha$, $C$ are five (three components of velocity in space) Lagrangian multipliers carrying the functional dependence on the conjugate hydrodynamic fields $\rho$, $u_\alpha$, $E$ - respectively density, momentum and energy-. These Lagrangian parameters are computed by imposing

the conservation of the following quantities:

$$\begin{aligned} m\int f d\vec{v} &= \rho \\ m\int f v_\alpha d\vec{v} &= \rho u_\alpha \quad \alpha = 1,2,3 \\ m\int f \frac{v_\alpha}{2} d\vec{v} &= \rho e \end{aligned} \tag{2.9}$$

where $\rho$ is the fluid density, $u_\alpha$ the macroscopic flow field and $\rho e$ the energy density. The equilibrium distribution can be expressed in the well known Maxwell-Boltzmann formulation,

$$f_{eq} = \rho \left(2\pi v_T^2\right)^{-D/2} exp\left(-c^2/2v_T^2\right) \tag{2.10}$$

in which $D$ is the number of spacial dimensions, $c$ the magnitude of the peculiar speed, the molecules speed relative to the fluid $c_\alpha = v_\alpha - u_\alpha$ - with $\alpha = 1, \ldots, D$ - and $v_T$ the thermal speed, associated to the fluid temperature $T$, $v_T = \sqrt{\frac{K_B T}{m}}$.

## 2.2 From kinetic approach to Navier Stokes

In order to recast Navier-Stokes from the kinetic formulation the Chapman-Enskog procedure has benn used. This technique is based on a double expansion in the Knudsen number of the two variables $f(\vec{x}, \vec{v}, t)$ -dependent variable- and $(\vec{x}, t)$, the independent space-time variable. The Knudsen number can be calculated by means of $Kn = \frac{\lambda}{L_M}$, in which $\lambda$ represents the mean free path and $L_M$ the shortest scale at which macroscopic variations can be appreciated. According

to the above mentioned Chapman-Enskog approach, it is possibile to write

$$f = f_{eq} + f_{neq} \tag{2.11}$$

where $f_{eq}$ and $f_{neq}$ represent respectively the local equilibrium and the non-equilibrium distribution. The expansion of space-time variables is at the basis of the multiscale methods: according to these, space and time variblaes can be represented in terms of hierarchy of slow/fast scales. The previously discussed hierarchy leads to the following multiscale representation of space-time variables:

$$x = \epsilon^{-1} x_1 \quad t = \epsilon^{-1} t_1 + \epsilon^{-2} t_2 \tag{2.12}$$

In this representation, $x_1$ and $t_1$ represent the linear sound-wave regime, whereas $t_2$ governs the long term dynamics. The multiscale representation in eq. 2.12 leads to the following formulation of the differentail operators:

$$\begin{aligned} \partial_x &= \epsilon \partial x_1 \\ \partial t &= \epsilon \partial t_1 + \epsilon^2 \partial t_2 \end{aligned} \tag{2.13}$$

The Chapman-Enskog representation of the collision operator is

$$\mathbf{Q}\left[f\right] \sim \mathbf{Q}\left[f_{eq}\right] + \epsilon \mathbf{Q}^{'}\left[f_{neq}\right] \tag{2.14}$$

in which the apex $^{'}$ represents the functional derivative with respect to $f$. Since the *0th-order* local equilibrium (the ground state) annihilates the collision operator -as defined above-, it is possibile to write:

$$\mathbf{Q}\left[f\right] \sim \epsilon \mathbf{Q}^{'}\left[f_{neq}\right] \tag{2.15}$$

The previous expansions provide the starting point for all order-by-order subsequent expansions that lead to the macroscopic equations.

In fact, for mass and momentum conservation, it is possible to write, respectively,

$$\epsilon \hat{M}_1 + \epsilon^2 \hat{M}_2 = 0.0 \tag{2.16}$$

$$\epsilon \hat{J}_1 + \epsilon^2 \hat{J}_2 = 0.0 \tag{2.17}$$

At order $\epsilon$, we obain $\hat{M}_1 = 0.0$ and $\hat{J}_1 = 0.0$, that is

$$\partial_{t_1} \rho + \partial_{a_1} J_a = 0.0 \tag{2.18}$$

$$\partial_{t_1} J_a + \partial_{b_1} \int v_a v_b f_{eq} d\vec{v} = 0.0 \tag{2.19}$$

where $J_a = \rho u_a$ is the current density.
The velocity space integral in eq. 2.19 can be solved analitically, yielding $\rho u_a u_b + \rho T \delta ab$: in this way, it is possible to recognize in eqs. 2.18 and 2.19 the *Euler equations* for inviscid flows.
If we consider the second-order equations, they harder to solve, since they invlove cross terms, that can be neglected by using the conditions $\hat{M}_1 = 0.0$ and $\hat{J}_1 = 0.0$, as well as the conservation relations 2.9:

$$\partial_{t_2} = 0.0 \tag{2.20}$$

$$\partial_{t_2} J_a + \partial_{b_1} m \int v_a v_b \left(f_{neq} + \partial_c v_c f_{eq}\right) d\vec{v} = 0.0 \tag{2.21}$$

With these expansions and after some algebra, it is possible to retreive the *Navier-Stokes* equations

$$\partial_t \rho + \partial_a J_a = 0.0 \tag{2.22}$$

$$\partial_t J_a + \partial_b \left(\rho u_a u_b P \delta ab\right) = \partial_b \tau_{ab} \tag{2.23}$$

.

## 2.3 The Bhatnagar Gross Krook model equation

The complicated integral collision operator can be expressed by a simpler expression, due to Bhatnagar, Gross and Krook [17]:

$$\mathbf{Q}_{BGK}[f] = \frac{f - f_{eq}}{\tau} \tag{2.24}$$

in which $f = f_{neq}$ and $f_{eq}$ is a local equilibrium parametrized by the local conserved quantities, that are density $\rho$, velocity $\vec{u}$ and temperature $T$. For what concerns $\tau$, it is the relaxation time to local equilibrium. The drastic simplification associated with $BGK$ is the assumption of a constant value for this relaxction scale, that is a single-time relaxation scheme, in which all modes relax on the same time scale given by $\tau$ -which is directly related to the fluid kinematic viscosity-.

### 2.3.1 Alternative Collision Operators

Other approaches for modeling collision operator are possibile. Between them result noticeable the *Multiple Relaxation Time* (MRT) [18] and the entropic one [19].
In MRT models the rates of relaxation processes owing to collisions of particle populations may be independently adjusted. As a result, the MRT models offer a significant improvement in numerical stability of the LB method for simulating fluids with lower viscosities. It can be shown through the Chapman–Enskog multiscale analysis that the continuum limit behavior of 3D MRT LB models corresponds to that of the macroscopic dynamical equations for multiphase flow.
The entropic method, on the other hand, allows to eliminate or at

least to tame some sumerical instabilities by means of Lyapunov functional. The main idea is to specify an appropriate functional, rather than use a simple discretization of equilibrium distribution. Of course specifying a Lyapunov functional determines the equilibrium distribution, but it also governs the approach to this equilibrium. We can highlight that the presence of a Lyapunov functional allows to reach non linear stability of the model a stronger condition in comparison with the linear stability. The collision operators constructed in that way are really similar in form to the lattice BGK operator, expect that their relaxation parameter may depend on the current state.

## 2.4 Lattice Boltzmann Models

Lattice Boltzmann models are a consistent simplification of Boltzmann's original conceptal view. The key is the reduction of the number of possible particle spatial positions and microscopic momenta from a continuum to just a discrete ensemble; time is discretized into time steps, too. There is a large number of possibile discretizations: Qian et al, [20] provided a whole family of solutions, commonly called $D_nQ_m$, in which $m$ represents the number of speeds and $n$ the dimensions. A schematic representation of theis velocity discretization is reported in the following figure 2.1.

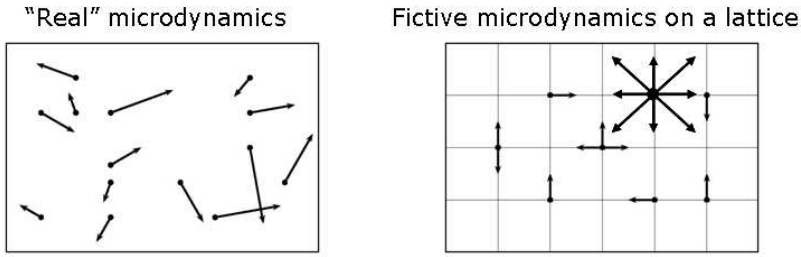


Figure 2.1: Example of velocity discretization.

Among the most used sets, there are $D_1Q_3$, $D_1Q_5$ and $D_2Q_9$. An important asset of such a kind of scheme is that it is possible to consider three dimensions, without introducing significant difficulties: in this case, perhaps the most used sets are the $D_3Q_{15}$, $D_3Q_{19}$ and $D_3Q_{27}$. The presented schemes are graphically reported in Fig. 2.2.

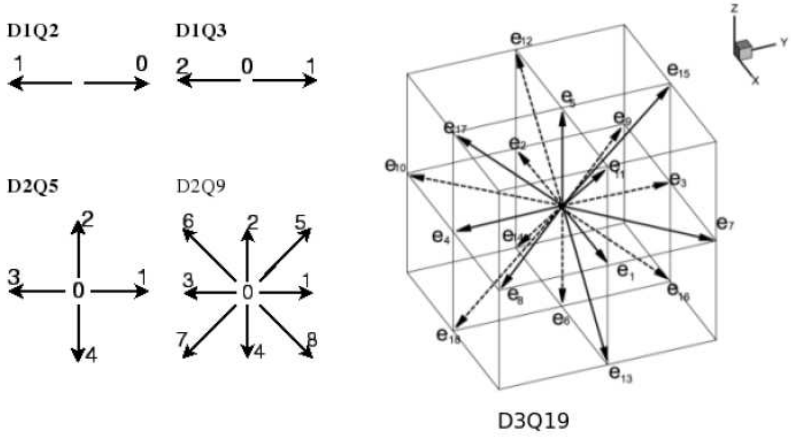


Figure 2.2: Possible Lattice Boltzmann Schemes

Only for example, let's consider the $D_2Q_9$ scheme. In such a scheme, the distribution function $f$ has only nine discrete allowed directions links, instead of being a continuous function. The single $f_\alpha$, then, can be considered as direction-specific fluid densities. According to this, the macroscopic fluid density can be written as

$$\rho = \sum_{\alpha=0}^{8} f_\alpha \tag{2.25}$$

The macroscopic velocity $\vec{u}$ can be retreived from the set of lattice microscopic velocities $\vec{c}_\alpha$. In the $D_2Q_9$ scheme, the velocity magnitudes $\vec{c}_\alpha = 1$ for $\alpha = 1, \ldots, 4$ and $\vec{c}_\alpha = \sqrt{2}$ for $\alpha = 5, \ldots, 8$ and the macroscopic velocity is given by

$$\vec{u} = \frac{1}{\rho} \sum_{\alpha=0}^{8} f_\alpha \vec{c}_\alpha \tag{2.26}$$

The relaxation towards local equilibrium is reached by means of a series of events, called streaming and collision: during the streaming the molecules do not interact, according to the Boltzmann hypothesis, while in the collision event they exchange momentum. In general, the equilibrium distribution function can be expressed as the low Mach expansion of a multi-energy Maxwellian:

$$f_\alpha^{eq}(\vec{x}) = w_\alpha \rho(\vec{x}) \left( 1 + \sum_a \frac{c_{\alpha a} u_a}{c_s^2} + \sum_{a,b} \frac{\Pi_{\alpha ab} u_a u_b}{2 c_s^4} \right) \tag{2.27}$$

in which $\Pi_{\alpha ab} = c_{\alpha a} c_{\alpha b} - c_s^2 \delta_{ab}$; $w_\alpha$ represents the set of weights associated to each direction: in a $D_2Q_9$ scheme, for example, direcctions from 1 to 4 (Fig. 2.2 have the same weight, which is 1/9, while directions from 5 to 8 have $w_\alpha = 1/36$ and finally direction 0 has a weight equal to 4/9

# Chapter 3

# Multiphase Methods for LBM

The numerical methods based on the traditional continuum approach (i.e. Navier-Stokes with closure relationships) usually rely upon rather complex correlations and often require transient solution algorithms with very small time steps. Since its early days, the Lattice Boltzmann shed promises of becoming a tool for the modeling of multiphase flows. The continuum approach, in fact, may become inadequate to describe complex flow phenomena (i.e. droplet formation, break-up, cavitation and colaescence, water waves and free-surface flows) associated to the contemporary presence of different phases. Such diculties are often signalled by a singular behaviour of the continuum equations (i.e. tip rupture), [21]. The kinetic approach is in principle better suited to handle the complex phenomena related to multiphase flows, since it can incorporate (minimal) aspects of microscopic physics (i.e. interphase interactions) without surrendering the computational effciency of continuum methods. With concern to the

latter point, it is worth noting that a still widespread misbelief is that LBE should apply only to dilute gases, the reason being that it derives from an approximation of the continuum Boltzmann equation, which was originally derived under the assumption of dilutedness. This line of thinking fails to recognize that, although kinetic theory was originally meant to describe weakly interacting (dilute) systems, it can also be applied whenever strong interactions between elementary degrees of freedom can be cast in the form of weak interactions between appropriate collective degrees of freedom (quasiparticles). LB falls within this category, since each LB population is hydrodynamically representative of a large collection of real molecules. Another source of confusion is to assume that, since BGK is a model approximation to the true Boltzmann equation, it should inherit all of its limitations. This is not necessarily the case, because BGK is based on two fairly universal assumptions, namely:

1. There exist a local attractor to the collisional dynamics (local equilibrium)

2. In the vicinity of this local equilibrium, the collisional dynamics can be described in terms of a simple relaxation process, the relaxation time-scale mixing the viscosity of the fluid.

Assumption 1 is certainly true for any statistical-dynamics system supporting microscopic invariants, while assumption 2 is also fairly plausible for generic systems with short-range interactions. For sure, neither of the two is restricted to dilute gases.

The earliest Lattice Boltzmann simulations of multi-component flows have been performed by Gunstensen et al. [22, 23] and Grunau et al. [7], based on the pioneering Rothman-Keller lattice gas multiphase model [24]. Ever since, many models have been proposed in

the past in order to simulate multiphase flows with the LBM, most of them aiming at incorporating the physics of phase-segregation and interface dynamics, typically hard to model with traditional methods, through simple mesoscopic interaction laws.To date, there are several methods to incorporate the physics of complex non-ideal fluids at the kinetic (Lattice Boltzmann) levels. In this thesis, we shall focus on the following three classes, restricting our attention to single-component multi-phase flows only:

1. Pseudo-Potential (PP);
2. Free-Energy (FE);
3. Front-Tracking (FT).

In particular, the pseudo-potential LBM, due to Shan and Chen [25], has gained increasing popularity on account of its conceptual simplicity and computational efficiency. In the Shan-Chen (SC) method, potential energy interactions are represented through a density dependent, mean-field, pseudo-potential and phase separation is achieved by imposing a short-range attraction between the light and dense phases. This method allows to track and maintain diffuse interfaces with no need of any special treatment of the interface. However, it is known to present unphysical features (i.e spurious velocities), namely the presence of non-zero velocities even for fluids at rest, with a steady density profile. These spurious currents are disturbing for practical applications, and they may cast doubts on the quantitative accuracy of the simulations methods [26]. The spurious currents have been recently addressed by many authors [27, 28, 29]. He et al. [29] proposed a multi-phase LBM scheme with improved numerical stability. It still

incorporates molecular interactions, but unphysical features are alleviated by introducing a pressure distribution function instead of the single-particle density distribution function. A particularly remarkable option has been suggested by Lee et al. [27, 28, 30, 31], who proposed a higher order finite difference treatment of the kinetic forces arising from non-ideal interactions (potential energy). In this model, spurious currents are allegedly tamed by a judicious resort to higher-order finite difference treatment of the non-ideal interactions.

Both PP and FE methods belong to the general class of diffuse-interface ($DI$) methods, whereby the interface between the two phases is not tracked explicitly, but rather defined by the transition region of a given scalar function, typically the fluid density or an equivalent scalar. By definition, this implies that the interface extends over a number of grid sites, whence the denomination *diffuse-interface*. The FT method belongs instead to the so-called class of front-tracking (FT) methods, whereby the interface is explicitly tracked within the grid. In these methods, the interface is basically a zero-thickness mathematical surface, hosting a discontinuous jump of the uid density across the light and dense phases, say vapor and liquid. Since no eort is spent in describing the internal structure of the front, it is clear that front-tracking methods are most naturally addressed to large-scale flows, whereas diffuse-interface methods can, in principle, account for the physics of the phase-transition across the interface, so that they are most naturaly targeted to smaller scales. Conceptually, DI and FT methods fall withing the general rubric of Eulerian versus Lagrangian methods, respectively. From the computational standpoint, diffuse-interface methods are simpler, because they do not require any front tracking and reconstruction within the grid, but are exposed to the

usual weaknesses of Eulerian methods, high-resolution to tame excessive numerical diffusivity. Lagrangian methods on the other hand, are more exposed to numerical instabilities generated by geometrical complexities of the moving interface. Consistently with the mesoscopic nature of kinetic theory, to date LB methods have been used almost exclusively in their DI versions. However, recent work, including the one presented here, is starting to appear also in the FT camp. That is basically the motivation for the "across" in the title of the present paper. This paper presents selected applications, directly drawn from the authors first-hand experience, of the three aforementioned LBM approaches to multiphase flows, covering a broad range of spatial scales. No attempt is made to couple these methods across scales, but special attention is paid instead to a qualitative identi

cation of the parametric regimes in which each of these models is possibly best applied.

## 3.1 Interphase interactions

The LB Method allows to account for the interactions between different phases in non-ideal fluids, by means of a generalized force term in eq. 3.1:

$$\frac{\vec{F}}{m} \cdot \frac{\partial f}{\partial \vec{v}} \tag{3.1}$$

in which the generalized force accounts for *both* external fields (such as gravity or electro-magnetic fields) and *self-consistent* interaction forces associated with intermolecular interactions or any other effective interaction we wish to include. The corresponding generalized LBGK

equation reads as follows:

$$\Delta_\alpha f_\alpha = -\frac{1}{\tau}(f_\alpha - f_\alpha^{eq}) + S_\alpha \tag{3.2}$$

where $S_\alpha$ is a source term that can be formally interpreted as the discrete velocity representation of 3.1. Operationally, $S_\alpha$ can be a source of mass, momentum, energy, or any other macroscopic observable in the form

$$\Phi(\boldsymbol{x}, t) = \sum_\alpha \phi(\boldsymbol{c}_\alpha, \boldsymbol{x})\ f_\alpha(\boldsymbol{x}, t) \tag{3.3}$$

in which $\phi(\boldsymbol{c}_\alpha, \boldsymbol{x})$ is a generic phase-space dependent microscopic quantity. The different formulation of the term $S_\alpha$ gives rise to the different multiphase approaches in the Lattice Boltzmann universe.
In the following paragraphs some multiphase models will be presented, however, in the current study, the Lee model [27, 28, 30, 31] characeristic of free-energy approaches will be used.

## 3.2 The Pseudo Potential Approach

We consider the standard lattice Boltzmann (LB) equation with pseudopotentials

$$f_\alpha(\boldsymbol{x} + \vec{c}_\alpha, t + 1) - f_\alpha(\boldsymbol{x}, t) = -\omega(f_\alpha - f_\alpha^{eq}) + F_\alpha \tag{3.4}$$

The term $F_\alpha$ is the pseudo-force, which expression is given below

$$\boldsymbol{F}(\boldsymbol{x}, t) = -G_0 \psi(\boldsymbol{x}, t) \sum_\alpha^{N_{pop}} \psi(\boldsymbol{x} + \boldsymbol{c}_\alpha \Delta t, t)\, \boldsymbol{c}_\alpha w_\alpha \tag{3.5}$$

where $N_{pop}$ is the number of possible directions in every lattice site (9 in this approach) and $\psi(\boldsymbol{x}, t)$ is a local functional of a density:

$$\psi(\boldsymbol{x}, t) = \rho_0 \left[1 - \exp\left(-\frac{\rho(\boldsymbol{x}, t)}{\rho_0}\right)\right] \tag{3.6}$$

In this application the reference density $\rho_0$ is set to $\rho_0 = 1$ and $G_0$ is the basic parameter which rules the inter-particle interaction. In this model, $G_0$ is the only free parameter fixing both density ratio and the surface tension of the model. The possibility of modifying these values is limited to a short range of values near the equilibrium ones.
Starting from Equation (3.5) the component of the interaction potential along each direction can be evaluated. This force is used for shifting the velocities prior to evaluating of the equilibrium distribution functions, according to:

$$\boldsymbol{u}'(\boldsymbol{x}, t) = \boldsymbol{u}(\boldsymbol{x}, t) + \frac{\boldsymbol{F}(\boldsymbol{x}, t)\,\tau}{\rho(\boldsymbol{x}, t)} \tag{3.7}$$

The Equation of State of the system is influenced by this contribution, and takes form:

$$P = p_0 + \frac{c_s^2 G_0}{2}\psi^2 = \rho c_s^2 + \frac{c_s^2 G_0}{2}\psi^2 \tag{3.8}$$

The greatest limits in the Shan-Chen approach are mainly related to the reduced magnitude of possibile density ratioes: usually, in fact, $\rho_L/\rho_V \leq 10$. There are two other concerns of thermodynamic nature. The first regards the formulation of $\psi(\rho)$: the natural choice of $\psi(\rho)$ would be $\psi(\rho) = \rho$, since the lattice spacing is usually much larger than the molecular size (a condition necessary for ensemble averages). However, this choice completely ignores the effects of the repulsive core

(the *Lennard-Jones* hard- and soft-core interaction, [16]). Without a balancing repulsive core, this choice inevitably leads to "mass collapse" with particle density approaching infinity. The formulation of $\psi(\rho)$ leads also to the second thermodynamic *caveat* in the computation of surface tension. In the Shan-Chen approach, surface tension is computed as follows,

$$\sigma = \frac{G\ R\ T}{2} \int_{-\infty}^{\infty} |\nabla\psi|^2 dz \tag{3.9}$$

that would be thermodinamically consistent only if $\psi(\rho) \propto \rho$, instead of $\psi(\rho) \propto e^{-\rho/\rho_0}$. Modern variants [32, 33, 34] considerably extend the scope of the SC model. As decribed in [33], it is possible to consider generalized pseudoforces of the following form

$$\boldsymbol{F}(\boldsymbol{x},t) = \sum_{j=1}^{2} c_s^2 G_j \psi_j^{n(j)}(\rho(\boldsymbol{x},t)) \sum_{\alpha=1}^{b_j} p_{\alpha j} \boldsymbol{c}_{\alpha j} \psi_j^{n(j)}(\rho(\boldsymbol{x}+\boldsymbol{c}_{\alpha j},t)) \tag{3.10}$$

In the above, the index $j$ labels the Seitz-Wigner cell (*belt* for simplicity) defined by the condition $|\boldsymbol{x'}-\boldsymbol{x}|^2 \leq 2j^2$, whereas $\boldsymbol{c_{\alpha j}}$ denotes the set of discrete speeds belonging to the $j-th$ belt. The exponents $n(j)$ are chosen to be: $n(1) = 1$ and $n(2)$ varying between 1 and 1/8, [33]. Note that lattice units $\Delta x = \Delta t = 1$ have been assumed here. In this work we shall confine our attention to the 24-neighbors, 2-belt lattice depicted in Figure 3.2.

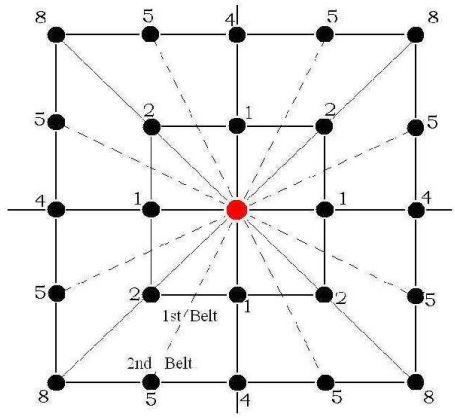


Figure 3.1: Two-belt lattice for force evaluation. Each node is labelled by the corresponding energy $|c_{ij}|^2$. Belt 1 contains eight speeds and two energy levels $(1, 2)$. Belt 2 contains sixteen speeds, distributed over three energy levels $(4, 5, 8)$

As is well-known, the standard 1-belt, 8-speed lattice provides 4th-order isotropy, whereas the 2-belts, 24-speed lattice upgrades isotropy to 8th order, provided the weights are properly chosen. A suitable choice is reported in [33].
To forestall any confusion, we wish emphasize that the 2-belt lattice is used *only* for the (pseudo)-force evaluation, whereas tha standard lattice Boltzmann dynamics still takes place in the original D2Q9 lattice. This is also the reason why we keep a separate notation for the weights $w_\alpha$ used for the lattice Boltzmann populations and the weights $p_{\alpha j}$ used for the force evaluation. In the case mostly used of $n(2) = 1$, from equation (3.10) it is possible to find the equation of state of our

system, which reads:

$$p(\rho) = \rho c_s^2 + \frac{1}{2} G_1 C_1 \psi^2 + \frac{1}{2} G_2 C_2 \psi^2 \tag{3.11}$$

This can be recast as follows:

$$p(\rho) = \rho c_s^2 + \frac{1}{2} G_{eff} \psi^2 \tag{3.12}$$

where

$$G_{eff} = G_1 C_1 / c_s^2 + G_2 C_2 / c_s^2 \tag{3.13}$$

is an effective coupling and

$$\begin{aligned} c_s^2 &= \sum_{\alpha=0}^{8} w_\alpha c_{\alpha 1,x}^2 = 1/3 \\ C_1 &= \sum_{\alpha=1}^{8} p_{\alpha 1} c_{\alpha 1,x}^2 = 737/3000 \\ C_2 &= \sum_{\alpha=1}^{16} p_{\alpha 2} c_{\alpha 2,x}^2 = 33/375 \end{aligned} \tag{3.14}$$

At the level of the EOS, this is the same as the Shan-Chen model, just with a rescaled coupling. However, since repulsive forces act on the second belt of neighbors, they are distributed differently in space, and consequently their effect cannot be captured by a mere rescaling of the attractive interactions, possibly allowing density ratios to depend on $G_1$ and $G_2$ separately. From a qualitative point of view, this can be seen through a Taylor development of the coupling force. Indeed, the force given by the equation (3.10) can be written in the continuum as:

$$\boldsymbol{F}(\boldsymbol{x}, t) = G_{eff} \boldsymbol{\nabla} \psi + g(G_1, G_2) c_s^2 \boldsymbol{\nabla} \nabla^2 \psi + O(\nabla^4) \tag{3.15}$$

where $g(G_1, G_2) = \sum_{\alpha=1}^{8} p_{\alpha 1} c_{\alpha x}^4 + \sum_{\alpha=1}^{16} p_{\alpha 2} c_{\alpha x}^4$. This expression differs from standard Shan-Chen, since in standard Shan-Chen both coefficients would be $G_{eff}$.

The two-parameter equation of state (3.11) offers an additional degree of freedom, $G_2$, as compared with the standard Shan-Chen. As recently shown [32], this degree of freedom can be used to tune the surface tension independently of the equation of state. With the $2 - belt$ approach, the zones of attraction-repulsion (AR) and of repulsion-attraction (RA) potential can be considered, even if the (RA) region corresponding to positive $G_1$ and negative $G_2$, may seem the most physical, since the hard-core repulsion could be associated to the first belt and the soft-core attraction with the successive belt.

The extension to the second belt of the interphase interaction allows several enhancements as compared to the standard Shan-Chen approach. The density ratio, in fact, can rise up to $1 : 250$, only limited by the magnitude of parasitic currents which, with high density ratioes, can grow up to $u_{spurious} \sim 0.3$. The presence of two control parameters, namely $G_1$ and $G_2$ permits to control the surface tension magnitude for a given density ratio, which is not possible in the standard Shan-Chen approach, giving more consistency to the multiphase simulation, [35]. Moreover, the $2 - belt$ approach gives the possibility to reduce consistently the magnitude of spurious currents up to a factor $\sim 0.8$, [36].

## 3.3 Pseudo Potential and Free Energy limits

The free energy approach will be deeply analyzed in the following chapter. Nevertheless it is useful to introduce in this section a main comparison between PP and FE approaches.
The LBM multiphase models based on interparticle interactions (i.e. phase transitions) present some limits, that could be expressed in terms of dimensionless parameters, which measure the relative strength of the various competing mechanisms. Among others, the most important ones are the Weber number, $We = \frac{\rho U^2 D}{\sigma}$, measuring the competion between inertia and surface tension, the Reynolds number, $Re = \frac{UD}{\nu}$, measuring the ratio of inertia and dissipation, and the Eotvos number $Eo = \frac{a\delta\rho D^2}{\sigma}$ and the Froude number $Fr = \frac{U}{\sqrt{a\ D}}$, expressing the relative strength of external drive (e.g. gravity) versus surface tension and inertia effects, respectively. In the above $\rho$ is the liquid density, $U$ the typical speed, $D$ the typical droplet diameter, $\sigma$ the surface tension, $\nu$ the liquid kinematic viscosity, $a$ the acceleration due to external fields. In practical applications involving the motion of small liquid droplets moving across a continuum gaseous phase, the Weber and Reynolds numbers can reach up to several thousands. It is therefore of interest to provide a semi-quantitative assessment of the capability of the present methods to reach up these parametric regimes. To this purpose, we remind the main limitations inherent to the LB models:

- $U_{LB} < 0.1$ (finite-compressibility constraint);
- $\nu_{FE} \sim 0.01$ (dissipative stability constraint);

- $\nu_{PP} = 1/6$ (numerical stability constraint);
- $\sigma_{FE} < 0.001$ (surface tension stability constraint);
- $\sigma_{PP} = 10^{-2} \div 10^{-1}$ (Equation Of-State constraint);

The first constraint stems from the fact that LB is a weakly compressible scheme, and if the local flow speed gets in the proximity of the sound speed $c_s$, the LB local equilibria may become negative, thereby ruining the stability of the scheme. The constraint on $\nu$ in the $FE$ approach is related to the fact that if the viscosity becomes too low, typically 0.01 in lattice units, local gradients of the flow field can develop, which may undermine the very basis of the hydrodynamic limit, namely a weak departure from local equilibria (the above constraint does *not* apply to the so-called entropic version of LB methods, [16]). On the other side, in the $PP$ methods, the kinematic viscosity is numerically fixed to 1/6 for computational stability.
The above constraints are well known from the single phase LB literature [33].
The constraint on $\sigma$ is inherent to the different formulations for non-ideal fluids. The EOS in the Shan-Chen approach fixes the surface tensionn magnitude to the density ratio, while in the $2-belt$ schematization, a certain degree of freedom in surface tension magnitude is allowed (see, for example, Tab. 3.1). For what concerns the FE method, our direct numerical experience shows that it is very hard to bring the surface tension above $\sigma_{LB} \sim 10^{-3}$ without experiencing numerical instabilities. It is of interest to observe that this value is about ten times smaller than the typical surface tensions with the (standard) Shan-Chen model, [37].
Thus, starting from the above constraints, a resolution of $1000 \times 1000$

grid points, permits to explore approximately the following range:

$$Re_{PP} = \frac{U_{LB} D_{LB}}{\nu_{PP}} < 100, \qquad Re_{FE} = \frac{U_{LB} D_{LB}}{\nu_{FE}} \leq 1000 \quad (3.16)$$

$$We_{PP} = \frac{\rho_{PP} U_{LB}^2 D_{LB}}{\sigma_{FE}} < 100, \quad We_{FE} = \frac{\rho_{FE} U_{LB}^2 D_{LB}}{\sigma_{FE}} \leq 1000 \quad (3.17)$$

$$Eo_{PP} = \frac{a_{LB} D_{LB}^2 \Delta\rho_{PP}}{\sigma_{PP}} < 10, \quad Eo_{FE} = \frac{a_{LB} D_{LB}^2 \Delta\rho_{FE}}{\sigma_{FE}} \leq 100 \quad (3.18)$$

$$Fr_{PP} = \frac{U_{LB}}{\sqrt{g_{LB}\ D_{LB}}} \leq 10, \qquad Fr_{FE} = \frac{U_{LB}}{\sqrt{g_{LB}\ D_{LB}}} \leq 10 \quad (3.19)$$

which gives a reasonable set of values for a large number of applications.

## 3.4 The Front Tracking Approach

As shown in the previous section, the $Pseudo - Potential$ and the $Free - Energy$ approaches present limits in simulating large-scale phenomena. For what concerns the $FE$ method, eqs. 3.17 and 3.18 highlight restrictive limits in terms of Reynolds and Weber numbers to avoid numerical instabilities. In the $PP$ approaches, however, $Re$ and $We$ numbers are limited as well by the choice of the grid spacing, in order to avoid unaffordable computational efforts.
In such a frame, the possibility of *by-passing* the limits of these two methods is given by the $Front - Traking$ approach. The model uses a

simplified approach for the study of the interface between two immiscible fluids, based on the same philosophy of the VOF (Volume of Fluid) technique. The main difference, which also represents the main advantage of the LBM front-tracking approach, is that the single-species transport equation, used in Navier-Stokes/VOF model to determine the relative volume fraction of the two phases, or phase fraction, in each computational cell, is not needed, as the free-surface tracking is automatically performed, as described in the following.

In the LBM front-tracking model, a single set of LB equations is solved for the heavy fluid, from now on referred to as *liquid*, while the light fluid (i.e. *gas*) is neglected in the simulation. The liquid volume fraction is introduced as an additional variable:[

$$\begin{aligned} &\varepsilon(x) = 0, \forall x \in G \\ &\varepsilon(x) = 1, \forall x \in L \\ &0 < \varepsilon(x) < 1, \forall x \in I \end{aligned} \tag{3.20}$$

in which $G$ represents the gas cells (i.e. empty cells), $L$ the liquid cells and $I$ the $interface$ ones.

The domain is then composed of liquid, gas and interface cells. The latter contain both liquid and gas and form the closed layer between liquid and gas cells that has to be tracked throughout the computational domain as the *free-surface*. Only a single layer of interface cells around the fluid cells is used.
The computation is then subdivided into the following three steps [38, 39]:

1. interface movement;

2. boundary conditions at the interface between gas and liquid;

3. cell types update;

### 3.4.1 Interface Movement

The movement of the fluid interfaced is retreived by means of the mass contained in the cell, by taking into account both the mass $m$ and the fluid fraction $\varepsilon$ of the cell as follows:

$$m(\boldsymbol{x}, t) = \varepsilon(\boldsymbol{x}, t)\ \rho(\boldsymbol{x}, t) \tag{3.21}$$

The interface motion is computed from the flux between the cells: the evolution of mass can be followed considering the values streamed between two adjacent cells for all the lattice directions. For an interface cell, this reads as follows,

$$\Delta m(\boldsymbol{x}, t + \Delta t) = f_\alpha^{in}(\boldsymbol{x} + \boldsymbol{c}_\alpha \Delta t, t) - f_\alpha^{out}(\boldsymbol{x}, t) \tag{3.22}$$

in which $f_\alpha^{in}$ represents the amount of liquid *entering* the cell and $f_\alpha^{out}$ the amount of liquid *leaving* the cell. The mass exchange between two interface cells must be directly related to the actual mass content of each cell: thus, eq. 3.22 becomes

$$\Delta m(\boldsymbol{x}, t+\Delta t) = \left(f_\alpha^{in}(\boldsymbol{x} + \boldsymbol{c}_\alpha \Delta t, t) - f_\alpha^{out}(\boldsymbol{x}, t)\right) \frac{\varepsilon(\boldsymbol{x} + \boldsymbol{c}_\alpha \Delta t, t) + \varepsilon(\boldsymbol{x}, t)}{2} \tag{3.23}$$

From eqs. 3.22 and 3.23 we see that the amount of fluid leaving the cell is the very same that enters the cell, for the sake of continuity. It is important to notice that direct state changes from liquid to gas and vice versa are not possible. Hence, liquid and gas cells are only allowed to transform into interface cells whereas interface cells can be transformed into both gas and liquid cells. Finally, in the interfacial cells, mass and density are completely decoupled, thus the mass evolution does not affect the particle distribution functions.

### 3.4.2 Free Surface Boundary Conditions

The empty cells are never accessed during computation. Thus, during the streaming process, only the particle distribution functions coming from liquid or interface cells can be computed normally, while those coming from the gas phase must be reconstructed from the boundary conditions at the liquid interphase. The following two important assumptions have to be made:

- the viscosity of the fluid is significantly lower than that of the gas phase;
- gas pressure (i.e. atmospheric pressure) is constant.

This corresponds to the assumption that the interface moves the same way the liquid does.
At the boundary between the phases (i.e. interphase), the velocity of both is set to be the same and the force performed by the gas is balanced by the one performed by the liquid. The reconstructuring procedure [38] provides the missing populations: for an interface cell at site $(\boldsymbol{x})$ with an empty cell at $(\boldsymbol{x} + \boldsymbol{c}_\alpha\ \Delta t)$, the post-streaming density function $\tilde{f}_i$ is given by

$$\tilde{f}_\alpha(\boldsymbol{x}, t + \Delta t) = f_\alpha^{eq,in}(\rho_{gas}, \boldsymbol{u}) + f_\alpha^{eq,out}(\rho_{gas}, \boldsymbol{u}) - f_\alpha^{out}(\boldsymbol{x}, t) \quad (3.24)$$

where $\boldsymbol{u}$ is the fluid velocity at the interface cell. In eq. 3.24, the effects of surface tension are neglected, but may be included in the two equilibrium distribution functions [39].

### 3.4.3 Cell-Type Updating

The collision step follows the same rules as in the *traditional* Lattice Boltzmann methods. Once the streaming and collision steps are

completed, the cell type at the interface must be checked: the conversion between gas and liquid must be accoplished by accessing to neighbour cells. The following two aspects must be verified:

- the layer of the new interface must be closed again to separate the two phases;
- mass must be conserved during the conversion.

The density, calculated after the collision, is used to check wether the interface cell filled or emptied during the time step:

$$m(\boldsymbol{x}, t + \Delta t) > (1 + \kappa)\ \rho(\boldsymbol{x}, t + \Delta t) \rightarrow cell\ filled \tag{3.25}$$

$$m(\boldsymbol{x}, t + \Delta t) < (0 - \kappa)\ \rho(\boldsymbol{x}, t + \Delta t) \rightarrow cell\ emptied \tag{3.26}$$

in which $\kappa$ is an offset, usually $\kappa = 10^{-3}$.
In order to assure mass conservation, the excess mass is equally redistributed in the neighbouring cell. Then, the neighborhood of all filled cells is computed; the neighboring empty cells are turned into interface and initialized with the equilibrium distribution functions, computed with average density and velocity.

## 3.5 Models range of application

It is interesting, from an appliction-oriented point of view, to compare the capabilities of the above methods for the simulation of a technical problem. The *Front-Tracking* approach is better oriented towards the simulation of *macro-scopic* phenomena, in which the actions due to the *inertia* of the fluid are predominant as compared to the other interactions. A typical field of application is that of the

*free-surface* phenomena, like tsunami's, flood waves or tidal waves, characterized by $Re$ numbers higher than $10^4$.

The *Pseudo-Potential* and the *Free-Energy* methods, on the other hand, are suited for phenomena from a *micro-* to a *meso-scale*. To expalain this, a free-jet simulation can be considered: Table 3.1 presents the main dimensionless parameters related to such a case. The inlet velocity is set to 200 $m/s$, that is 0.1 expressed in lattice units and the characteristic length is the nozzle diameter of 0.1 $mm$, fixed to 200 lattice points for the different cases.

| | $SC$ | $2belts$ | $FE$ |
|---|---|---|---|
| $\rho_L$ | 2.5 | 2.5 | 1 |
| $\rho_V$ | 0.083 | 0.083 | 0.033 |
| $\sigma$ | 0.1130 | $0.1009 - 0.1662$ | $1 \cdot 10^{-4}$ |
| $Re_L$ | 120 | 120 | 1200 |
| $We_L$ | 44.2 | $49.55 - 30.0$ | $2 \cdot 10^4$ |
| *spurious currents* | 0.025 | $0.045 - 0.004$ | $10^{-14}$ |

Table 3.1: Dimensionelss parameters for a diesel injection simulation; $u_{in} = 0.1$ corresponding to $\sim 200$ $m/s$; densities and surface tension are expressed in *lattice units*.

The $Re_L$ and $We_L$ numbers in Tab. 3.1 can be increased only by decreasing the lattice space, that is increasing the number of nodes inside the domain and, thus, demanding greater computational efforts.

The boundary between the application fields of these two methods can be identified according to the magnitudes of the dimensionless numbers in Tab. 3.1.

The Free-Energy approach allows to reach higher dimensionless numbers, due to its numerical stability in dealing with low viscosities ($O(10^{-2})$ in lattice units) and *very* low surface tensions ($O(10^{-4})$ in lattice units).
The Pseudo-Potential approaches, on the other side, see their viscosity numerically fixed to a precise value ($O(10^{-1})$ in lattice units) and the surface tensions ranging in an interval of $O(10^{-2}) \div O(10^{-1})$ lattice units, thus being much more oriented than the Free-Energy approach towards micro-flow simulations, in which the surface tension interactions are predominant.

The main problem of the Psudo-Potential methods is related to the presence of the spurious currents, that, however, can be decreased in the $2 - belt$ model of a factor up to $\sim 0.8$ [36], while in the Free-Energy approach the lack of some types of boundary conditions at the moment dramatically reduces its applicability to technical problems.

Table 3.2 proposes a possible way to distinguish the different fileds of application of the different methods, as referred to the order of magnitude of the main dimensionless parameters characterising the *real* phenomena (that is, not referring to lattice units, but to the physical ones). It is worth of noting that a $We$ range has been indicated also for the front tracking approach, mainly suitable for large scale hydraulics, characterised by high $Re$ and low $Fr$, not reachable by the SC and Free-energy models. In fact, in the application shown in the front-trackig section, the surface tension is neglected. However, the front-tracking method may be also applied to those flow problems, such as free-jet or droplet flows, in which surface tension plays a significant role at the interface, by including the Young-Laplace equation

(i.e. surface tension, local interface curvature and liquid- and gas-side pressure effects) as an external force term in equation 3.24, as reported in [39]. Therefore, the front-tracking method with this numerical artifact may be used in surface-tension driven flows, where the phase transition approach (i.e. SC and free-energy) are not applicable or require very high computational effort (i.e. high $We$ and $Re$).

| | $\frac{\rho_L}{\rho_V}$ | $Re_L$ | $We_L$ | $Fr$ | *applications* |
|---|---|---|---|---|---|
| $FT$ | $-$ | $> 10^4$ | $> 10^6$ | $< 10^1$ | large-scale hydraulics<br>high-speed sprays |
| $FE$ | $10^3$ | $< 10^4$ | $> 10^3$ | $> 10^2$ | free jets<br>cavitation |
| $2belts$ | $10^2$ | $< 10^3$ | $< 10^3$ | $> 10^0$ | wall impingement<br>low-speed jets<br>micro-flows |
| $SC$ | $10^1$ | $< 10^2$ | $< 10^2$ | $> 10^0$ | ferrofluids<br>capillarity effects |

Table 3.2: Application fields of the different methods as functions of the dimensionless numbers *Reynolds*, $Weber$ and $Froude$, that characterise the *real-scale* phenomena.

# Chapter 4

# The Free Energy Approach

In this chapter the model presented by Lee et al. [27, 28, 30, 31], who proposed a higher order finite difference treatment of the kinetic forces, will be deeply analyzed. As already pointed out, in this model, spurious currents are allegedly tamed by a judicious resort to higher-order finite difference treatment of the non-ideal interactions, but this advantage is not free and it will be paid in terms of complexity and implementation.

In the following chapter a brief description of the algorithm and of derivatives discretization will be carried out for the Lee model [27, 28, 30, 31, 37]. The standard procedure for Lattice Boltzmann Method is used as well but the presented model requires some additional features lie to the forcing terms. The formulation of these added terms is sometimes tricky and influences the general procedure used for the solution of multiphase flows problems.
In the final part of the chapter a description of paralelization procedure, carried out both for 2D and 3D models, will be reported. Due

to the always increasing computational resources required in order to properly simulate this kind of problem, one of the steps we have developed has been the code paralelization.

## 4.1 Model Definition

The model introduced in [28] starts with a Cahn-Hilliard formulation for the *i-th* species the continuity equation of multicomponent fluid, that can be written as:

$$\frac{\partial \tilde{\rho}_i}{\partial t} + \nabla \cdot \tilde{\rho}_i \mathbf{u}_i = 0 \tag{4.1}$$

where $\tilde{\rho}_i$ and $\mathbf{u}_i$ represent the local density and the velocity of the i-th species. The total density can be easily recast as $\rho = \sum_i \tilde{\rho}_i$ and it is also conserved. The local velosity is in such a way function of averaged volume velocity $\mathbf{u}$ and of the product between the bulk density $\rho_i$ and the diffusive flow rate $\mathbf{j}_i$ as expressed in the following equation:

$$\rho_i \mathbf{j}_i = \tilde{\rho}_i \left( \mathbf{u}_i - \mathbf{u} \right) \tag{4.2}$$

The previous equations 4.1, 4.2 can be rewritten for a binary system (where $i = 1, 2$) and expressed in terms of composition $C \equiv \frac{\tilde{\rho}_1}{\rho_1}$:

$$\frac{\partial C}{\partial t} + \nabla \cdot (\mathbf{u} C) = -\nabla \cdot \mathbf{j}_1 \tag{4.3}$$

Naming $\rho_1$ and $\rho_2$ respectively density for the two components the mean density can be expressed as $\rho = C\rho_1 + (1 - C)\rho_2$. Usually the diffusive flow rate is related to the local composition of two components, thus $\mathbf{j}_1 = -\mathbf{j}_2 = \mathbf{j}$ which leads to:

$$\nabla \cdot \mathbf{u} = 0 \tag{4.4}$$

In terms of the composition $C$, the mixing energy density for an isothermal system reads as:

$$E_{mix}\left(C, \nabla C\right) = E_0\left(C\right) + \frac{\kappa}{2}\left|\nabla C\right|^2 \tag{4.5}$$

where $C$ is the composition of one component and $\kappa$ is the gradient parameter. The bulk energy can be rewritten as:

$$E_0\left(C\right) \approx \beta C^2\left(C-1\right)^2 \tag{4.6}$$

where $\beta$ is a constant fixing the free-energy barrier between the pure states $C = 0$ and $C = 1$. The chemical potential can be expressed as the derivative ov $E_0$ with respect to $C$:

$$\mu_0 = \frac{\partial E_0}{\partial C} = 2\beta C\left(C-1\right)\left(2C-1\right) \tag{4.7}$$

The real interaction chemichal potential takes into account the contribution of interface curvature which is transported through the laplacian of concetration:

$$\mu = \mu_0 - \kappa\nabla^2 C \tag{4.8}$$

where $\kappa$ is a function of $\beta$ and of the interface thickness $D$, which represent the free parameters of the model:

$$\sigma = \frac{\sqrt{2\kappa\beta}}{6} \qquad D = \sqrt{\frac{8\kappa}{\beta}} \tag{4.9}$$

In the Chan-Hilliard model, the diffusive flow rate is assumed to be proportional to a thermodinamic force, function of chemical potential gradient:

$$\mathbf{j} = -M\nabla\mu \tag{4.10}$$

where $M > 0$ is the mobility factor. Thus the conservation equation for concentration can be expressed as:

$$\frac{\partial C}{\partial t} + \mathbf{u} \cdot \nabla C = \nabla \cdot (M \nabla \mu) \tag{4.11}$$

The non-ideal bulk pressure, through the Legendre's relation, can be written in terms of bulk energy and chemichal potential:

$$p_0 = C \frac{\partial E_0}{\partial C} - E_0 = C\mu_0 - E_0 \tag{4.12}$$

The external force representing the non-ideal gas effects can be expressed as (pressure form):

$$\mathbf{F} = \nabla \rho c_s^2 - \nabla p_0 + \rho \kappa \nabla \nabla^2 \rho \tag{4.13}$$

where can be highlighted the term proportional to the surface tension $\rho \kappa \nabla \nabla^2 \rho$. In order to enforce incompressibility [28], the forcing term can be re-written by including the hydrodynamic pressure:

$$\mathbf{F} = \nabla \rho c_s^2 - \nabla p_1 - C \nabla \mu \left( C \right) \tag{4.14}$$

The total pressure in the momentum equation can be obtained by summing to the hydrodynamic pressure $p_1$, defined later in Eqn. (4.30), the thermodynamic pressure $p_0$ and the curvature term as follows:

$$P = p_0 + p_1 - \kappa C \nabla^2 C + \frac{1}{2} \kappa \left| \nabla C \right|^2 \tag{4.15}$$

The Lee model evolves the *pressure* instead of the density, and consequently, the discrete distribution is defined as follows:

$$g_\alpha = f_\alpha c_s^2 + \left( p_1 - \rho c_s^2 \right) \Gamma_\alpha \left( 0 \right) \tag{4.16}$$

where $f_\alpha$ is the usual discrete particle distribution, as defined in the classic LBE theory, and $\Gamma_\alpha(\mathbf{u}) = f_\alpha^{eq}/\rho$ (as a consequence $\Gamma_\alpha(0) \equiv w_\alpha$), and $\alpha$ runs over the set of discrete speeds. In this case the model is written for a two dimensional, nine velocities (D2Q9) LBE. The total derivative, $D_t = \partial_t + \mathbf{c}_\alpha \cdot \nabla$, of this variable reads as follows:

$$\begin{aligned}\frac{\partial g_\alpha}{\partial t} + \mathbf{c}_\alpha \cdot \nabla g_\alpha = &- \frac{1}{\tau}\left(g_\alpha - g_\alpha^{eq}\right) \\ &+ \left(\mathbf{c}_\alpha - \mathbf{u}\right) \cdot \left[\nabla \rho c_s^2 \left(\Gamma_\alpha - \Gamma_\alpha(0)\right) - C\nabla\mu\Gamma_\alpha\right]\end{aligned} \tag{4.17}$$

with the following expression for the equilibrium distribution:

$$g_\alpha^{eq} = w_\alpha \left[p_1 + \rho c_s^2 \left(\frac{\mathbf{c}_\alpha \cdot \mathbf{u}}{c_s^2} + \frac{\left(\mathbf{c}_\alpha \cdot \mathbf{u}\right)^2}{2c_s^4} - \frac{\left(\mathbf{u} \cdot \mathbf{u}\right)}{2c_s^2}\right)\right] \tag{4.18}$$

The above presented equation 4.17 can be integrated in time and space obtaining the following DBE:

$$\begin{aligned}&g_\alpha\left(\mathbf{x} + \mathbf{c}_\alpha\delta t, t + \delta t\right) - g_\alpha\left(\mathbf{x}, t\right) = \\ &- \left.\frac{g_\alpha - g_\alpha^{eq}}{2\tau}\right|_{(\mathbf{x},t)} - \left.\frac{g_\alpha - g_\alpha^{eq}}{2\tau}\right|_{(\mathbf{x}+\mathbf{c}_\alpha\delta t, t+\delta t)} \\ &+ \frac{\delta t}{2}\left(\mathbf{c}_\alpha - \mathbf{u}\right) \cdot \left[\nabla^B \rho c_s^2 \left(\Gamma_\alpha - \Gamma_\alpha(0)\right) - C\nabla^B\mu\Gamma_\alpha\right] g_\alpha^{eq}|_{(\mathbf{x},t)} \\ &+ \frac{\delta t}{2}\left(\mathbf{c}_\alpha - \mathbf{u}\right) \cdot \left[\nabla^C \rho c_s^2 \left(\Gamma_\alpha - \Gamma_\alpha(0)\right) - C\nabla^C\mu\Gamma_\alpha\right] g_\alpha^{eq}|_{(\mathbf{x}+\mathbf{c}_\alpha\delta t, t+\delta t)}\end{aligned} \tag{4.19}$$

In the previous equation there is the contemporary presence of two kinds of derivatives used in the computation, the centered one and the biased one, which will be deeply analyzed.
The LBE is obtained by discretizing the equations (4.17 and 4.19)

along the characteristics over a timestep $\delta t$. Considering the following non-linear transformation [40]:

$$\begin{aligned}\bar{g}_\alpha = g_\alpha + \frac{1}{2\tau}\left(g_\alpha - g_\alpha^{eq}\right) \\ - \frac{\delta t}{2}\left(\mathbf{c}_\alpha - \mathbf{u}\right)\cdot\left[\nabla^C \rho c_s^2\left(\Gamma_\alpha - \Gamma_\alpha\left(0\right)\right) - C\nabla^C \mu\Gamma_\alpha\right]\end{aligned} \tag{4.20}$$

$$\bar{g}_\alpha^{eq} = g_\alpha^{eq} - \frac{\delta t}{2}\left(\mathbf{c}_\alpha - \mathbf{u}\right)\cdot\left[\nabla^C \rho c_s^2\left(\Gamma_\alpha - \Gamma_\alpha\left(0\right)\right) - C\nabla^C \mu\Gamma_\alpha\right] \tag{4.21}$$

second-order integration in time (Crank-Nicolson), finally leads to the following LBE for pressure field:

$$\begin{aligned}\bar{g}_\alpha\left(\mathbf{x} + \mathbf{c}_\alpha\delta t, t + \delta t\right) - \bar{g}_\alpha\left(\mathbf{x}, t\right) = -\frac{1}{\tau + 0.5}\left(\bar{g}_\alpha - \bar{g}_\alpha^{eq}\right)\left(\mathbf{x}, t\right) \\ + \delta t\left(\mathbf{c}_\alpha - \mathbf{u}\right)\cdot\left[\nabla^M \rho c_s^2\left(\Gamma_\alpha - \Gamma_\alpha\left(0\right)\right) - C\nabla^M \mu\Gamma_\alpha\right]_{(\mathbf{x},t)}\end{aligned} \tag{4.22}$$

where the mean gradient $\nabla^M$ is evaluated as a mixed difference. More specifically, the discretization has realized in two different manners the directional one, where the $\nabla$ operator is multiplied for a characteristic velocity $\mathbf{c}_\alpha$, and the global one where the involved velocity is the macroscopic $\mathbf{u}$. The centered and biased directional derivatives for density can be expressed as:

$$\begin{aligned}\mathbf{c}_\alpha \cdot \nabla^B \rho\big|_{(\mathbf{x})} &= \frac{-\rho\left(\mathbf{x} + 2\mathbf{c}_\alpha\delta t\right) + 4\rho\left(\mathbf{x} + \mathbf{c}_\alpha\delta t\right) - 3\rho\left(\mathbf{x}\right)}{2} \\ \mathbf{c}_\alpha \cdot \nabla^C \rho\big|_{(\mathbf{x})} &= \frac{\rho\left(\mathbf{x} + \mathbf{c}_\alpha\delta t\right) - \rho\left(\mathbf{x} - \mathbf{c}_\alpha\delta t\right)}{2}\end{aligned} \tag{4.23}$$

while the global ones can be written as:

$$\begin{aligned}\nabla^B \rho\big|_{(\mathbf{x})} &= \sum_{\alpha=1}^{N} \frac{-\rho\left(\mathbf{x} + 2\mathbf{c}_\alpha\delta t\right) + 4\rho\left(\mathbf{x} + \mathbf{c}_\alpha\delta t\right) - 3\rho\left(\mathbf{x}\right)}{2c_s^2\delta t} \\ \nabla^C \rho\big|_{(\mathbf{x})} &= \sum_{\alpha=1}^{N} \frac{\rho\left(\mathbf{x} + \mathbf{c}_\alpha\delta t\right) - \rho\left(\mathbf{x} - \mathbf{c}_\alpha\delta t\right)}{2c_s^2\delta t}\end{aligned} \tag{4.24}$$

Thus, the mixed derivatives (directional and global) in equation 4.22 may be recast as:

$$\begin{aligned}\mathbf{c}_\alpha \cdot \nabla^M \rho &= \frac{1}{2}\left(\mathbf{c}_\alpha \cdot \nabla^B \rho + \mathbf{c}_\alpha \cdot \nabla^C \rho\right) \\ \nabla^M \rho &= \frac{1}{2}\left(\nabla^B \rho + \nabla^C \rho\right)\end{aligned} \tag{4.25}$$

The same procedure can be applied to the concentration $C$, by introducing a second distribution $h_\alpha = (C/\rho)\, f_\alpha$, $h_\alpha^{eq} = (C/\rho)\, f_\alpha^{eq}$, which can be shown to obey the following LBE:

$$\begin{aligned}&\bar{h}_\alpha\left(\mathbf{x} + \mathbf{c}_\alpha \delta t, t + \delta t\right) - \bar{h}_\alpha\left(\mathbf{x}, t\right) = -\frac{1}{\tau + 0.5}\left(\bar{h}_\alpha - \bar{h}_\alpha^{eq}\right)(\mathbf{x}, t) \\ &+ \delta t\left(\mathbf{c}_\alpha - \mathbf{u}\right) \cdot \left[\nabla^M C - \frac{C}{\rho c_s^2}\left(\nabla^M p_1 + C \nabla^M \mu\right)\right] \Gamma_\alpha|_{(\mathbf{x},t)} \\ &+ \delta t \nabla \cdot \left(M \nabla \mu\right) \Gamma_\alpha|_{(\mathbf{x},t)}\end{aligned} \tag{4.26}$$

where the modified equilibrium distribution $\bar{h}_\alpha$ and its equilibrium are calculated as in (4.20) and (4.21), namely:

$$\begin{aligned}\bar{h}_\alpha^{eq} = h_\alpha^{eq} &- \frac{\delta t}{2}\left(\mathbf{c}_\alpha - \mathbf{u}\right) \cdot \left[\nabla^C C - \frac{C}{\rho c_s^2}\left(\nabla^C p_1 + C \nabla^C \mu\right)\right] \Gamma_\alpha|_{(\mathbf{x},t)} \\ &- \frac{\delta t}{2} \nabla \cdot \left(M \nabla \mu\right) \Gamma_\alpha|_{(\mathbf{x},t)}\end{aligned} \tag{4.27}$$

In the above $M$ is the mobility, a chemical factor which rules the velocity of the convergence to the equilibrium. In Lee's work [28] it is shown that spurious currents decrease rapidly as $M$ is increased. At the endo of this part, it should be pointed out as the forcing in equilibrium and collision phases is carried out in two different manners. In fact, in order to ensure stability to the adopted scheme, the

derivatives discretization scheme adopted for the equilibrium phase is a standard central apporach, while a biased second neighbour scheme has adopted for the collision forcing phase. As will be explained in following paragraph this eterogenous derivatives discretizaion could lead to mass conservation issues.
The composition, the hydrodynamic pressure and the momentum are calculated by taking the zeroth and the first moments of the modified particle distribution function:

$$C = \sum_{\alpha} \bar{h}_{\alpha} + \frac{\delta t}{2} \nabla \cdot (M \nabla \mu) \tag{4.28}$$

$$\rho c_s^2 \mathbf{u} = \sum_{\alpha} \mathbf{c}_{\alpha} \bar{g}_{\alpha} - \frac{\delta t}{2} C \nabla \mu \tag{4.29}$$

$$p_1 = \sum_{\alpha} \bar{g}_{\alpha} + \frac{\delta t}{2} \mathbf{u} \cdot \nabla \rho c_s^2 \tag{4.30}$$

The equation (4.28) is non linear, because the equilibrium chemical potential $\mu$ is a function of the composition $C$. This means that, in principle, $\mu$ should be obtained by solving the nonlinear equation $\mu = \mu(C)$ by iteration at each lattice site. However, due to the slow variation of the chemical potential on the time-scale of a single time-step, in our implementation, $C$ at time $t$ is updated with the value of $\mu$ at the previous time-step $t - \delta t$, as suggested in [31]. On the other hand, the other gradients necessary for evaluating hydrodynamic properties are updated immediately after the definition of concentration. Thus, after having upgraded the concentration, new values for chemical potential and gradients have evaluated and used for upgrading those quantities.
The density and the relaxation time are calculated as local functions

of the composition

$$\begin{aligned} \rho(C) &= C\rho_1 + (1-C)\rho_2 \\ \tau(C) &= C\tau_1 + (1-C)\tau_2 \end{aligned} \tag{4.31}$$

The additional terms proportional to $\delta t$ in eqns. (4.28), (4.29) and (4.30), are introduced in order to cancel the contribution of the forces to the mass conservation.

## 4.2 The Derivatives Discretization

Crucial to the successful implementation of the Lee model is the proper discretization of the forcing terms:

$$\begin{aligned} F_\alpha^{(g)} &= (\mathbf{c}_\alpha - \mathbf{u}) \cdot \left[\nabla \rho c_s^2 \left(\Gamma_\alpha - \Gamma_\alpha(0)\right) - C\nabla\mu\Gamma_\alpha\right]_{(\mathbf{x},t)} \\ F_\alpha^{(h)} &= (\mathbf{c}_\alpha - \mathbf{u}) \cdot \left[\nabla C - \frac{C}{\rho c_s^2}\left(\nabla p_1 + C\nabla\mu\right)\right]\Gamma_\alpha|_{(\mathbf{x},t)} \\ &+ \nabla \cdot (M\nabla\mu)\,\Gamma_\alpha|_{(\mathbf{x},t)} \end{aligned} \tag{4.32}$$

Both terms are prefactored by the peculiar velocities $\mathbf{c}_\alpha - \mathbf{u}$, which, once summed upon over all discrete speeds, automatically cancel, as it is appropriate for a mass-conserving term. *However, this property is broken by the Lee discretization.* To appreciate this point, let us rewrite both forces as the sum of separate pieces, moving along the molecular and fluid speed directions, respectively

$$\begin{aligned} F_\alpha^{(g)} &= \mathbf{c}_\alpha \cdot \nabla A\Gamma_\alpha - \mathbf{u} \cdot \nabla A\Gamma_\alpha \\ F_\alpha^{(h)} &= \mathbf{c}_\alpha \cdot \nabla B\Gamma_\alpha - \mathbf{u} \cdot \nabla B\Gamma_\alpha + \nabla \cdot (M\nabla\mu)\,\Gamma_\alpha \end{aligned} \tag{4.33}$$

In the above, $A$ and $B$ represent generic space-time dependent quantities to be discretized.

The term corresponding to the microscopic velocity is discretized along the characteristics, instead the other one, corresponding to the macroscopic velocity, is discretized using standard gradients ([28] and Lee private communication).

The gradient along the characteristics which approximates $\mathbf{c}_\alpha \cdot \nabla A$ can be expanded to the first and second order, respectively, as follows:

$$\mathbf{c}_\alpha \cdot \nabla^C A|_{(\mathbf{x},t)} = \frac{A(\mathbf{x} + \mathbf{c}_\alpha \delta t) - A(\mathbf{x} - \mathbf{c}_\alpha \delta t)}{2} \tag{4.34}$$

$$\mathbf{c}_\alpha \cdot \nabla^M A|_{(\mathbf{x},t)} = \frac{5A(\mathbf{x} + \mathbf{c}_\alpha \delta t) - 3A(\mathbf{x}) - A(\mathbf{x} + 2\mathbf{c}_\alpha \delta t) - A(\mathbf{x} - \mathbf{c}_\alpha \delta t)}{4} \tag{4.35}$$

where the superscript $M$ denotes the mixed derivatives scheme, which is a linear composition of centered and biased.
The same approximation is used for the other forcing term $\mathbf{c}_\alpha \cdot \nabla C\Gamma_\alpha$.

It should be noticed that each different direction leads to a separate discretization stencil, i.e. it is a Lagrangian discretization along the characteristics defined by the discrete velocities.

The standard (non-Lagrangian) discretization consists of two different gradients, the first-order centered and the second-order biased, respectively:

$$\begin{aligned}
\nabla^C A|_{(x)} &= \sum_{\alpha \neq 0} \frac{w_\alpha \mathbf{c}_\alpha \left[A(\mathbf{x} + \mathbf{c}_\alpha \delta t) - A(\mathbf{x} - \mathbf{c}_\alpha \delta t)\right]}{2c_s^2 \delta t} \\
\nabla^B A|_{(x)} &= \sum_{\alpha \neq 0} \frac{w_\alpha \mathbf{c}_\alpha \left[-A(\mathbf{x} + 2\mathbf{c}_\alpha \delta t) + 4A(\mathbf{x} + \mathbf{c}_\alpha \delta t) - 3A(\mathbf{x})\right]}{2c_2^2 \delta t}
\end{aligned} \tag{4.36}$$

The use of a second order is necessary to ensure the stability to the method. In the different phases of the simulation, the first order approximation is used for the forcing term of the equilibrium distributions defined in eqns. (4.21) and (4.27), the second order is used for the force applied to the collision operators of Eqns. (4.22) and (4.26). As an example the equilibrium and collision forcing will be reported as they are implemented in current code version. In following lines, the equilibrium forcing routine is reported:

```
do j = syr,eyr
 do i = sxr,exr
  cc(i,j)      = 1.d0/(rho(i,j)*cs_2)
  do k = 0,npop-1
   fr1          = rhofo(k,i,j)
   fr2          = u(i,j)*gcentx_rho(i,j) + v(i,j)*gcenty_rho(i,j)
   fm1          = mufo(k,i,j)
   fm2          = u(i,j)*gcentx_mu(i,j) + v(i,j)*gcenty_mu(i,j)
   fr           = (fr1 - fr2)*cs_2*(Gamma(k,i,j) - w(k))
   fm           = (fm1 - fm2)*C(i,j)*Gamma(k,i,j)
   geqpf(k,i,j) = geq(k,i,j) - 0.5d0*(fr - fm)
   fC1          = Cfo(k,i,j)
   fC2          = u(i,j)*gcentx_C(i,j) + v(i,j)*gcenty_C(i,j)
   fp11         = p1fo(k,i,j)
   fp12         = u(i,j)*gcentx_p1(i,j) + v(i,j)*gcenty_p1(i,j)
   fm1          = mufo(k,i,j)
   fm2          = u(i,j)*gcentx_mu(i,j) + v(i,j)*gcenty_mu(i,j)
   fC           = (fC1 - fC2))*Gamma(k,i,j)
   fp1          = (fp11 - fp12)*Gamma(k,i,j)*C(i,j)*cc(i,j)
   fm           = (fm1 - fm2)*Gamma(k,i,j)*C(i,j)*C(i,j)*cc(i,j)
   f2m          = Mm*secder_mu(i,j)*Gamma(k,i,j)
   heqpf(k,i,j) = heq(k,i,j) - 0.5d0*(fC - fp1 - fm + f2m)
  enddo
 enddo
enddo
```

As pointed out before, in the collision forcing a second neighbour

differentiation has been used. This becomes apparent by looking at following codelines. It should be noticed that the mean value for gradients has used only for global quantities, in fact, for directional derivatives, only the mixed differentiation has applied.

```
do j = syr,eyr
 do i = sxr,exr
  cc        = 1.d0/(rho(i,j)*cs_2)
  gradmrhox = 0.5d0*(gcentx_rho(i,j) + gbiasx_rho(i,j))
  gradmrhoy = 0.5d0*(gcenty_rho(i,j) + gbiasy_rho(i,j))
  gradmmux  = 0.5d0*(gcentx_mu(i,j)  + gbiasx_mu(i,j))
  gradmmuy  = 0.5d0*(gcenty_mu(i,j)  + gbiasy_mu(i,j))
  gradmCx   = 0.5d0*(gcentx_C(i,j)   + gbiasx_C(i,j))
  gradmCy   = 0.5d0*(gcenty_C(i,j)   + gbiasy_C(i,j))
  gradmp1x  = 0.5d0*(gcentx_p1(i,j)  + gbiasx_p1(i,j))
  gradmp1y  = 0.5d0*(gcenty_p1(i,j)  + gbiasy_p1(i,j))
  do k = 0,npop-1
   fr1      = rhoso(k,i,j)
   fr2      = u(i,j)*gradmrhox + v(i,j)*gradmrhoy
   fm1      = muso(k,i,j)
   fm2      = u(i,j)*gradmmux + v(i,j)*gradmmuy
   fr       = (fr1 - fr2)*cs_2*(Gamma(k,i,j) - w(k))
   fm       = (fm1 - fm2)*C(i,j)*Gamma(k,i,j)
   g(k,i,j) = g(k,i,j) + (fr - fm)
   fg(i,j)  = (fr - fm)
   fC1      = Cso(k,i,j)
   fC2      = u(i,j)*gradmCx + v(i,j)*gradmCy
   fp11     = p1so(k,i,j)
   fp12     = u(i,j)*gradmp1x + v(i,j)*gradmp1y
   fm1      = muso(k,i,j)
   fm2      = u(i,j)*gradmmux + v(i,j)*gradmmuy
   fC       = (fC1 - fC2)*Gamma(k,i,j)
   fp1      = (fp11 - fp12)*Gamma(k,i,j)*C(i,j)*cc
   fm       = (fm1 - fm2)*Gamma(k,i,j)*C(i,j)*C(i,j)*cc
   f2m      = Mm*secder_mu(i,j)*Gamma(k,i,j)
```

```
    h(k,i,j) = h(k,i,j) + (fC - fp1 - fm + f2m)
    fh(i,j)  = (fC - fp1 - fm + f2m)
   end do
  end do
 end do
```

Presenting now the derivatives definition, at least for one componente, is useful. In following lines the first and second neighbour global derivatives are presented:

```
 do j = syr,eyr
  do i = sxr,exr
   do k = 1,npop-1
    !CENTERED
    c_x             = cx(k)
    c_y             = cy(k)
    gcentx_rho(i,j) = gcentx_rho(i,j) + &
     &                w(k)*cx(k)*csd*(rho(i+c_x,j+c_y) &
     &                              - rho(i-c_x,j-c_y))
    !BIASED
    c_x             = cx(k)
    c_y             = cy(k)
    gbiasx_rho(i,j) = gbiasx_rho(i,j) + w(k)*cx(k)*csd*(&
     & -rho(i+2*c_x,j+2*c_y)+4.d0*rho(i+c_x,j+c_y)-3.d0*rho(i,j))
   end do
  end do
 end do
```

On the other hand, directional derivatives, evaluated for every direction, will be discretized in two different manners (again first and second neighbour) each of one used or in the equilibrium or in the collision forcing.

```
 do j = syr,eyr
  do i = sxr,exr
   do k = 0,npop-1
```

```
    xpuu          = i + 2*cx(k)
    ypuu          = j + 2*cy(k)
    xpu           = i + cx(k)
    ypu           = j + cy(k)
    xp0           = i
    yp0           = j
    xpd           = i - cx(k)
    ypd           = j - cy(k)
    r2            = rho(xpuu,ypuu) - rho(xpu,ypu)
    r1            = rho(xpu,ypu) - rho(xp0,yp0)
    r0            = rho(xp0,yp0) - rho(xpd,ypd)
    rhoso(k,i,j) = r1 - 0.25d0*(r2 - r0)
    rhofo(k,i,j) = r1 - 0.5d0*(r1 - r0)
   end do
  end do
 end do
```

By writing the discretized forcing terms for each population and summing up all contributions, it is possible to demonstrate that this method is numerically non-conservative. In fact, using only a first order approximation, the method is completely conservative, but in the collision phase there appears a spurious contribution due to the imbalance between the finite differencing over the characteristics and the local fluid direction. The main problem is that the coefficients in the second order discretization are different between the flow gradient and the one evaluated along the characteristics. In fact, if these coefficients were equal, the local contribution of this "hybrid" of discretization would be zero.
For example, assuming the forcing term written as in equation (4.33), the spurious non-conservative contribution of the global forcing is obtained by summing the correction terms over all the populations.
We notice that the last term, with the second order derivative is not

expanded because it cancels out in the eqn. (4.28). It is important to underline that this discretization is non-conservative, as some terms in the local force are different from zero. In particular, the discretization is conservative for the case of no-flow ($u = v = 0.0$) and/or A and B are trivially constant. Nevertheless, simulation practice shows that the non-conservative term, although non-zero at each lattice site, particularly near the interface, does not appreciably perturb the actual solution. Moreover the total mass (sum over all lattice sites) is conserved. Similar considerations apply to the fluid momentum, whose lack of conservation might have implications on the Galilean invariance of the model. This remains as a standing issue for future investigations of the properties of the Lee's model.

$$
\begin{aligned}
&\sum_{\alpha} F_{\alpha}^{(h)} = -\frac{3}{4}B(i,j)\sum_{\alpha=1}^{8}\Gamma_{\alpha}+ \\
&+ B(i+1,j)\left[\frac{5}{4}\Gamma_1 - \frac{1}{4}\Gamma_3 - \frac{2uw_1}{c_s^2}\right] + B(i-1,j)\left[\frac{5}{4}\Gamma_3 - \frac{1}{4}\Gamma_1 + \frac{2uw_3}{c_s^2}\right] + \\
&+ B(i+2,j)\left[-\frac{1}{4}\Gamma_1 + \frac{uw_1}{2c_s^2}\right] + B(i-2,j)\left[-\frac{1}{4}\Gamma_3 - \frac{uw_3}{2c_s^2}\right] + \\
&+ B(i,j+1)\left[\frac{5}{4}\Gamma_2 - \frac{1}{4}\Gamma_4 - \frac{2vw_2}{c_s^2}\right] + B(i,j-1)\left[\frac{5}{4}\Gamma_4 - \frac{1}{4}\Gamma_2 + \frac{2vw_4}{c_s^2}\right] + \\
&+ B(i,j+2)\left[-\frac{1}{4}\Gamma_2 + \frac{vw_2}{2c_s^2}\right] + B(i,j-2)\left[-\frac{1}{4}\Gamma_4 - \frac{vw_4}{2c_s^2}\right] + \\
&+ B(i+1,j+1)\left[\frac{5}{4}\Gamma_5 - \frac{1}{4}\Gamma_7 - \frac{2\left(u+v\right)w_5}{c_s^2}\right] + \\
&+ B(i-1,j-1)\left[\frac{5}{4}\Gamma_7 - \frac{1}{4}\Gamma_5 + \frac{2\left(u+v\right)w_7}{c_s^2}\right] + \\
&+ B(i+2,j+2)\left[-\frac{1}{4}\Gamma_5 - \frac{\left(u+v\right)w_5}{2c_s^2}\right] + \\
&+ B(i-2,j-2)\left[-\frac{1}{4}\Gamma_7 + \frac{\left(u+v\right)w_7}{2c_s^2}\right] + \\
&+ B(i-1,j+1)\left[\frac{5}{4}\Gamma_6 - \frac{1}{4}\Gamma_8 + \frac{2\left(u-v\right)w_6}{c_s^2}\right] + \\
&+ B(i+1,j-1)\left[\frac{5}{4}\Gamma_8 - \frac{1}{4}\Gamma_6 - \frac{2\left(u-v\right)w_8}{c_s^2}\right] + \\
&+ B(i-2,j+2)\left[-\frac{1}{4}\Gamma_6 + \frac{\left(u-v\right)w_6}{2c_s^2}\right] + \\
&+ B(i+2,j-2)\left[-\frac{1}{4}\Gamma_8 - \frac{\left(u-v\right)w_8}{2c_s^2}\right] + \\
&+ \nabla\left(M\cdot\nabla\mu\right)
\end{aligned}
\tag{4.37}
$$

### 4.2.1 Static Droplet - Conservation of Mass

In order to understand the influence of non-conservative contribution term on simulation we analized the behaviour of a static droplet immersed in a continuous domain. A drop of liquid with radius $R = 25$ is initialized in the centre of a fully periodic box, being the interface thickness D equal to 4 lattice sites. The density ratio between liquid and vapor phases $\frac{\rho_l^{sat}}{\rho_v^{sat}}$ is set to 1000. The simulation is stopped when the kinetic energy, defined as $KE = \sum_{domain} \frac{\left(u^2+v^2\right)}{2}$, becomes practically constant.

Figure 4.1 shows that KE is constantly decreasing until its minimum value, reached after about $4 \times 10^5$ iterations, and then remains nearly constant for the following $6 \times 10^5$ iterations.

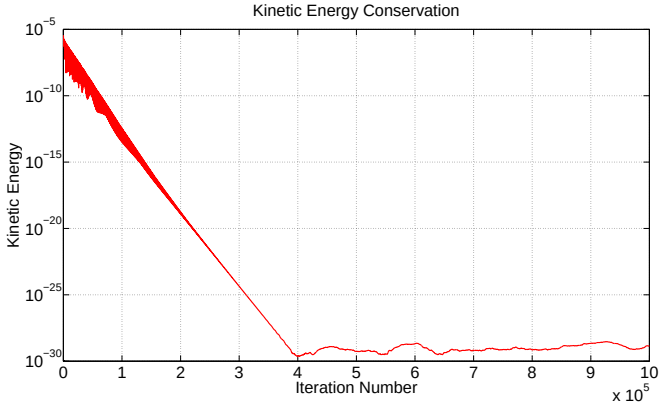


Figure 4.1: Time evolution of the kinetic energy for the case of a static drop. After $4 \times 10^5$ the kinetic energy reaches value near the round-off precision of the machine and remains practically constant. The main parameters are: $R = 25$, $\frac{\rho_l^{sat}}{\rho_v^{sat}} = 1000.0$, $\frac{\tau_v}{\tau_l} = 10.0$. The grid resolution is 100x100.

The non-conservative effect of the discretization is apparent from Figure 4.2, which shows the distribution of the local force, summed over all the populations. However, the non-conservative term of the forcing, still present in the lattice sites of the interface zone (black line in Figure 4.2), has negligible effects on the total mass variation, as shown in Figure 4.3.

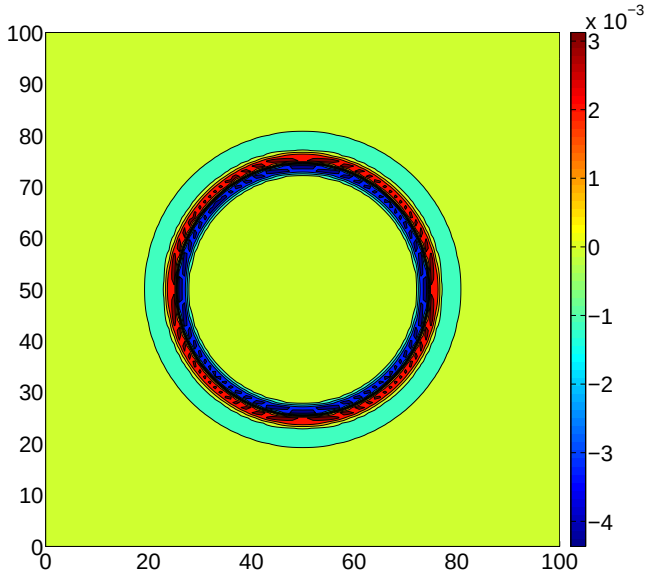


Figure 4.2: Contour plot of the spurious force after the collision phase, evaluated after $10^6$ time-steps. As expected, the spurious force is peaked around the interface. The main parameters are: $R = 25$, $\frac{\rho_l^{sat}}{\rho_v^{sat}} = 1000.0$, $\frac{\tau_v}{\tau_l} = 10.0$. The grid resolution is 100x100..

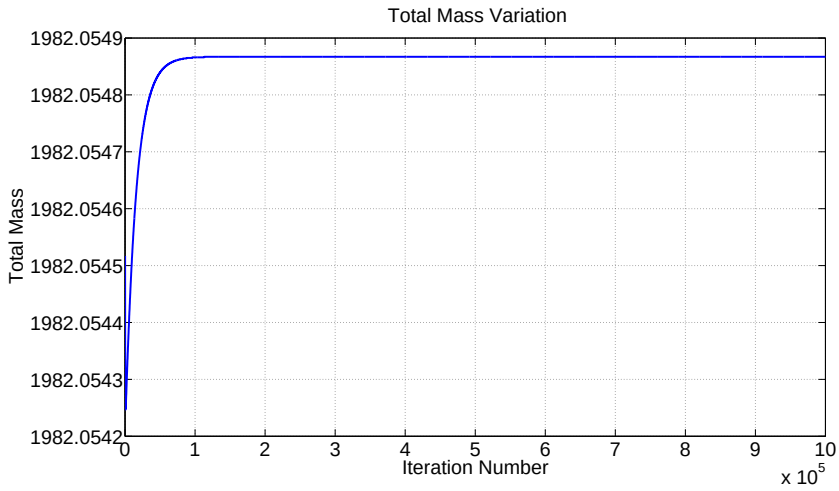


Figure 4.3: Conservation of the total mass for the static drop. As expected the spurious force has no effect on the value of the total mass. The main parameters are: $R = 25$, $\frac{\rho_l^{sat}}{\rho_v^{sat}} = 1000.0$, $\frac{\tau_v}{\tau_l} = 10.0$. The grid resolution is 100x100.

## 4.3 The Algorithm

In this chapter the general solving algorithm for a standard Lattice Boltzmann Method will be briefly described before introducing the one used for the multiphase free-energy approach. As described in chapter 2 the LBM is composed of two different interaction phases, the streaming - where the information are passed through neighbour sites along allowed directions - and the collision - where there is the effective exchange of momentum. In the following figure 4.4 is reported a standard scheme for one phase model, highlighting the equations solved step by step.

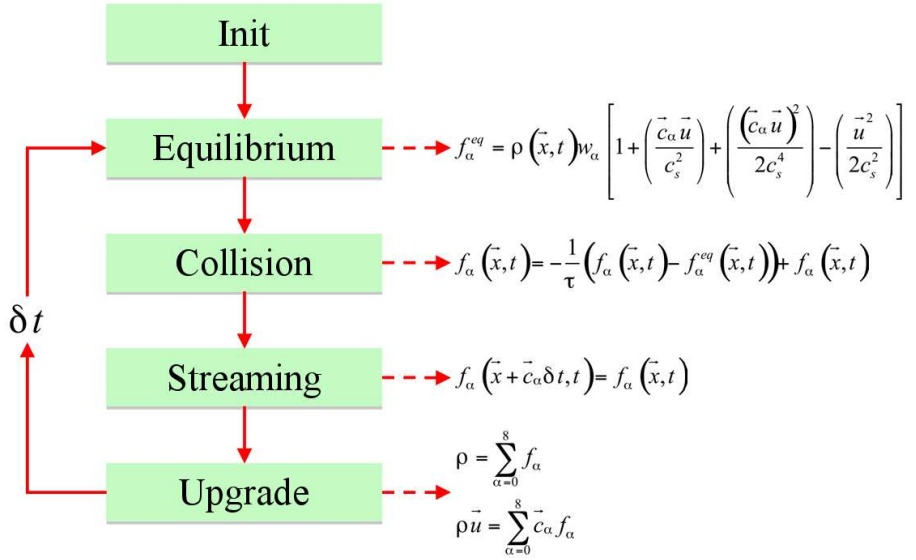


Figure 4.4: Schematic flow chart for standard one phase Lattice Boltzmann Method.

As can be seen from Fig. 4.4, the timestep finishes with the evaluation of new macroscopic fields values, which will be used for the new equilibrium distribution function for the next timestep.
This simple procedure can be used as weel for the multiphase models only with adding intermediate phases which take into account the presence of intermolecular potential. More specifically, for the Lee model the following flow chart, reported in figure 4.5, has been used. For sake of simplicity, in this representation the equations will not reported.

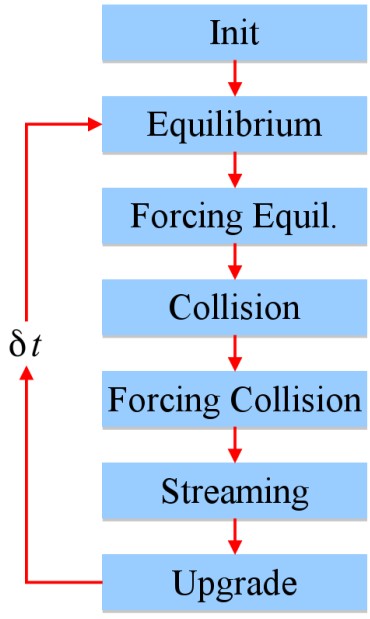


Figure 4.5: Flow chart for Lee model solving algorithm.

All the equations needed in order to solve the above reported flow chart are written in chapter 3 with the derivatives discretization deeply discussed in the previous section.

## 4.4 Paralelization Procedure

In order to improve the possible problems which can be solved with the current model especially addressed to a three-dimensional analysis, a parallel version of the code has been implemented. In the current paragraph some features of parallel code will be presented.
First of all, a short introduction to possible hardware layout should

be done in order to understand and define the paralalezation strategy. In fact, following the memory architecture a parallelizing structure can be preferred to another. Basically we speak in terms of shared or distributed memory depending on the fact of having one block of memory for every processor (*distributed*) or one block of memory for the whole set of processors (*shared*). A clearer description is reported in the following figure 4.4.

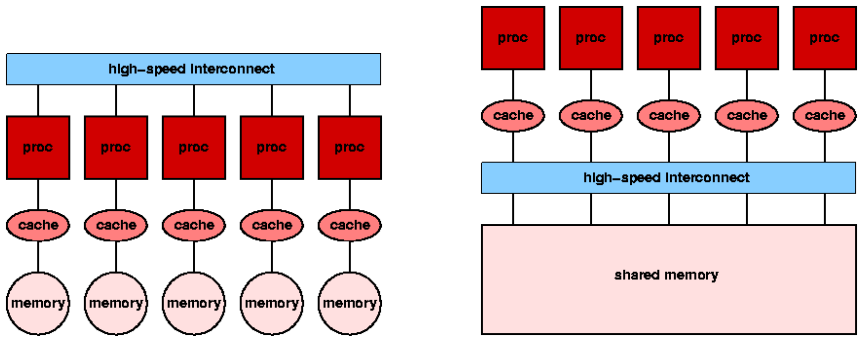


(a) Distributed Memory (b) Shared Memory

Figure 4.6: Graphical comparison between distributed 4.6(a) and shared 4.6(b) memory architecture.

In the current work we focued on shared memory systems, implemented with OpenMPI.
The code is structerd in order to solve the same functions in different processors/cores for different regions of the studied domain. It is easy to understand that one of the priorities of the paralelization technique is the domain partitioning. In fact, in order to have almost the same computational request over all the processors involved in the numerical simulation, all of them should be charged of the same amount of

lattice sites. Luckly the applications analyzed allow this procedure to be done easly, considering cubical or similar domains. Thus in this analysis the domain decomposition technique is not analyzed, the only thing to focus on is the fact that there is the necessity of exchanging data at the interface between two processors. In fact, the population addresed to a lattice site which is part of the neighbouroud process should be sent to it through a series of sites called *halo*. In the following figure 4.7 the concept described above is clearly represented.

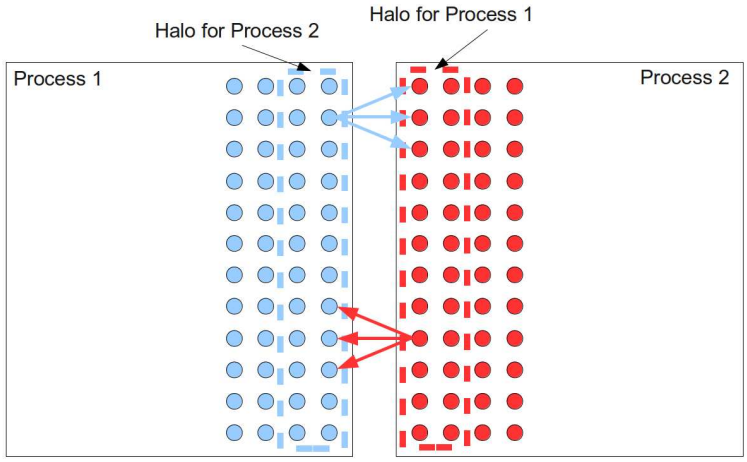


Figure 4.7: An example of halo between two neighbour processes.

As can be observed form fig. 4.7 the halo is composed from two layers because the model uses the second neighbour for the evaluation of gradients (the Biased one described above).
In the following figures some practical examples of domain decomposition procedure will be shown. Starting from the whole domain represented in fig. 4.8, it has been decomposed in different blocks as

shown in figure 4.9. The halo interface is shown on the figure 4.10

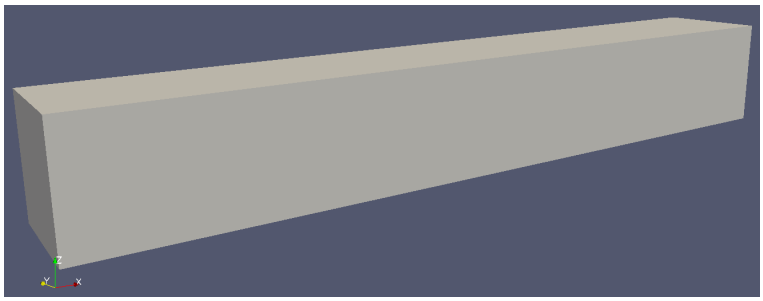

Figure 4.8: An example of domain to analyze.

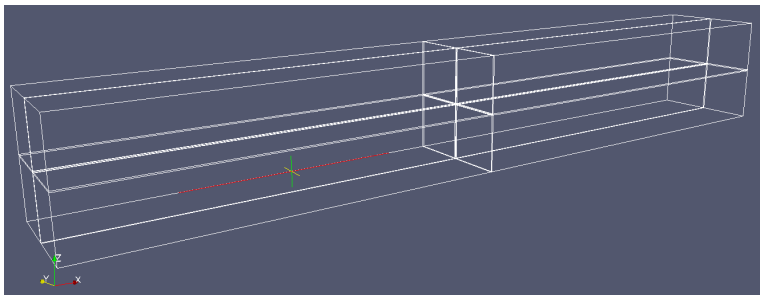

Figure 4.9: An example of domain decomposition.

As can be observed from the previous figure the domain decomposition is perfectly balanced thus asseures that there are not processors/cores overloaded in comparison to others, because each one executes the same amount of operations.

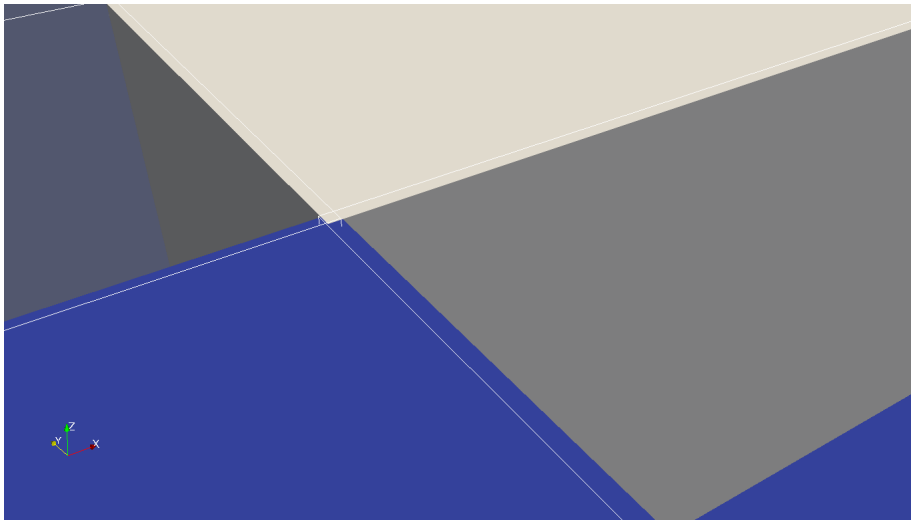

Figure 4.10: Interface between domains.

In the previous figure 4.10 can be observed as the different processes share some sites where take place the message passing in the parallel computing.

# Chapter 5

# Results

In this chapter some results obtained for a set of 2-dimensional multiphase flows will be presented, [37, 41]. More specifically three different test-cases will be studied, the primary break-up of a liquid jet uunder the effect of Rayleigh-Taylor instability, the secondary break-up of a liquid droplet under the effect of a gravitational field and, finally the coalescence of two impacting drops. In the last ssection some preliminary results of the parallel code developed will be shown with the aim of characterize the results obtained for a three dimensional analysis.

## 5.1 The Primary Break-Up

Next, we test the Lee model against a gravity-driven Rayleigh-Taylor (RT) instability, one of the most fundamental forms of interfacial instability between fluids of different densities, which has been extensively studied both numerically and experimentally [42].

The computational domain is a channel of width $W = 100$ and a height $H = 4W$. Symmetric boundary conditions are applied on the top and bottom wall and periodic boundary conditions are imposed at the side walls. The heavier fluid, initially placed above the lighter one, falls down under the effect of the gravity field when the interface is perturbed. Subsequently, as the heavy fluid moves downwards, a wave-like disturbance appears at the interface. Downward-moving 'spikes' and upward-moving 'bubbles' are observed. The initial perturbation of the interface is a sinusoidal function, with amplitude $A = 0.1W$ and wavelength $\lambda = 2\pi/W$. Being $g$ the gravity acceleration in lattice units, the characteristic velocity of the system is $U = \sqrt{W \cdot g}$, which has been set to 0.04 for all the simulations. The Lee model has been tested under different operating conditions, given in terms of non-dimensional parameters. The Reynolds number is defined as: $Re = \sqrt{Wg}W/\nu$ where $\nu$ is the fluid viscosity. The density ratio is measured in terms of the Atwood number, defined as: $At = (\rho_l - \rho_g)/\rho_l + \rho_g$ with $\rho_l$ and $\rho_g$ being the densities of the light and heavy fluids, respectively. The natural time-scale of the system is given by $T = \sqrt{W/g}$.

In order to assess the validity of the model, the present numerical results are compared with those obtained by He et al. [2]. The comparison has been performed for two different cases: a 256x1024 grid, with Re = 2048 and At = 0.5; a 128x512 grid, with Re=256 and At=0.5.

Figures 5.1 and 5.2 show the evolution of the fluid interface from He et al. [2] and from the Lee model, respectively, at a $Re = 2048$. The agreement with literature results is satisfactory. The flow field is qualitatively consistent with the typical RT instability dynamics, experimentally and numerically observed by various authors [43, 44, 45,

46, 47, 48]: the initial exponential growth, the rise bubble of the light fluid and the spikes of denser fluid moving in the opposite direction as well as the superficial wave breaking at a later stage of the simulation, are well visible.

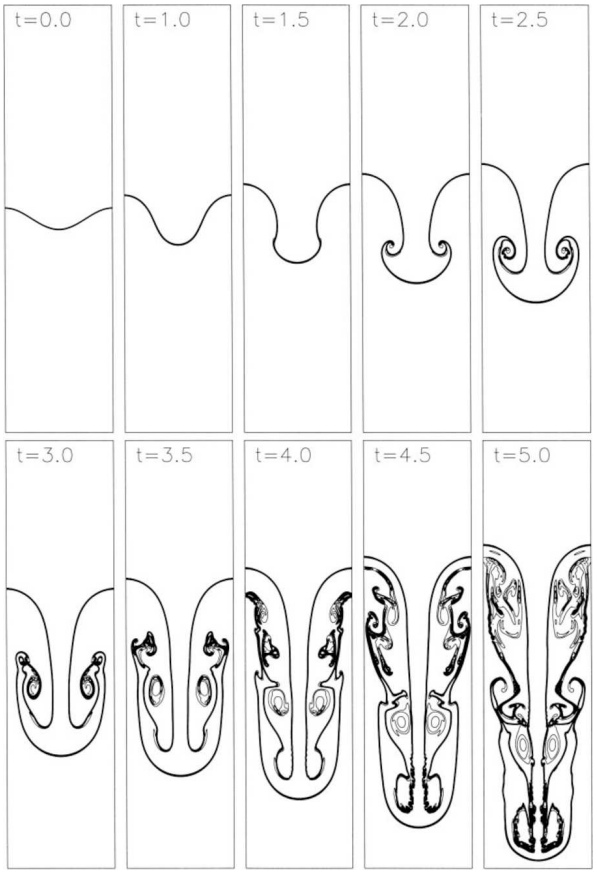


Figure 5.1: A sequence of density contours for the RT instability at different times, as presented in the reference [2]. The main parameters are: grid-size 256x1024, Re = 2048, At = 0.5 and $\sqrt{W \cdot g} = 0.04$.

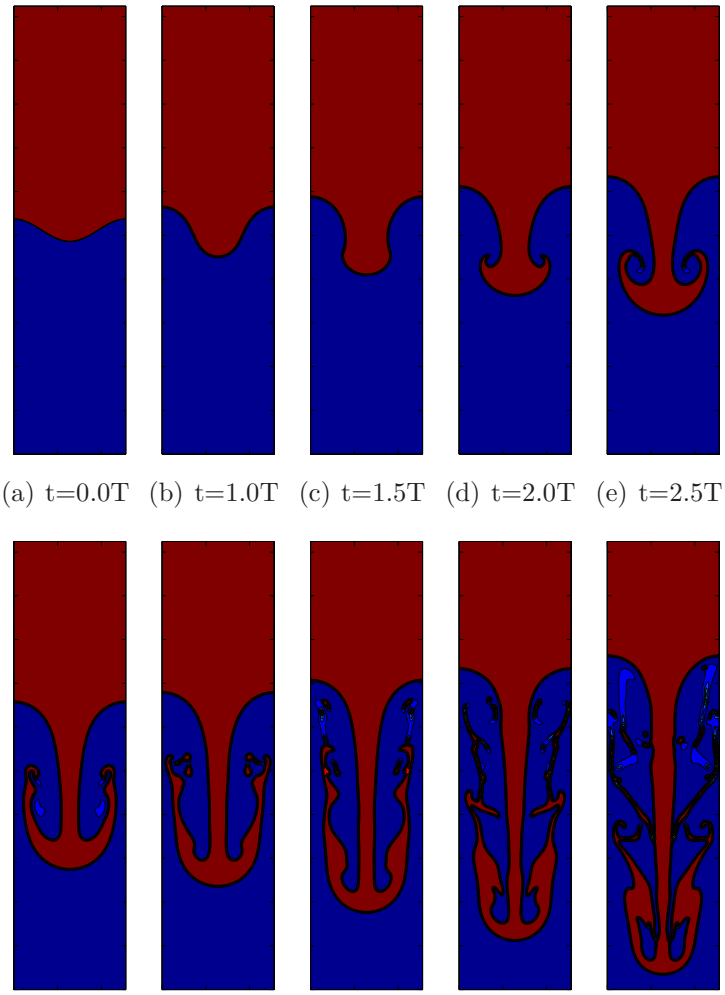

(a) t=0.0T (b) t=1.0T (c) t=1.5T (d) t=2.0T (e) t=2.5T

(f) t=3.0T (g) t=3.5T (h) t=4.0T (i) t=4.5T (j) t=5.0T

Figure 5.2: A sequence of density contours for the RT instability at different times, as computed with the Lee's model. The main parameters are: grid-size 256x1024, Re = 2048, At = 0.5 and $\sqrt{W \cdot g} = 0.04$.

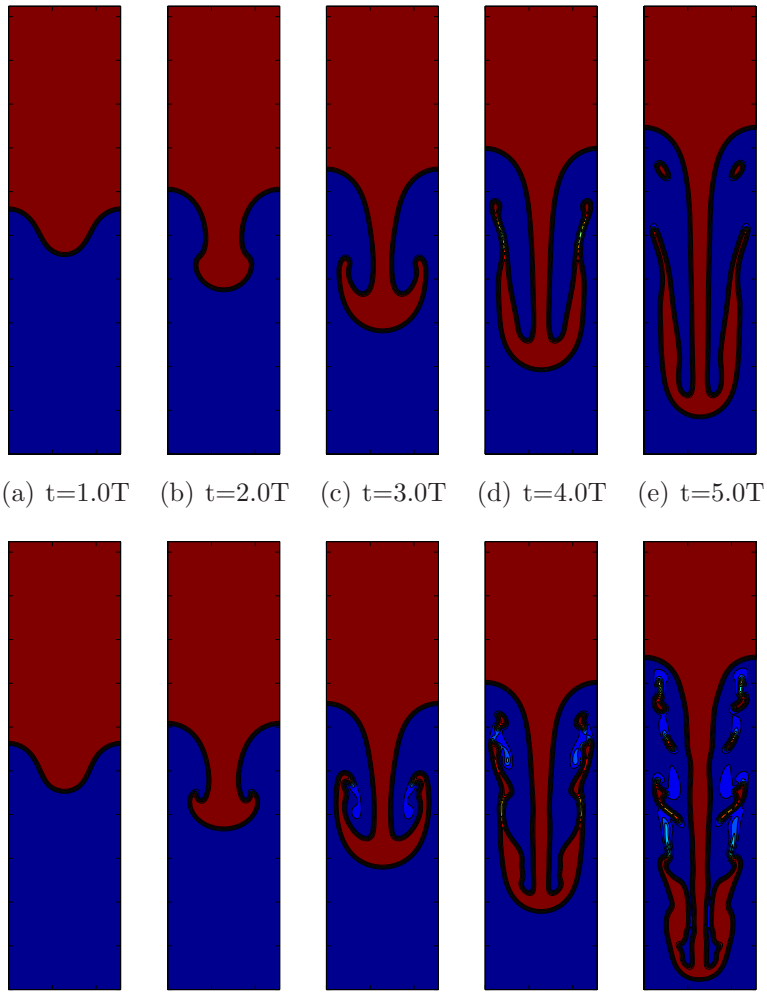

(a) t=1.0T (b) t=2.0T (c) t=3.0T (d) t=4.0T (e) t=5.0T

(f) t=1.0T (g) t=2.0T (h) t=3.0T (i) t=4.0T (j) t=5.0T

Figure 5.3: A sequence of density contours at different times as computed with the Lee's model - Two different Re are examined: 1)Re = 256 figure 5.3(a) to 5.3(e);2)Re = 2048 figs 5.3(f) to 5.3(j). Other parameters are: Grid size = 128 x 512, $At = 0.5$, $\sqrt{W \cdot g} = 0.04$.

A better insight is obtained by monitoring the evolution of the interface at low and high Re, shown in figure 5.3, which reveals significant differences at $t = 3T$. These are mainly related to the dense jet breakup: at high Re, more and smaller dense fluid elements separate from the main jet. A quantitative comparison with the literature data in terms of the spike and bubble leading front positions is given in Figure 5.4. Again, satisfactory agreement between our results and literature data is observed. Figure 5.4 reveals that the evolution of the global parameters is only marginally affected by the Reynolds number, as small differences are observed only at a later stage of the simulations.

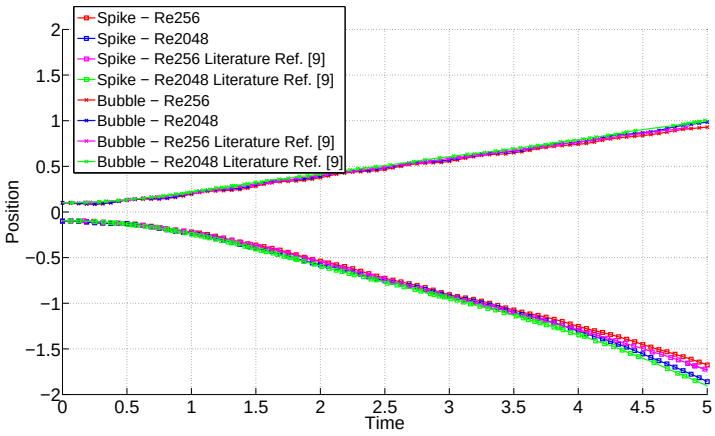


Figure 5.4: Position of the spike and bubble as a function of time. Comparison between the Lee's model and the literature data [2] for two different Re numbers. The main parameters are: grid size = 128 x 512, $At = 0.5$, $\sqrt{W \cdot g} = 0.04$. The examined Re number are 256 and 2048.

### 5.1.1 Lack of mass conservation

Inspection of mass-conservation for the RT instability (see Figure 5.5), shows indeed a deterioration with respect to the casde of a static droplet shown previously in this work. From Figure 5.5), it is seen that the relative mass non-conservation reaches up to $10^{-4}$ after $32,000$ timesteps, with a linear growth rate of about $10^{-8}$ per time step. Besides unsteadiness, which is inherent to the RT instability, this error growth could be related also to the effect of symmetric boundary conditions on the north/south walls. The development of optimal boundary conditions for the Lee model is an open research topic, which deserves a full study on its own. Nevertheless, we notice that for the test cases presented in this work, the error due to mass non-conservation appears to be sufficiently low to preserve the essential physics of the problem.

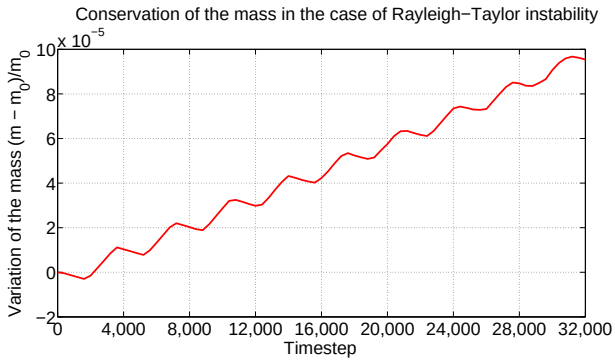


Figure 5.5: Conservation of the total mass for the Rayleigh-Taylor Instability. The variation of the mass respect to the initial condition is reported. The parameters of the simulation are $Re = 2048$, grid size $= 256$ x 1024, $At = 0.5$, $\sqrt{W \cdot g} = 0.04$.

### 5.1.2 Effect of the grid-size

The gravity-driven RT instability has been simulated at three different resolutions: $64 \times 256$; $128 \times 512$ and $256 \times 1024$. As reported in the following figure2, 5.6, the effect of grid size can be appreciated in terms of precision in solving the interface phenomena.

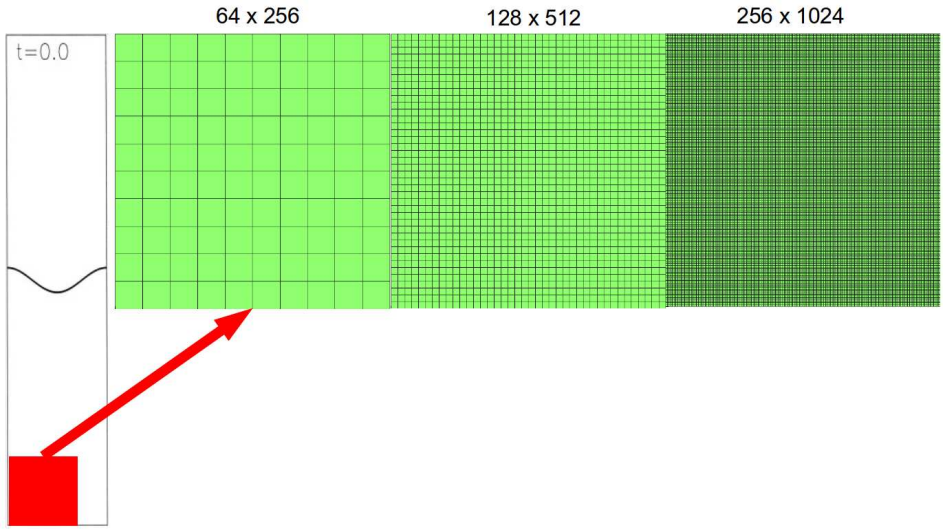


Figure 5.6: Influence of Grid Size resolution in solving the Rayleigh-Taylor Instability phenomenon.

The Reynolds and Atwood numbers have been set to 2048 and 0.5, respectively. As can be observed in figure **??**, which compares the fluid interface evolution with the different grids, the grid-resolution significantly affects the interface dynamics. The difference between the finest and the coarsest grids is evident at any stage of the RT instability growth, as the interface shape and the spike penetration

are clearly different already at $t = 2T$.
The effectiveness of the grid refinement, from $128 \times 512$ to $256 \times 1024$, becomes more apparent as the fluid interpenetration becomes turbulent and the scale of the wave disturbances becomes smaller. Since a coarser grid inevitably implies a larger interface thickness, liquid breakup is brought forward by the coarser grids, as well as the separated structures are smaller with the finest grid. Passing from the $128 \times 512$ to the $256 \times 1024$ grids, the differences in the jet shape become apparent only after 5T, a time at which the relevant scales of the flow have become smaller.

The differences are much less evident at the level of the main penetration parameters. The time evolutions of the falling spike and the rear bubble position are almost the same for the three grids, as shown in figures 5.7, 5.8 and 5.9.

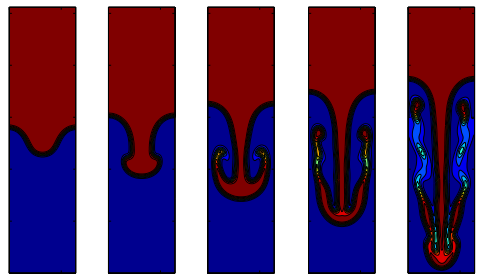

(a) t=1.0T (b) t=2.0T (c) t=3.0T (d) t=4.0T (e) t=5.0T

Figure 5.7: Grid Size effects. A sequence of density contours of RT instability at different times, as computed with the Lee's model with a grid-size of 64x256. Other parameters are: $Re = 2048$, $At = 0.5$, $\sqrt{W \cdot g} = 0.04$.

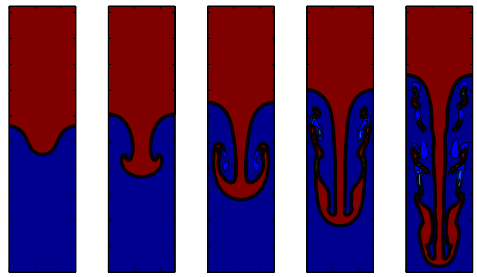

(a) t=1.0T (b) t=2.0T (c) t=3.0T (d) t=4.0T (e) t=5.0T

Figure 5.8: Grid Size effects. A sequence of density contours of RT instability at different times, as computed with the Lee's model with a grid-size of 128x512. Other parameters are: $Re = 2048$, $At = 0.5$, $\sqrt{W \cdot g} = 0.04$.

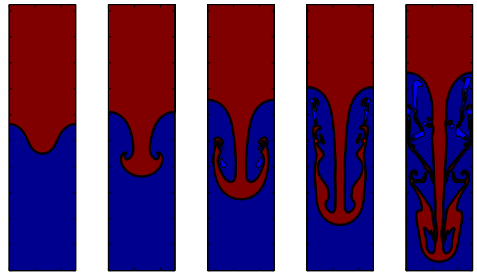

(a) t=1.0T (b) t=2.0T (c) t=3.0T (d) t=4.0T (e) t=5.0T

Figure 5.9: Grid Size effects. A sequence of density contours of RT instability at different times, as computed with the Lee's model with a grid-size of 256x1024. Other parameters are: $Re = 2048$, $At = 0.5$, $\sqrt{W \cdot g} = 0.04$.

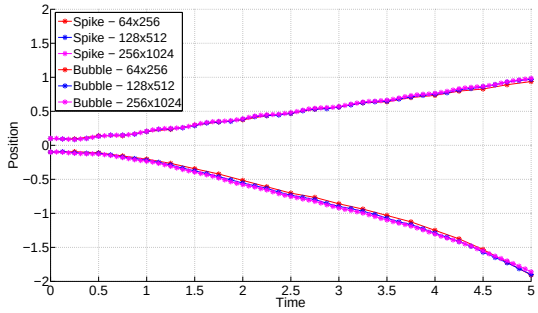


Figure 5.10: Grid Size effects on the evolution of the penetration of the bubble and the spike. No apparent differences can be appreciated for these "global" quantities. The main differences are shown in the previous figure, which shows the density contours at different times. Parameters: Re = 2048, At = 0.5 and $\sqrt{W \cdot g} = 0.04$. - Three different grids are examined: 64x256, 128x512 and 256x1024.

## 5.2 The Secondary Break-Up

Droplet deformation by aerodynamic forces is a complex phenomenon, in which the non-homogeneous pressure distribution on the surface of the bubble leads to shape deformation and eventually to droplet breakup, depending on the strength of inertial versus surface tension effects.
Exposing a droplet to a gas flow of increasing velocity, significant deformation starts at Weber numbers of unity and above a certain critical Weber number $We_c$, the deformation leads to breakup.

The critical Weber number for low-viscosity fluids is around 10. Depending on the intensity of the aerodynamic force, five distinct

regimes have been identified: vibrational, bag, chaotic, stripping and catastrophic, [3, 49].
In the following section, we analyze the capabilities of the present method to reproduce the aforementioned breakup regimes. The analysis is carried out in two spatial dimensions.
In Figure 5.11 a sketch of the problem is reported.

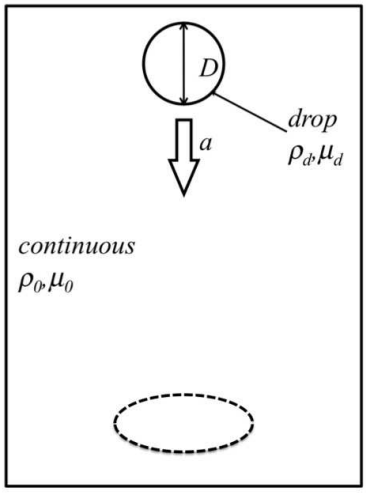


Figure 5.11: Schematic Representation of the break-up problem. The liquid droplet falls under the effect of a constant acceleration $a$.

As suggested by Tryggvason [3], the breakup problem is best analyzed in terms of the Eotvos, rather than Weber, number, because the former is directly related to the external acceleration, $a$. Another dimensionless group of interest is the Ohnesorge number, which combines the Reynolds and Weber numbers as follows:

$$Oh = \frac{\mu}{\sqrt{\rho D \sigma}} = We^{1/2} Re^{-1} \tag{5.1}$$

In order to facilitate comparisons between different simulations, a characteristic time $T = \sqrt{\frac{D}{a}}$ is introduced.

We have analyzed droplet break-up at a given $Oh = 0.05$ for a range of Eotvos numbers, $Eo = 28.8, 36, 72, 96, 196$. The analysis of the $Eo$ influence on the droplet deformation is carried out for small values of the Ohnesorge number, which is to say that surface tension is dominant over viscous stress. At low $Oh$, the $Eo$ number is the only dimensionless parameter influencing the break-up regime.
The grid size is $250 \times 1250$ for all the $Eo$ numbers considered. The symbol $t^* = \frac{t}{T}$ in Table 5.1, denotes the time span of the simulations.

Table 5.1: $Eo$ to dimensionless time span.

| $Eo$ | 28.8 | 36.0 | 72.0 | 96.0 | 196.0 |
|---|---|---|---|---|---|
| $t^*$ | 14.85 | 13.83 | 7.83 | 6.78 | 5.54 |

As shown in figure 5.12, the variation of $Eo$ has a strong effect on the drop behaviour. At low $Eo$ (fig. 5.12(a)), we observe an oscillating behaviour of the drop, which takes an ellipsoidal disc shape, subject to fluctuations due to the interactions between viscous stresses and surface tension. In this case, the external force is not able to break the intermolecular links, which results in a droplet oscillating behaviour without rupture.

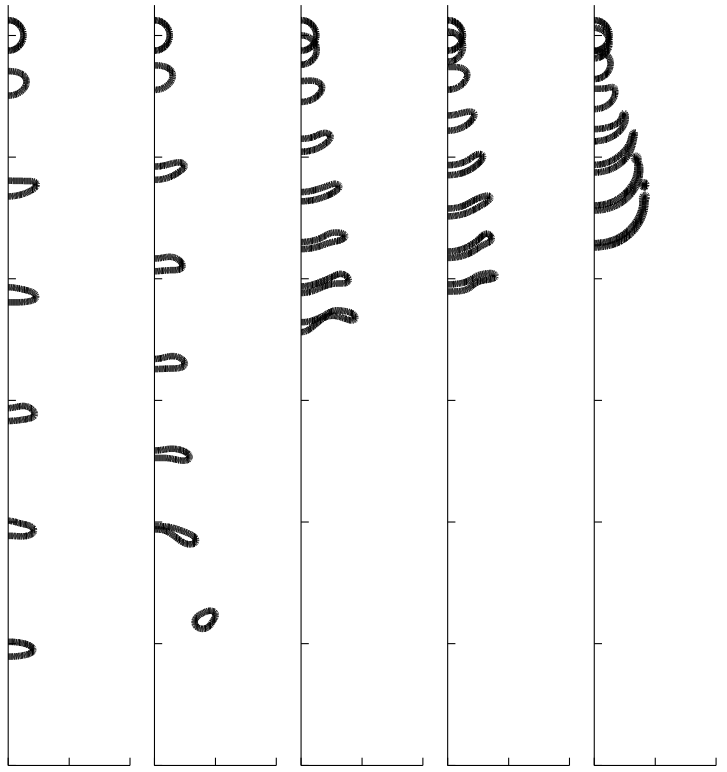

(a) $Eo = 28.8$ (b) $Eo = 36.0$ (c) $Eo = 72.0$ (d) $Eo = 96.0$ (e) $Eo = 196.0$

Figure 5.12: Density contours showing the shape of the droplet interface for a sequence of instants spaced $t^*/8$ in time, at different Eotovos numbers. The parameters of the simulation (lattice units) are $D = 50$, $R = 10$, $\rho_d = 2$, $\sigma = 0.001$.

At $Eo = 36$ (fig. 5.12(b)), the droplet enters the so-called backward-facing bag regime. As shown in Fig. 5.12(b), under the effect of the gravitational field, the droplet first takes the shape of an ellipsoidal

disc with upward concavity. Subsequently, gravity turns the droplet concavity downwards, until rupture occurs. In the first phases of motion, the hydrodynamic pressure in the rear-zone of the drop is higher than in the front. This is the reason why the liquid drop tends to take a disc-shaped configuration. In the evolution of phenomenon, the pressure gap tends to change direction and the droplet changes its curvature accordingly, until separation in two smaller droplets occurs.

Subsequently, a transition region is observed, until the shear stripping regime is reached at $Eo = 72$ (figs. 5.12(c) and 5.12(d)). As it can be observed, after an initial disk-like phase, the stabilizing effect of surface tension is no longer capable of balancing the gravitational force. As a result, the drop undergoes a major deformation and tends to assume a thin layer configuration. As $Eo$ increases from 72 to 96, the layer-droplet becomes increasingly thinner, until shear-stripping is observed. The separation of small liquid portions from the droplet occurs only in the case of $Eo = 196.0$. Also in this case, the formation of a thin layer is apparent, but, due to the high influence of gravitational force, the main structure is broken in two different parts. This shift of results is basically due to the fact that the two-dimensional model implemented here is not able to reproduce the full three-dimensional dynamics of droplet break-up.
A comparison with literature data (front tracking method [3]) is presented in figure 5.13. As can be observed, LB is constantly underpredictive in terms of drop penetration. This is most likely due to the fact that the front tracking method deals with an axis-symmetric configuration, while the LB simulation is purely 2D. Nevertheless, in view of the above limitations, the agreement between the two methods appears reasonable. Once again, the dimensionless position of the

droplet centermass is evaluated as the ratio between the traveled distance and the droplet diameter, and the dimensionless time is obtained by dividing the timestep by the characteristic time.

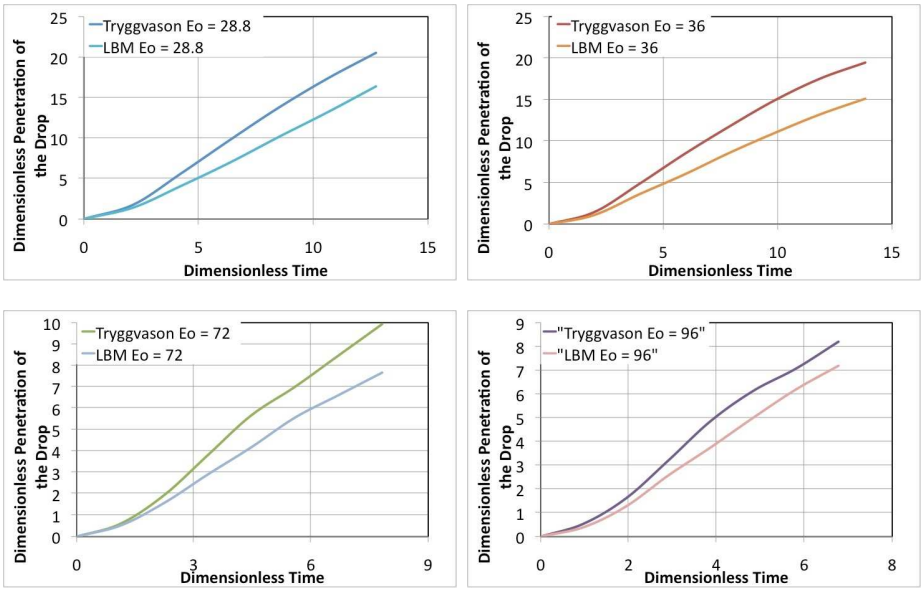


Figure 5.13: Centermass position of the droplet as a function of time. Comparison between the present LB and reference front-tracking method $Eo = 28.8, 36, 72, 96$.

## 5.3 The Coalescence

As a third example, we examine the collision and coalescence of 2D droplets (cylinders in 3D). A graphical scheme of coalescence problem is reported in the following figure 5.14.

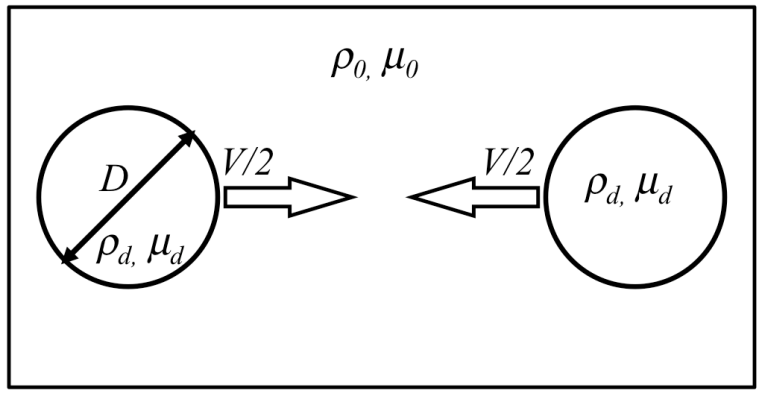


Figure 5.14: Scheme of coalescence of two-deimensional impacting droplets aligned in the same axis.

Both numerical and experimental data show that, upon colliding, 3D spherical droplets undergo different types of merging and coalescence, depending on the value of the Weber number and impact parameter [50, 51, 52, 53, 54, 55].
In particular, coaxial (perfectly head-on) droplets coalescence at $5 < We < 20$ gives rise to a single final droplet. On the other hand, at $We > 20$, the two droplets undergo a so-called reflexive breakup [50, 55], meaning by this that the coalesced droplet undergoes progressive deformations towards an elliptic and dumbell shapes, and finally, under the effect of internal vorticity motion, it breaks up again into two droplets moving along directions opposite to the initial ones (perfect reflection).

We have explored to which extent such complex sequence of events can be reproduced within a 2D model. Our simulations show no evidence of reflexive break-up up to $We \sim 100$. The droplets coalesce,

deform into a vertical dumbell, but, instead of further deforming into an horizontal dumbell and subsequently break-up, the dumbell shape is simply reabsorbed into a single droplet. This is most likely an effect of the major difference between the cylindrical versus spherical geometry in the energy budget controlling the sequence of events which lead to reflexive breakup. Unlike the case of direct breakup (without coalescence), such difference seems to play a major role. We have also investigated whether brakeup would be facilitated by increasing the Reynolds number [54]. Simulations at $Re = 150, 200, 250$ show only minor effects on the droplet shape, with no impact on the final outcome of the droplet collision.

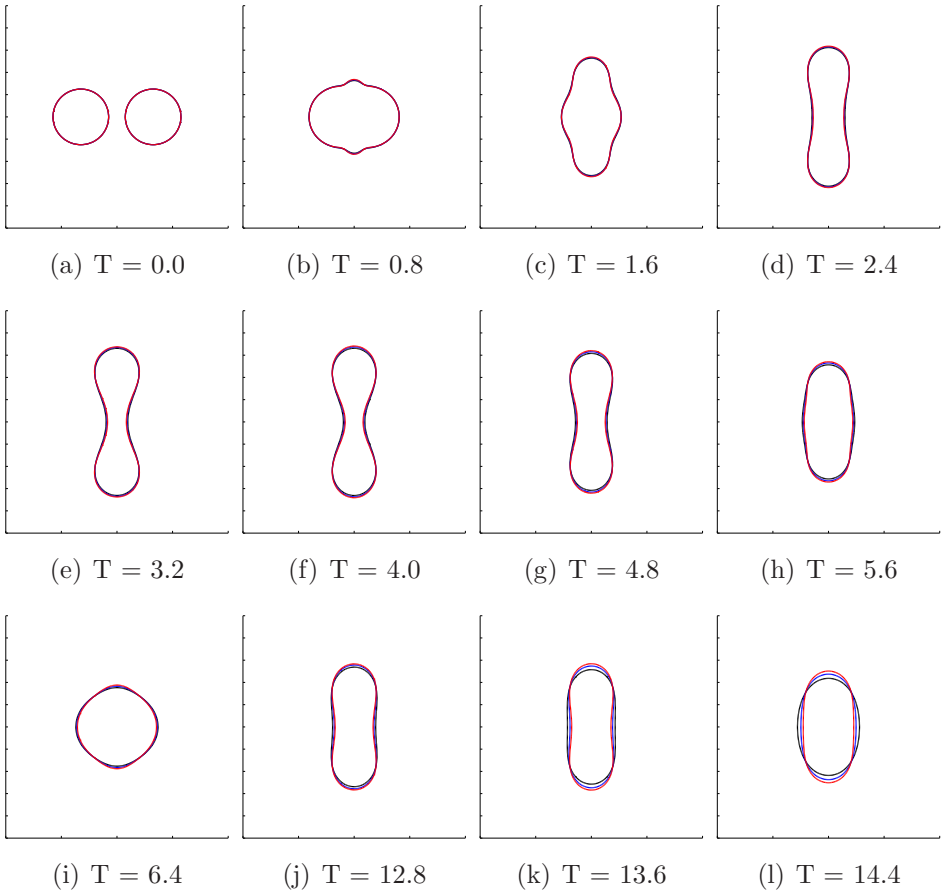

(a) T = 0.0 (b) T = 0.8 (c) T = 1.6 (d) T = 2.4

(e) T = 3.2 (f) T = 4.0 (g) T = 4.8 (h) T = 5.6

(i) T = 6.4 (j) T = 12.8 (k) T = 13.6 (l) T = 14.4

Figure 5.15: Density contour plots at different dimensionless times. Behaviour of two impacting droplets at $We = 50$ and $Re = 150, 200, 250$. Black $Re = 150$, Blue $Re = 200$, Red $Re = 250$.

For a higher $We$ number equal to 150, the rupture of coalescing dropets has been reached as reported in the following picture, 5.16.

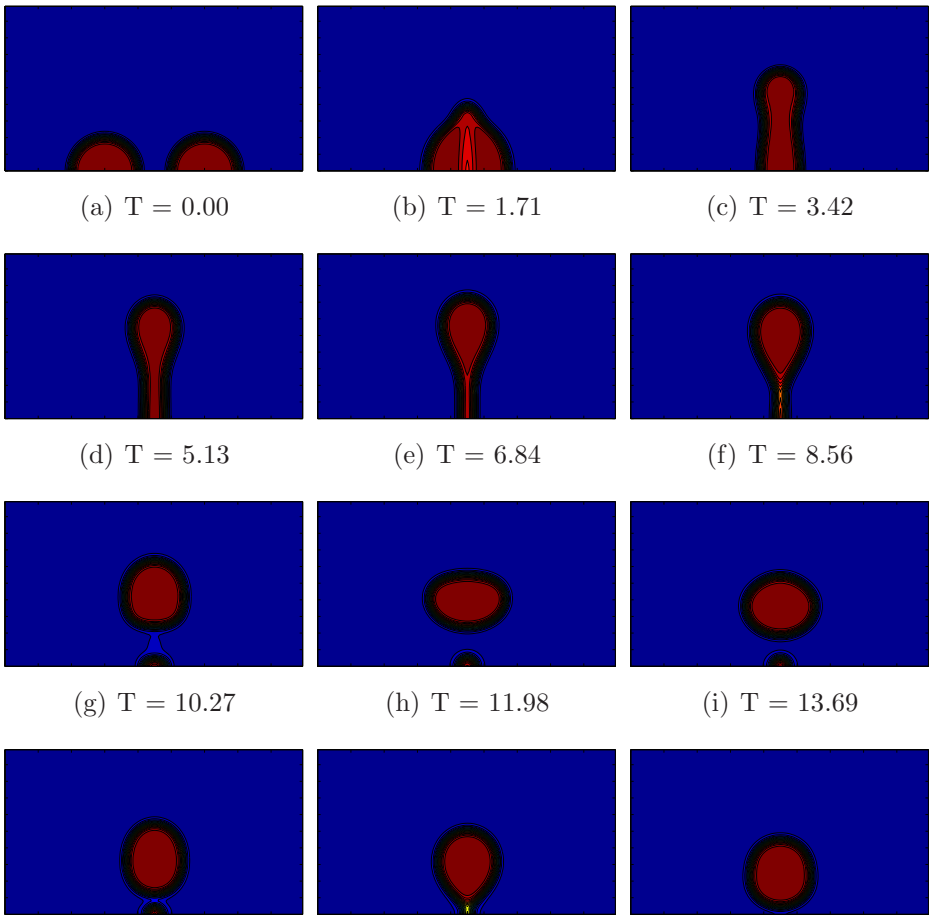

(a) T = 0.00 (b) T = 1.71 (c) T = 3.42

(d) T = 5.13 (e) T = 6.84 (f) T = 8.56

(g) T = 10.27 (h) T = 11.98 (i) T = 13.69

(j) T = 15.40 (k) T = 17.11 (l) T = 18.83

Figure 5.16: Density contour plots at different dimensionless times. Behaviour of two impacting droplets at $We = 150$ when the 2D code starts to highlight break-up.

As can be noticed from Figure 5.16, the rupture realiazed in this

application is far from the expected one for this kind of problems, [50]. In fact, the Weber regime should be characterized from a reflexive break-up with the formation of two bubbles wich moves following opposite directions on the same axis of the incoming velocity. On the contrary, a kind of break-up is noticed but the reflected droplets move along the normal direction.

## 5.4 The Parallel Code - Results for Secondary Break Up

In the following paragraph some results obtained with the parallel code implemented will be proposed. The structure of the new thre-dimensional code is comparable with the two dimensional one described above. The main differences are represented from the *message passing interface* and to the three-dimensional formulation of the code. In this first test case, we analyze the behaviour of a liquid droplet sujected to a gravitational field. As pointed out in the same chapter, where the bi-dimensional behaviour of a falling droplet has been analyzed, one of the characteristic parameters is the $Eo$ number. More specifically, in the following figure 5.17 the results obtained for $Eo = 96.0$ are reported and density ratio equal to 10.0 are reported. As done fore the two-dimensional simulation presented above the Ohnesorge number has been kept constant to 0.05 and imposed to be same for both the phases.

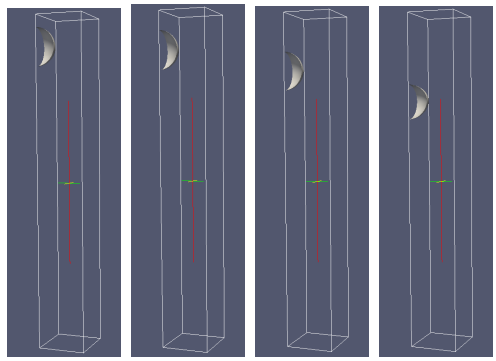

(a) T = 0.00 (b) T = 0.65 (c) T = 1.29 (d) T = 1.94

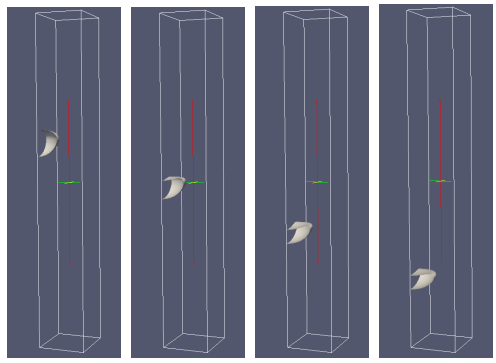

(e) T = 2.58 (f) T = 3.23 (g) T = 3.87 (h) T = 4.52

Figure 5.17: Density contours showing the shape of the 3D droplet interface for a sequence of instants. The parameters of the simulation (lattice units) are $Eo = 96.0$, $D = 50$, $R = 20$, $\rho_d = 1$, $\sigma = 0.001$. The rapresentation is limited to nodes solved only in one processor in order to more clearly show the interface evolution in time.

As can be observed in the previous sequence the 3-dimensional code

seems not to be able to highlight rupture as expected from the theory [3]. In order to better compare the results and better understand the capabilities of the method a droplet penetration comparision will be carried out again. In figure 5.18 the results obtained for this quantity are reported.

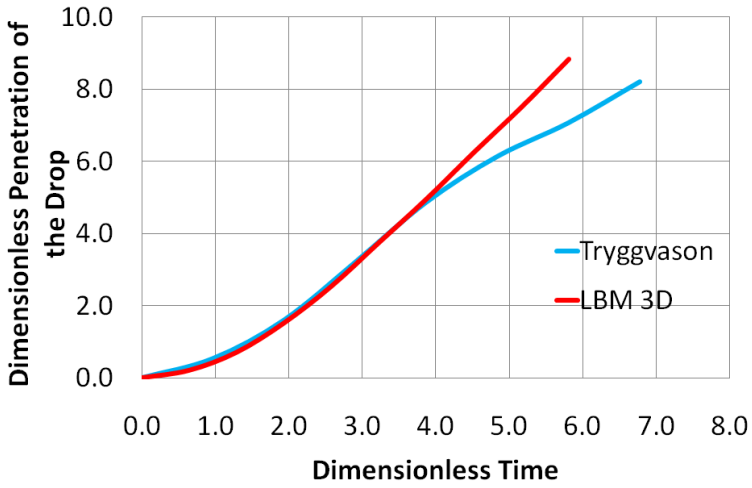


Figure 5.18: Dimensionless droplet penetration for reference [3] and implemented 3D parallel code.

As can be observed there is a good agreement between two approaches until the breakup takes place. After the beginning of it there is a missmatch between solution obtained from reference [3] and three-dimensional LBM. As can be noticed, the breakup significantly affect the trajectory of droplet.

# Chapter 6

# Conclusion

There are a lot of factors which are source of complexity in the multiphase flow phenomena; not only the interaction between bubbles-droplets-particles immersed in the fluid, but also physical problems, like the transition between different liuid-gas flow regimes, or the presence of a perturbed interface, as well the simultaneous presence of phenomena occuring at different scales. This complexity represents a tough limit in the use of fully analitical methods designed in order to solve this kind of problems. For example, also the flow around spheres -which have intrinsically simple shapes- present some analytical sultion which are definetely limited to either to small or large Reynolds numbers. For the most interesting applications, referred to a moderate Reynolds number, there is not a closed analytical solution.

The aim of this work has been the analysis of a multiphase algorithm for Lattice Boltzmann Method. In a large number of applications, in fact, the understaing of interactions between different phases become crucial. Over last decades a series of model have been developed with

the goal to determine the correct modeling of this kind of interaction. By the way, the traditional approaches based on Navier-Stokes techniques have always required a huge degree of approximation and a high computing time, due to the high order of interactions modeled. During last years a series of models based on the kinematic discretization of Boltzmann equation have gained a primary role in multiphase simulation.

The main idea of LBM starts from a more detailed approach in solving continuity equations which characterize every fluid-dynamical problem. Thus, starting from this smaller scale approach, the definition of multiphase models have benn deeply analyzed. In the numerical panorama, there are a lot of possibilities for modeling multiphase interaction with LBM, between them we have chosen a really promising model, developed by Lee et al., which sholud allow to tame a numerical unwated effect known as spurious currents, present with other approaches, and, at the same time, it should allow to reach a high density ratio between two phases. These two main advantages have maked the studied approach very appealing.

Then, the aim of this work has been the characterization and the analysis of this model in order to uderstand its possible usage in an engineering environment. More specifically the possibility to study primary and secondary break up has been deeply analyzed with the results presented in previous chapters. Moreover a 3D fully parallel version of the model has been developed in order to make possible the solution of a large number of applications which involve three-dimensional effects which can be captured only with a fully determined scheme. The two-dimensional analysis, in fact, pays its simplicity and

velocity in reaching the solution with a lack of precision due to the complexity of involved phenomena.

In conclusion, the results show a good agreement of the model with the reference data for a primary breakup, analyzed through Rayleigh-Taylor Instability, while it becomes less accurate studying a secondary breakup compared with some results obtained with a front tracking apporach. This lack of precison can be attributed to the three-dimensional effects which are not captured in the two-dimensional analysis here presented. This can be easily unterstood because a two-dimensional droplet represents a three-dimensional cylinder which has rupture dynamics very far from a three dimensional droplet. Finally some results in terms of coalescence have been showed. They are affected from the same kind of problem as well. The last results presented have shown the possibility of the implemented model to simulate a fully three-dimensional test-case with a paralellized version of the model.

Thus, the model have shown very promising results, especially in terms of accuracy and quality of analysis, but of course it has affected by a series of inconvenients which characterize the laticce boltzmann method and the multiphase modeling with this kind of approach. Of course other improvememnts have to be done in order to better characterize and developed the multiphase model here presented. All this activities have to be done in order to develop a valuable tool for the simulation of multiphase problems in a large numeber of engineering applications.

# Bibliography


[1] Ferziger, J. H., and Peric, M., 2002. *Computational methods for fluid dynamics*. Springer.

[2] He, X., Chen, S., and Zhang, R., 1999. "A lattice boltzmann scheme for incompressible multiphase flow and its application in simulation of rayleigh-taylor instability". *Journal of Computational Physics,* **152**, pp. 642–663.

[3] Han, J., and Tryggvason, G. "Secondary breakup of liquid drops in axisymmetric geometry - part i, constant acceleration". *Physics of Fluids,* **11**, pp. 3650–3667.

[4] Prosperetti, A., and Tryggvason, G., 2005. *Computational methods for multiphase flow*. Cambridge University Press.

[5] Ishii, M., and Hibiki, T., 2007. *Thermo-Fluid Dynamics of Two-Phase flow*. Springer.

[6] Postrioti, L., and Ubertini, S., 2006. "An integraded experimental-numerical study of hsdi diesel injection system and spray dynamics". *SAE 2006-01-1389*.

[7] Grunau, D., Chen, S., and Eggert, K., 1993. "A lattice boltzmann model for multiphase fluid flows". *Physics of Fluids A,* **5**(2557).

[8] Chung, T. J., 2002. *Computational fluid dynamics.* Cambridge University Press.

[9] Durst, F., 2008. *Fluid Mechanics - An Introduction to the theory of flows.* Springer.

[10] Kolev, N. I., 2007. *Multiphase Flow Dynamics - 1 Fundamentals.* Springer.

[11] Capuani, F., Pagonabarraga, I., and Frenkel, D. "Discrete solution of the electrokinetic equations". *Journal of Chemical Physics,* **221**, pp. 973–986.

[12] Scotti, A., Meneveau, C., and K., L. "Generalized Smagorinsky model for anisotropic grids". *Physics of Fluids A,* **5**, pp. 2306–2308.

[13] Tennekes, H., and Lumley, J., 1972. *A first course in turbulence.* MIT Press, Cambridge.

[14] Krause, E., 2005. *Fluid Mechanics - With problems and solutions, and an aerodynamic laboratory.* Springer.

[15] Sethian, J., 1999. *Level set methods and fast marching methods: evolving interfaces in computational geometry, fluid mechanics, computer vision, and material science.* Cambridge University Press.

[16] Succi, S., 2001. *The Lattice Boltzmann equation - for fluid dynamics and beyond.* Oxford University Press.

[17] Gross, E., Bhatnagar, P., and Krook, M., 1954. "A model for collisional processes in gases 1: Small amplitude processes in charged and neutral one-component system". *Physiscal Review Letters,* **54**.

[18] D'Humières, D., 2002. "Multiple-relaxation-time lattice boltzmann models in three dimensions". *Phil. Trans. R. Soc. Lond. A,* **360**, p. 437–451.

[19] Boghosian, M., Yepez, J., Coveney, P. V., and Wager, A., 2001. "Entropic lattice boltzmann methods". *Proc. R. Soc. Lond. A,* **457**, p. 717–766.

[20] D'Humières, D., Quian, Y., and Lallemand, P. "Lattice bgk models for naveri-stokes equation". *Europhysics Letters,* **17**, pp. 479–484.

[21] Eggers, J., 1997. "Nonlinear dynamics and breakup of free-surface flows". *Rev. Mod. Phys.,* **69**, pp. 865–927.

[22] Gunstensen, A. K., Rothman, D. H., Zaleski, S., and Zanetti, G., 1991. "Lattice boltzmann model of immiscible fluids". *Physical Review A,* **43**, pp. 4320–4327.

[23] Gunstensen, A. K., and Rothman, D. H., 1992. "Microscopic modeling of immiscible fluids in three dimensions by a lattice boltzmann method". *Europhysics Letters,* **18**, pp. 157–161.

[24] Rothman, D. H., and Keller, J. M., 1988. "Immiscible cellular-automaton fluids". *Journal of Statistical Physics,* **52**, pp. 1119–1127.

[25] Chen, H., 1993. "Discrete boltzmann systems and fluid flows". *Computer in Physics,* **7**(6).

[26] Luo, L. S., and Girimaji, S. S., 2003. "Theory of the lattice boltzmann method: Two-fluid model for binary mixtures". *Physical Review E,* **67**(036302).

[27] Lee, T., and Lin, C.-L., 2005. "A stable discretization of the lattice boltzmann equation for simulation of incompressible two-phase flows at high density ratio". *Journal of Computational Physics,* **206**, pp. 16–47.

[28] Lee, T., and Fischer, P., 2006. "Eliminating parasitic currents in the lattice boltzmann equation method for nonideal gasses". *Physical Review E,* **74**(046709).

[29] He, X., Shan, X., and Doolen, G. D., 1998. "A discrete boltzmann equation model for non-ideal gases". *Physical Review E,* **57**(R13).

[30] Lee, T., 2009. "Effects of incompressibility on the elimination of parasitic currents in the lattice boltzmann equation method for binary fluids". *Computers and Mathematics with Applications (2009), doi:10.1016/j.camwa.2009.02.017.*

[31] Lee, T., and Liu, L., 2008. "Wall boundary condition in the lattice boltzmann equation method for nonideal gasses". *Physical Review E,* **78**(017702).

[32] Sbragaglia, M., Benzi, R., Biferale, L., Succi, S., Sugiyama, K., and Toschi, F., 2007. "Generalized lattice boltzmann method with multirange pseudopotential". *Physical Review E,* **75**(026702).

[33] Falcucci, G., Bella, G., Chiatti, G., Chibbaro, S., Sbragaglia, M., and Succi, S., 2007. "Lattice bolzmann models with mid-range interactions". *Communication in Computational Physics,* **2**, pp. 1071–1084.

[34] Falcucci, G., Chiatti, G., Succi, S., Kuzmin, A., and Mohamad, A., 2009. "Rupture of a ferrofluid droplet in external magnetic fields using a single-component lattice boltzmann model for non-ideal fluids". *Physical Review E,* **79**(056706).

[35] He, X., and Doolen, G., 2002. "Thermodynamic foundations of kinetic theory and lattice boltzmann models for multiphase flows". *Journal of Statistical Physics,* **107**, pp. 309–328.

[36] Falcucci, G., Succi, S., and Ubertini, S. "Lattice boltzmann multiphase model with lennard-jones potential". *submitted to Physical Review E.*

[37] Chiappini, D., Bella, G., Succi, S., Toschi, F., and Ubertini, S., 2009. "Improved lattice boltzmann without parasitic currents for rayleigh-taylor instability". *Communication in Computational Physics,* **7**, pp. 423–444.

[38] Korner, C., Thies, M., Hofmann, T., Thurey, N., and Rude, U., 2005. "Lattice boltzmann model for free surface flow for modeling foaming". *Journal of Statistical Physics,* **121**.

[39] Thurey, N., Rude, U., and Korner, C. "Interactive free surface fluids with the lattice botlzmann method". *Technical Report 05-4, Lehrstuhl fur Informatik 10 (Systemsimulation), University of Erlangen-Nueremberg.*

[40] Chen, S., and Doolen, G., 1998. "Lattice boltzmann method for fluid flows". *Annual Review of Fluid Mechanics.*

[41] Chiappini, D., Bella, G., Succi, S., and Ubertini, S., 2009. "Application of finite-difference lattice boltzmann method to break-up and coalescence in multiphase flows". *International Journal of Modern Physics C,* **141**.

[42] Sharp, D. H., 1984. "An overview of rayleigh-taylor instability". *Physica D,* **12**(3).

[43] Nourgaliev, R. R., Dinh, T. N., and Theofanous, T. G., 2004. "A pseudocompressibility method for the numerical simulation of incompressible multifluid flows". *International Journal of Multiphase Flow,* **30**, pp. 901–937.

[44] Cabot, W. H., and Cook, A. W., 2006. "Reynolds number effects on rayleigh-taylor instability with possible implications for type-ia supernovae". *Nature Physics,* **2**.

[45] Cabot, B., Cook, A., and Miller, P., July 2006. "Direct numerical simulation of rayleigh-taylor instability". *IWPCTM10, Paris.*

[46] Wilkinson, J. P., and Jacobs, J. W. "Experimental study of the single-mode three-dimensional rayleigh-taylor instability". *Physics of Fluids,* **19**(124102).

[47] Chertkov, M., Kolokolov, I., and Lebedev, V. "Effects of surface tension on immiscible rayleigh-taylor turbulence". *Physical Review E,* **71**(055301).

[48] Huang, Z., De Luca, A., Atherton, T. J., Bird, M., and Rosenblatt, C. "Rayleigh-taylor instability experiments with precise and arbitrary control of the initial interface shape". *Phisical Review Letters,* **99**(204502).

[49] Nomura, K., Koshizuka, S., Oka, Y., and Obata, H. "Numerical simulation for meniscus bridge formation and breakage". *Journal of Nuclear Science and Technology,* **38**, pp. 1057–1064.

[50] Ashgriz, N., and Poo, J. "Coalescence and separation in binary collisions of liquid drops". *Journal of Fluid Mechanics,* **221**, pp. 183–204.

[51] Stone, H. A. "Dynamics of drop deformation and breakup in viscous fluids". *Annual Review of Fluid Mechanics,* **26**, pp. 65–102.

[52] Sun, Z., Xi, G., and Chen, X. "Numerical simulation of binary collisions using a modified surface tension model with particle method". *Nuclear Engineering and Design,* **239**, pp. 619–627.

[53] Gupta, A., and Kumar, R. "Lattice boltzmann simulation to study multiple bubble dynamics". *International Journal of Heat and Mass Transfer,* **51**, pp. 5192–5203.

[54] Mashayek, F., Ashgriz, N., Minkowycz, W. J., and Shotorban, B. "Coalescence collision of liquid drops". *International Journal of Heat and Mass Transfer,* **46**, pp. 77–89.

[55] Sakakibara, B., and Inamuro, T. "Lattice boltzmann simulation of collision dynamics of two unequal-size droplets". *International Journal of Heat and Mass Transfer,* **51**, pp. 3207–3216.

# Acknowledgements

At the end of this work there are many people who I should thank and for sure I will forget some of them, hoping that they will forgive me.
First of all, I would like to thank prof. Gino Bella who I worked with during last years. He thaught me a lot of things at different levels. He showed everyday his willingness in helping me not only when I had to face up with engineering problems, but he also with *normal* life issues. Moreover he always paid attention to my education and he was interested in allowing my personal growth up on the career ladder. He gave me the opportunity to travel around the world in order to reach a high level of knowledge in my research topic. Nevertheless being involved in academic research he always highlighted the importance of addressing every research to the industrial appllication wih significant advantages for my person.

Secondly I would like to thank prof. Stefano Ubertini who introduced me to the fascinating world of Lattice Boltzmann Method and he helped me in many situations. He showed everyday his vast knowledge being always willing to share it and he did it always addressing his efforts to the personal growth of each one of his co-workers.

I would like to write a special thank to Dr. Sauro Succi as well. He always showed his interest in *people* rather than in *workers*. Day by day he taught me the correct way of understanding the Lattice Boltzmann Method and he tried to make me indipendent in solving this kind of problems. He helped me in every pubblication I wrote with very valuable and significative contribution.

I would like to thank prof. Fabio Gori too. He was willing to be my supervisor and he gave me the opportunity to know international schools, encouraging me in this kind of activity.

Finally there are many people who contributed in such a way to my personal growth. Between them for sure, prof. Taehun Lee from City College of New York, who gave me the possibility to study in his departement for three months. He helped me whenever I had dubt about the model, especially at the beginning of the work. I would like to thank Dr. Federico Toschi too, who I worked with until he had been in Rome and who helped me in better understanding the LBM. Moreover I would like to thank Eng. Alessandro de Maio and Dr. Silvia Palpacelli who helped me in a very valuable way during the parallelization procedure of the code.

A special thanks to all my colligues and to all my room-mates. Spending days with them made working more pleasant and funny. They contribute in different manners to my personal growth. Also in difficult periods, we spent together very good time in our office in the departement. I will not name any of them because the list will be very long but I really would like to thank them for every bit of time

we spent together.

Finally, a particular thank to my family, especially to my parents. They deeply know me and they were very patient during these difficult years. I passed through many obstacles and difficulties and I am sure that I had been able to overcome those only because they supported me in everything I did. They gave me the opportunity to spend these years at the University and they encouraged me in doing it with the feeling that they were looking after me.